ABSTRACT

Title of Dissertation: ION PLUME DAMAGE IN FORMATION FLIGHT REGIMES

Jarred Alexander Young, Doctor of Philosophy, 2017

Dissertation directed by: Associate Professor Raymond J. Sedwick
Department of Aerospace Engineering

This effort examines the potential for damage from plume impingement from an electric propulsion system within spacecraft missions that utilize a formation flight architecture. Specifically, the potential erosion of a structural material (Aluminum) and anti-reflective coatings for solar cell coverglass are explored. Sputter yields for the materials of Aluminum, Magnesium Fluoride, and Indium Tin Oxide are experimentally

validated using an electrostatic ion source at energies varying from 500-1500 eV. Erosion depths are analyzed using white-light optical profilometry to measure potential depths up to 1 μm. This erosion data was then utilized to create (or augment) Bohdansky and Yamamura theoretical curve fits for multiple incidence angles to look at theoretical sputter effects within formation flight regimes at multiple formation distances from 50-1000 m. The damage from these electric propulsion plumes is explored throughout multiple orbital conditions from LEO, Sun-Synchronous, and GEO. Factors affecting erosion are: plume density, local geomagnetic field environment and incidence angles of target surfaces. Results from this simulated study show significant erosion with GEO with minor erosion in some LEO and all Sun-Synchronous cases.

ION PLUME DAMAGE IN FORMATION FLIGHT REGIMES

By

Jarred Alexander Young

Dissertation submitted to the Faculty of the Graduate School of the
University of Maryland, College Park in partial fulfillment
of the requirements for the degree of
Doctor of Philosophy
2017

Advisory Committee:

Professor Raymond J. Sedwick, Chair
Professor David L. Akin
Professor Kenneth Yu
Professor Christopher Cadou
Professor Rami Kishek
Professor Gottlieb Oehrlein

Dedication

This dissertation is dedicated to the memory and the testament of my grandfather, William Benjamin Young, who was lost on July 17, 2016 to Alzheimer's Dementia.

Acknowledgements

A wise man once said, “It’s been a long road…..getting from there to here….” I really think they must have been talking about my doctoral journey. Along the way, I’ve done things I’ve never thought possible and I’ve met people that have given energy to me on this long road to this moment.

First, I’d like to give thanks to my lab-mates at the Space Power and Propulsion Laboratory. For the better part of a decade, we’ve struggled through lab moves, earthquakes, electrical mishaps, and other numerous things together. Although each and every one of you have made the journey that much sweeter in your own way, I’d especially like to thank Adriane Faust and Arber Masati.

Adriane, affectionately known as “Girl on the Bike” to my family, I cannot count how many times you’ve made me laugh whenever I was toiling away in the lab or at work. Whether it was you channeling your inner Buffalo Bill from “Silence of the Lambs” or using RuPaul’s “Glamazon” on as your theme song, you have always brightened my day.

Arber, what can I say about you that hasn’t already been said? You’re a good friend…..even though that one time you did put a cockroach on my desk in a transparent plastic cup so I’d freak out when I’d go to my desk. But, I forgive you, because you’re an awesome dude. We’ve worked together, laughed together, and partied together. Now, if we could only get Young-Masati Aerospace off of the ground……

I’d also like to take this time to thank all of my undergraduate research assistants from throughout the years: Ethan Evans (currently completing his doctorate at Georgia Tech), Hari Deveraj (working on his Mechanical Engineering degree here at UMD), Janessa Wilkins, Andy

Budimirovich, Andrew Dallas, Elya Pardes, Skylar Trythall, Chris Lawler, Alex Günter, Spencer Levin (who's beginning his own graduate journey), and Thomas Pitzel (starting his Aerospace Master's at UMD). There are many things I could say about each and every one of you. Nevertheless, I wish you all very well and know that your efforts helped me get to where I am today. I'm very appreciative for all your help!

My lab-mates are all great people (even you, Pratik!) but if it weren't for my friends outside of the lab, I may have went insane. A lot of my friends have pushed me and supported me on this journey, but I owe a special thanks to you guys, my "Team Black Aerospace". Brad, Romina, and David, if it weren't for you three, I'm not sure I would have made it across the finish line.

Brad, I've known you since my last year of undergrad here at UMD. Since then, you've been a mentor, friend, and practically a brother to me. Hell, who else can I frequently share Archer quotes with? (Apparently, no one else…..because that's how you get ants.) With our constant debates on philosophy, life, and late-night research discussions, I'm not sure I'd be as aware of the world as I am today. I'm truly honored to be called your friend.

Romina, if it weren't for your awesome panda-like hugs and positive energy, I would've been too drained to get to this point. Even though we've had our ups and downs, I knew that you were always there for me. Even when my left arm was a punching bag that couldn't be tenderized enough by your "friendship", somehow we've managed to get to this point. Hugs!

David, every time we get together, I can't help but be motivated to get things done. When times were tough and I ran into you, you always told me things like, "Let's get it!" or

"Don't get married!" Now, I'm not saying all the advice was amazing but you always have the most positive can-do attitude of anyone I've ever known.

Although I've received support from many sources, from my lab-mates to my friends, I'd like to take the time recognize a few faculty that this journey would not be possible without. Firstly, I'd like to extend my gratitude to Dr. William Fourney, who was the first professor I met from this great university. I remember being a fresh incoming freshman, bursting into his office and demanding to know why I wasn't admitted into the Aerospace program. Of course, instead of kicking me out, he took the time to figure out my problem. When it came down to the department not taking ACT scores, he had told me that I'd have to start the hard way by taking all of the gateway courses to get through the limited enrollment process. Throughout the process, he was advising me and even allowing me access to the first-year Aerospace classes so I wouldn't be too far behind. He kept pushing me to keep moving and he constantly reminded me that what I was doing was a very tough thing that only "10-20% of students that go this route" succeed in. I was usually mocked by my close friends from time to time that I may have been his "illegitimate son" for the way I always talked about how I got to this point. He helped me make sure that my dream would be achieved. Needless to say, if it weren't for him, I wouldn't be writing this dissertation today. I can never thank him enough.

Secondly, I'd like to give a huge thank you to my "Engineering Mom", Dr. Mary Bowden. Dr. Bowden taught my first engineering class that I had taken after I was admitted to the aerospace program, Statics. Even though it's a very fundamental class that's a huge foundation of engineering, I struggled mightily. I remember failing the first test and then coming to her for counsel and she kept pushing me to get through the class, constantly telling me, "Don't stress!!!" (Which, by the way, I swear is her motto….) I owe a lot of my success in that class to

her and from that point on, she has been willing to help advise me through a lot of the little things from stuggling through grad school to dealing with rough patches with my family. I'm pleased to call a trusted advisor and a great friend.

Finally, I'd like to take this opportunity to thank my advisor, Dr. Raymond Sedwick. I remember when I was thinking about starting along a research path as an undergrad, I came to him and asked if I could work in his lab. He told me to come back in two weeks when my schedule fleshed out. Of course, being in Controls as a junior, that didn't exactly pan out. So, when I came back to him the next semester, I had told him that I wanted in. "Come back in two weeks," he said. So, I came back in two days and said, "If I don't do this now, I might not make it back." And that's how I ended up in the SPPL. From then, whether it was naming timing chips that kept blowing up in my faulty circuit to struggling through some relation that I was having trouble with, he was always there for me. Even though his boundless knowledge never ceases to amaze me, what kept me going was his intense passion for his work. Between that, and his endless supply of patience, through all of my research ups and downs, it's truly been a joy to work with him and I'm truly appreciative for having his tutelage and guidance to get to this point.

Everyone mentioned above (and those that haven't) gave me a lot of support through this ordeal, even when I was personally struggling. They say every grad school journey is unique and I certainly can't refute that. While trying to deal with my research problems and the like, both of my parents became intensely ill around the same time and for almost two years, I struggled to get them the care they needed and still tried to get my work done. Needless to say, even when I thought I would've been kicked out for not producing enough, everyone (especially my advisor)

kept pushing me to do what I needed to do and I can't thank them enough for that. Words do not do it justice.

Which bring me to the last group of people I want to thank: my family. Mom, even though there are times where I'm not even sure we're related, I have nothing but love for you. I wouldn't have chosen space propulsion if it weren't for you getting me into Star Trek. You never believed me when I said "I'm going to be a propulsion engineer!" Well Mom, look at me now! You would always keep calling me, asking me, "Is this month it? Are you gonna make it?" and pushing me to get the job done and always being in my corner. You pushed me on this journey and now we're here. I love you, Mom.

Finally, if it weren't for my grand-father, I wouldn't have gotten to this point either. Dad, I know you're watching over me, but if you didn't instill in me a never-quit mentality and a hardy work ethic, I wouldn't be writing this today. Dad (my grandfather) was my hero as he worked for NASA Goddard and built parts of those satellites overhead today and loved to tell me about "space age'n", as he'd always say. When I told him I was going to be an engineer, he told me to be "Number one, because you're my Number One". My only regret was that you couldn't be here to share in this moment with me. I love you, Dad!

Thanks for going through all of these acknowledgements and I hope you find this dissertation as enlightening as it was for me to work on it. Live Long and Prosper!

Table of Contents

List of Figures

List of Tables

1. Introduction

One of the greatest achievements of the Space Race was when Neil Armstrong was the first human to set foot on the Moon and proclaimed, “One small step for man, one giant leap for mankind.” And, as the exploration of space became a realization, so would the need for advanced equipment for exploration. Many satellites were launched to observe other planets in our solar system. The best example of space missions like this are Voyager 1 and 2. These missions required gravity assists to make their grand tour across the solar system, observing the Jovian planets, and ultimately heading for interstellar space. Yet, exploration missions like this were limited by one major factor: their inability to significantly alter trajectory without sacrificing operational range.

The main reason for these limitations in a vast majority of propulsion systems are usually derived from the types of propulsion systems used. Propulsion, as defined by Sutton and Biblarz, is the act of changing the motion of a body[1]. In space, this usually boils down to changing the momentum of the body that needs to be in motion. This is usually done by ejecting stored material known as *propellant* from the body. The act of this ejection generates *thrust*, which leads us to the definition of thrust as defined in Equation 1-1.

$$T = \dot{m}u_e \tag{1-1}$$

As seen from this equation, thrust depends on the mass throughput of the propellant as well as its exhaust velocity. The majority of satellites use systems such as *cold gas thrusters*, which eject a stored propellant gas under pressure, and *chemical rockets*, which

use both a pressurized propellant as well as *fuel* to provide the energy for the chemical reaction. The reason chemical rockets use fuel for their energetic reactions is to increase the overall exhaust velocity of the reaction. Exhaust velocity is an important factor to consider in spacecraft mission ranges to due to a concept known as *specific impulse*, as defined in Equation 1-2. Specific impulse is a basic metric used to directly analyze the propulsion system's efficiency at using its propellant. As shown from Equation 1-2, the exhaust velocity is directly proportional to the specific impulse. Furthermore, if we introduce the Rocket Equation as shown in Equation 1-3, this clearly shows that the exhaust velocity is also directly proportional to the Δv of a spacecraft, which is a measure of the spacecraft's ability to change its momentum. Chemical rocket systems have been shown to have a maximum specific impulse of 452.5 s, which belongs to the Space

$$I_{sp} = {}^{u_e}/_{g_0} \tag{1-2}$$

$$\Delta v = -u_e \ln {}^{m_f}/_{m_i} \tag{1-3}$$

Shuttle Main Engine1. While this provides a large thrust, this limits the overall range of the spacecraft and, therefore, its mission profiles.

In the modern era, where satellites are commonplace in the scientific and commercial arenas, mission designers and manufacturers are looking for ways to expand the capabilities of satellites while making them smaller, cheaper, and more advanced. This would also include extending the Δv of the spacecraft while trying to reduce the mass of the overall craft. To this end, a larger number of missions are beginning to use Electric Propulsion (now being abbreviated as EP) systems which, unlike chemical

systems that use a physical substance as the fuel for the reaction, use electrical power to drive the reaction. The result provides a larger mission lifetime through the order of magnitude increase of specific impulse.

At the beginning of the 21st century, more spacecraft missions began to look into formation flight concepts, where a number of smaller satellites would be placed in a set formation to perform a larger satellite's job[2]. As their mission profiles will become more complex, the need for EP systems are a priority.

1.1. Electric Propulsion

1.1.1. General Background

As defined by Jahn, electric propulsion is defined through "the acceleration of gases for propulsion by electrical heating and/or by electric and magnetic body forces[3]." As mentioned above, EP systems replace actual physical fuel with electrical power as the main energy source for the reaction. This can lead to a much larger exhaust velocity for the propellant than through standard chemical means. Electric thrusters can be separated into three categories: *Electrothermal, Electrostatic,* and *Electromagnetic*. Electrothermal systems rely on a heating element that is powered electrically in order to energize the propellant that is then expanded through a nozzle. Electrostatic systems use electric fields as their primary means of accelerating the propellant. Likewise, electromagnetic systems use EM fields to accelerate their propellant. For the purposes of this work, we will limit the discussion to electrostatic systems, as these systems have the most flight heritage (and have the most direct relation to the work contained herein).

As stated, electrostatic systems use electric fields in order to accelerate their propellant. To manipulate the propellant via electrostatic forces, it is necessary to ionize the propellant. As such, a vast majority of EP systems utilize some form of plasma discharge to ionize the propellant. The two main types of discharges that can be used are DC, which usually utilizes electron bombardment ionization, and RF discharges, which heat the propellant gas with EM waves to ionize the propellant to form the plasma. For either type of discharge, most systems use a noble gas propellant such as xenon (and, in some cases, argon). This is due to the fact that these gases are non-toxic, do not condense on the spacecraft if not kept cryogenically, and their relatively low ionization energies[4]. A sample diagram of a standard DC discharge ion source is pictured below.

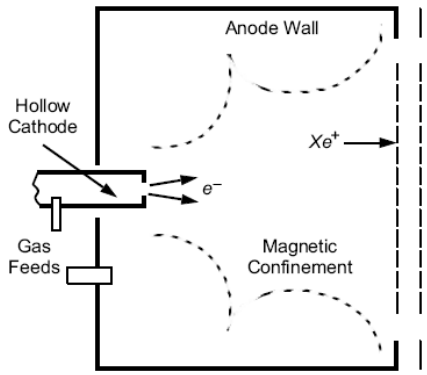

Fig. 1: Diagram of DC Discharge Chamber [4]

Electron bombardment ionization entails an electron stream from a cathode source that is then accelerated by the anode, but kept away from it by a magnetic field via Larmor motion. These energized electrons, or “primary electrons” then bombard the neutral propellant to ionize it, leaving a slightly less energetic electron (a “secondary”) in order to aid in the ongoing plasma reaction process. While this process enables

ionization, it is not self-sustaining and requires a constant stream of primary electrons to maintain the reaction. As the propellant gas is now ionized by the plasma reaction, the ions drift towards the plasma sheath. The sheath is the potential boundary between the plasma and the surface that the plasma is contained by (in this case, the discharge chamber). As ions drift through the plasma sheath, they experience a small acceleration force proportional to the electron temperature (T_e) of the plasma, which is the average kinetic energy of the electrons in the plasma. While some ions are inevitably lost to the walls through this process, those that drift towards the ion extraction grids are accelerated by electrostatic forces in order to generate thrust. Through conservation of energy, it can be shown that the exit velocity of the propellant is proportional to the square root of the electric field.

$$\frac{1}{2}mu_e{}^2 = e\emptyset \rightarrow u_e = \sqrt{2e\emptyset/m} \tag{1-4}$$

There are two types of electrostatic thrusters that are primarily used for space missions: Hall Thrusters and Ion Engines. Both types of thrusters have large flight heritage histories and are used for various purposes. Hall Thrusters consist of an annular discharge chamber with a strong axial electric field for ion acceleration and a radial magnetic field for electron confinement. Meanwhile, ion engines consist of a cylindrical discharge chamber (as pictured in Fig. 1) and accelerate their drive ions through the use of electrically-biased grids. While Hall thrusters have been primarily used for station-keeping (for their larger thrust-to-power ratio), ion engines have been used for both

station-keeping purposes and primary drive purposes on such missions as Deep Space 1 and DAWN missions from NASA[5,6].

The main advantages of these types of thrusters are their specific impulse ratings. Hall thrusters usually have a specific impulse between 1500-2000 s while ion engines have ratings between 1500-5000 s. Compared to their chemically-based brethren, this gives them a distinct advantage in terms of their Δv ratings, which give spacecraft a larger amount of mission variability.

1.1.2. Ion Engines

Ion engines are one of the most popular types of electrostatic thrusters in use today for space missions. Ion engine technology has been researched since the late 1950's through the work of Kaufmann and Reader[7]. Through the development of electron bombardment ionization thrusters by NASA, the first ion engines used propellants such as cesium and mercury, due to their low ionization potentials. However, due to the toxic

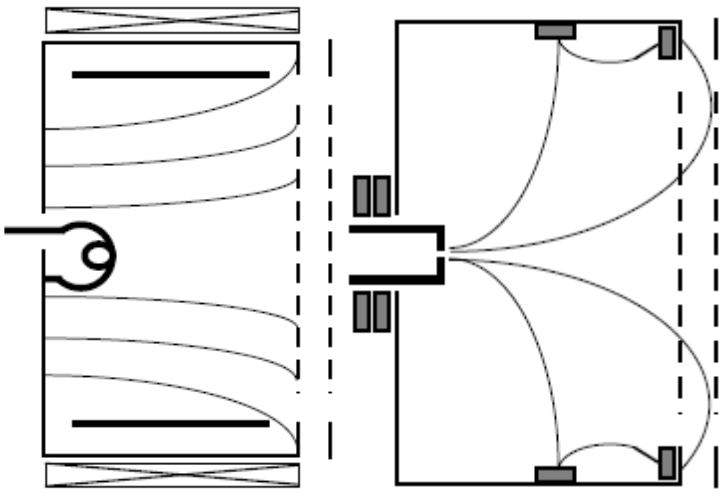

Fig. 2: Kaufman-type (left) and Ring-Cusp type (right) [4]

(and corrosive) nature of these propellants, researchers ultimately moved to noble gas propellants such as xenon and argon. These engines come predominantly in two types of configurations: ring-cusp and Kaufmann-types[4]. The main difference in these types is the magnetic field configuration. Ring-cusp types have multiple magnets positioned around the discharge chamber. The field lines from the magnets form magnetic cusps that produce a strong magnetic field near the edges of the chamber. This, in turn, allows for a large, low-strength magnetic field envelope to form inside the discharge chamber. The low-strength envelope allows for high electron mobility in the chamber to ionize plasma while reducing electron loss to the walls. Meanwhile, Kaufman-type thrusters have a strong axial magnetic field produced from a solenoid.

Regardless of type, both of these configurations share the same basic components: a thermionic cathode for primary electron emission, an anode to energize the primaries, another thermionic cathode placed on the outside for beam neutralization (to keep the environment outside of the thruster charge-neutral) and a gridded assembly that provides for the acceleration of the ions. These ion optics are unique to the ion engine and are usually the limiting factor in the performance of the thruster (which will be expounded on in Chapter 2). Because of the electrical configuration of the ion engine, the anode voltage usually determines the beam's kinetic energy. Ion engines have been designed to generate beam energies up to 1500 eV[4].

Ion optics usually consist of three main components: the screen grid, the accelerator grid, and the decelerator grid. The screen grid is biased to cathode potential in order to repel electrons and attract ions towards the grid holes. The accelerator grid then extracts the ions due to being biased very negative with respect to the screen grid. The

decelerator grid then decelerates the ions as it is held at spacecraft/engine ground. This third grid is in place to protect the accelerator grid from ion backstreaming/erosion stemming from lack of beam focus (or *perveance*). An example of this configuration located in Fig. 3.

Also, as a point of fact, the beam plume of an ion engine (and electrostatic thrusters, in general) generally expands from the beam exit with a half-angle of 15°. Also, through multiple diagnostic efforts of electrostatic thrusters, it has been shown that as the plume propagates downstream from the exit, the plume density falls quadratically[3,4].

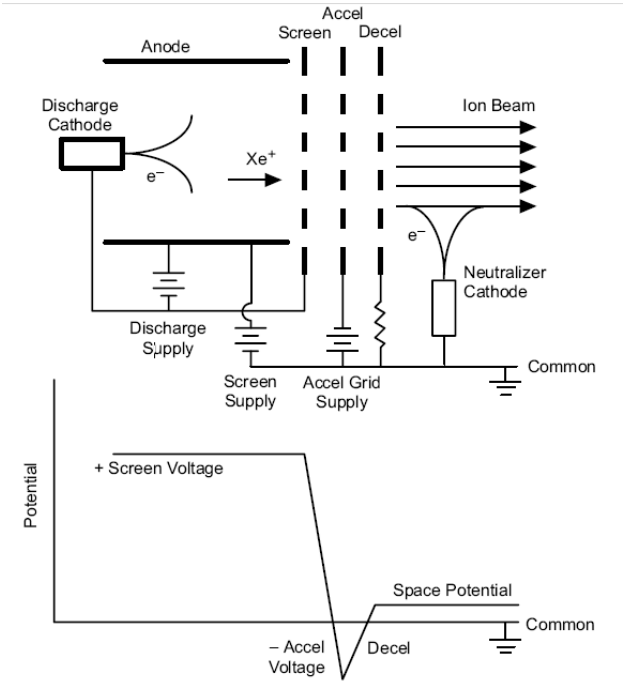

Fig. 3: Typical Ion Engine w/Optics configurations and biases [3]

1.1.3. Hall Thrusters

Hall thrusters have been in development since the 1960's by both the United States and Russia, but the latter focused on developing them to flight status. As mentioned earlier, they consist of an annular discharge region consisting of an anode, a strong axial electric field, a radial magnetic field and a cathode placed exterior to the annulus that provides both the primary electrons and the electrons that keep the environment outside the thruster charge-neutral. The propellant gets ionized through the Hall-Effect by the interaction of the electrons attracted by the axial electric field and the radial magnetic field. This strong electric field that provides the ion acceleration determines the beam energy, designed to be as high as 350 eV[4]. The primary differences of the Hall thruster relative to the ion engine are the lack of internal cathode for primary generation and no gridded accelerator assembly. This means that the lifetime of the Hall thruster is only limited by erosion of the anode. A typical Hall thruster configuration is pictured below.

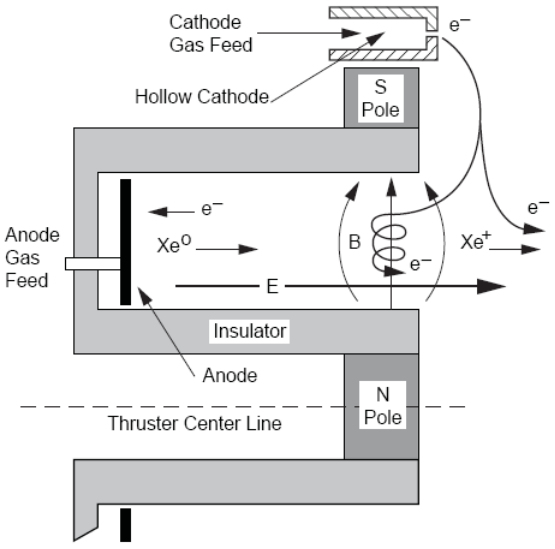

Fig. 4: Typical Hall thruster configuration [4]

1.2. Plume Impingement

With any type of thruster that is placed on a spacecraft, there has to be a considerable effort to negate any potential effects from plume impingement. When thrusters are fired, the exhaust gas creates momentum in order the spacecraft to maneuver itself to a desired position. However, these gases, once released, also have a certain momentum. When these gas plumes impact other surfaces of the spacecraft it causes what is defined as plume impingement. Plume impingement has been known to cause counter-torques on components of spacecraft, such as solar cells, as well as causing attitude misalignments on spacecraft in orbit[8,9].

Plume impingement is always a priority in spacecraft mission design. If the plume impingement causes unwanted moments to occur on the spacecraft, it could be knocked off its desired alignment and therefore require more propellant to compensate for the undue moments, lowering the operational lifetime of the spacecraft by wasting propellant[8]. Plume impingement can also cause other unwanted effects, such as heat loading on the surface of spacecraft[9].

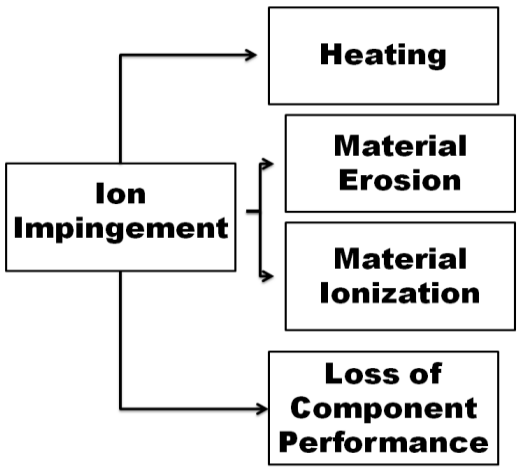

Fig. 5: Description of EP Plume Impingement effects

1.3. Project Premise

As mentioned above, plume impingement is a major factor in space mission design. However, this becomes more complicated with the introduction of an EP plume. Instead of just the possibility of spacecraft misalignment and minor heat

loading, we are now introduced to a very high energy collection of ionized particles that can have a multitude of different effects on any surface they impact. As they are electrically-charged, they can ionize the unintended target surface, causing harm and possible erosion to the target. They can also cause a net charge on the surface that can negatively affect how the components function or how the beam propagates away from the spacecraft. It can also cause overall performance loss from components, such as solar cells and their coverglass.

As missions that require satellite formations continue to rise, the study of formation flight plume impingement situations are required. In addition, since there are a larger number of craft that are using electric propulsion, this can become a serious problem in the realm of formation flight missions that should be explored. There is a wealth of simulation data on plume impingement effects on individual satellite components with limited amounts of experimental citations. However, very few of those studies focus on formation flight fluence levels of ion beams with respect to the distance and orientation from the origin of the beam exit. As a result, the purpose of this project would be to categorize the expected levels of damage from an EP thruster plume using both basic predictive modeling techniques and experimental validation with a variable-energy ion source.

1.4. Project Objectives

This dissertation work will begin to expound on the limited experimental work related to ion beam plume impingement with respect to:

- Aluminum 6061-T4, a commonly used spacecraft alloy

- Solar Cell coverglass with anti-reflective coating

With these experiments, we will be able to paint a picture of the possible outlooks on spacecraft damage caused by EP thruster plumes with respect to material loss and performance on solar cells due to anti-reflective (AR) coating loss. Although not the only contributing factors to spacecraft failures, these two factors are of primary concern as the EP plume can enhance the damage by other phenomenon such as spacecraft charging, micro-meteoroid impacts, and plasma damage from the ambient plasma environment on Earth orbit[10].

This work is also part of a larger collaborative effort between the University of Maryland, Penn State University, and Iowa State University through an AFOSR grant (No. FA9550-11-1-0158). This collaborative research effort intends to study the interactions between a spacecraft and possible plasma environments encountered (LEO, GEO, drive plasmas) and reactive gases, such as atomic oxygen[11]. As part of Maryland's contribution to this collaboration, we are providing the material experiments listed above as well as providing raw beam plume data.

1.5. Dissertation Outline

This collected work will be divided into seven chapters beyond this introductory chapter. Chapter 2 will be a literature survey covering some of the influential work in the field of ion plume damage and cover the most recent experimental work relevant to this dissertation. Chapter 3 will look into the mathematical methods of sputter yield calculation and how they will be implemented throughout this work. Chapter 4 focused on the modelling of the ion plume for the erosion study in this work. Chapter 5 will be a

description of the experimental facilities used to perform the experiment and analyze the material samples. The experiments, and their subsequent results, involving the structural and AR materials will be covered in Chapters 7-9. Chapter 10 will involve applying the experimental results to a test case to examine the overall impact these results could have on an average mission. Chapter 11 will list the overall conclusions and interpretations from the experiments, as well as any recommended future work.

1.6. State of the Art Contributions

The goal of this work is to provide the following to the community as a whole:

- To provide a set of Xenon sputtering yield data for typical EP energy ranges for the following materials:
    - Magnesium Fluoride (MgF_2), an AR coating frequently used for space-rated solar cell coverglass
    - Indium Tin Oxide (ITO), an AR coating that can be utilized in similar situations to the MgF_2 and is also a space-rated coating for solar cell coverglass
- To augment the existing sets of Xenon sputtering yield data for Aluminum
    - Providing a data set for the beam energy, 1500 eV, which would coincide with a specific impulse of nearly 5000 s
- Provide a theoretical curve fit model for all materials involved in this study
    - Aluminum, to include the new experimental sputter data from this study to update or provide an updated curve fit to the existing datasets

    - Provide all-new curve fits for a range of incidence angles for both Magnesium Fluoride and Indium Tin Oxide that have not existed before in literature for their sputter interactions with Xenon
- Provide damage estimates and relations for various maneuvers as a function of incident energy, particle flux, incident angle, and formation distance between two spacecraft in a simple formation

2. Literature Survey

2.1. Sputtering Processes

Sputtering is the process by which the surface of a material becomes eroded, surface atoms are removed, and the morphology of the surface gets modified[12]. This process is one of the natural byproducts from energetic particle bombardment of energy ranges that can naturally occur within an ion beam plume from an EP system. This type of sputtering process, which occurs between the energies of 100 eV to a few keV, is defined as *physical sputtering.*

Physical sputtering occurs when a particle has transferred energy to the target surface that is larger than its surface binding energy. This is usually approximated as the target material's heat of sublimation. Within these energy ranges, there are three different collision regimes: *single knockon*, *linear cascade,* and *spike*. The *single knockon* regime classifies an energetic collision that simply knocks off an incident particle from the target material. *Linear cascade* depicts nearly the same type of collision; the main difference between the two regimes lies in the fact that the *linear cascade* allows for the sputtered particles to be energetic enough to aid in the sputtering process, unlike in *single knockon*. The last category, the *spike regime,* usually calls for heavy ions with large collision cross-sections to cause a high density of sputtered, or recoil, particles to emerge from the target.

$$Y = \frac{\langle \#\ of\ atoms\ removed \rangle}{\#\ of\ incident\ particles} \tag{2-1}$$

One of the useful metrics for sputtering processes is the *sputtering yield*, which is defined in Equation 2-1. This relation becomes relevant when trying to estimate the types

of sputtering damage one can expect from exposures to certain particle energies. Although Equation 2-1 describes the overall definition of sputtering yield, it only becomes relevant when the energetic particle's properties, such as mass and energy, and the target material are taken into account. As a result, extensive testing has been performed over the years to experimentally determine the sputter yields by interactions of many ionic beams to materials of choice[12].

2.2. Plume Impingement on Propulsion Components

As demonstrated above, energetic particle bombardment can be a deciding factor in the design of space missions, even down to the design of their components. As mentioned in Section 1.1.2, the ion engine's main lifetime-limiting factor is its set of optics grids that provide for the electrostatic acceleration of its propellant. These grids can be affected by erosion from both ion and electron impacts to the grids, which affect the overall current extraction.

One of the main design factors of the optics grids comes from the concept of *perveance*. Perveance (Equation 2-2) relates the total extracted current to the voltage difference between the electrodes (in this case, the optics grids)[3,4]. However, to fully appreciate the concept, one must be familiar with the basic law governing the current extraction properties of the optics grids: space charge.

$$P = {I_{beamlet}}\Big/{\emptyset^{\frac{3}{2}}} \tag{2-2}$$

$$j = \frac{4}{9}\epsilon_0 \left(\frac{2e}{m}\right)^{\frac{1}{2}} \frac{\emptyset^{\frac{3}{2}}}{L^2} \tag{2-3}$$

The phenomenon of space charge involves the interaction of electric fields in between two electrodes that have a separation distance. For these two electrodes, for a certain voltage difference between the two electrodes, there can only be a certain amount of current allowed between them before they become saturated, which represents the upper limit of current that can be transferred between the two electrodes. This current, the space charge limited current, between the two electrodes can be calculated using the Child-Langmuir Space Charge law, as seen in Equation 2-3[3,4].

As one can see, perveance and the space-charge limited current are intrinsically related, as the maximum current (per beamlet) that can be focused is directly related to both the space-charge limited current as well as the desired bias differences between the screen and accelerator grids. Perveance can even determine the number of gridlets for an optics set, based on the focusing parameters that are desired. The penalties of not balancing the perveance of the grids can lead to direct damage caused by beam impingement.

There are three types of perveance effects that can be experienced: normal perveance, over-perveance, and under-perveance. Normal perveance involves an optimal focusing of the beam and completely leaves the grids untouched due to the behavior of the electric fields. Over-perveance involves the under-focusing of the beam, which causes a direct impingement of the ion beamlet directly onto the accelerator grids, which will cause both loss of material around the gridlets and additional loss of focus of the beam. Under-perveance describes the over-focusing of the beam and causes the beam to lose

focus downstream due to ion-ion collisions; this causes stray ions from the beam to backstream and impinge on the accelerator grid, again causing erosion and loss of focus.

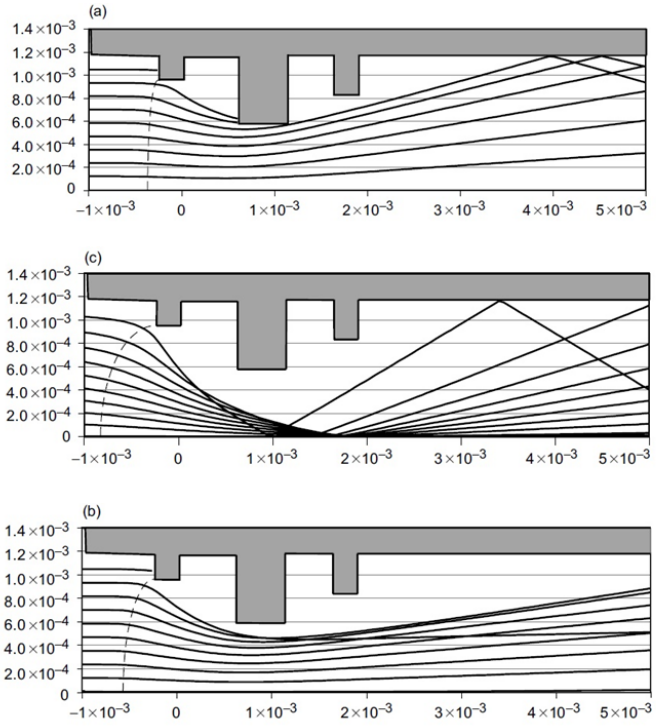

Fig. 6: Examples of Perveance types: Over-Perveance (top), Under-Perveance (middle), and Normal Pervenace (bottom) [3]

Grid erosion is a dominating factor in engine design. Even though extensive design simulations of understanding the optics grids' behavior over operation lifetimes[13,14,15,16], a large amount of time is spent on experimental testing of ion engines to understand each individual's lifetime beam trends. An example of this was the 8200 hour wear test performed by Polk et al., on the NSTAR thruster[17]. The NSTAR thruster, used for the Deep Space 1 mission, was part of NASA's Solar Electric Propulsion Application Readiness (coincidentally, NSTAR) program to establish flight-level maturity in EP technology. As a result, extensive testing was performed on one of

the NSTAR engineering model thrusters. Over the course of the wear test, in situ testing of the grids was performed via laser profilometry to test for wear. Perveance was also measured by monitoring the accelerator current impingement as well as the screen grid currents. Although the thrust was fairly consistent over the course of the wear test, perveance of the grids lowered over time across all the major throttle settings available. The perveance was lowering due to erosion of the molybdenum optics grids, as the accelerator grid lost 10.8 grams of material while developing pit-and-groove erosion patterns. This wear also contributed to increased neutral losses, which slightly lowered both the efficiency and specific impulse of the thruster.

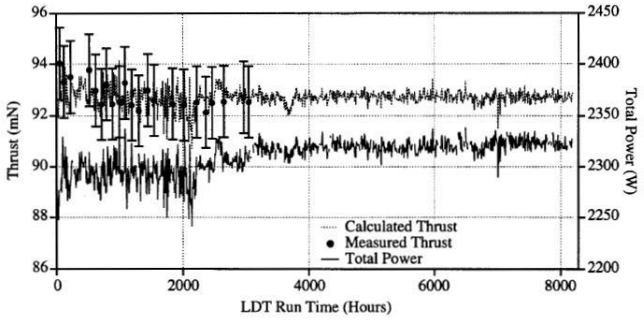

Fig. 7: Thrust levels of NSTAR 8200 hour wear test [16]

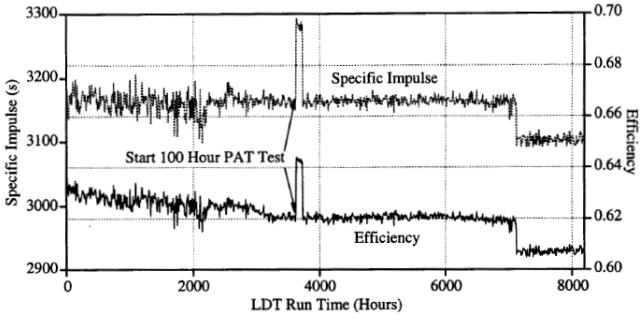

Fig. 8: Specific Impulse and Efficiency over time from NSTAR 8200 hour wear test [16]

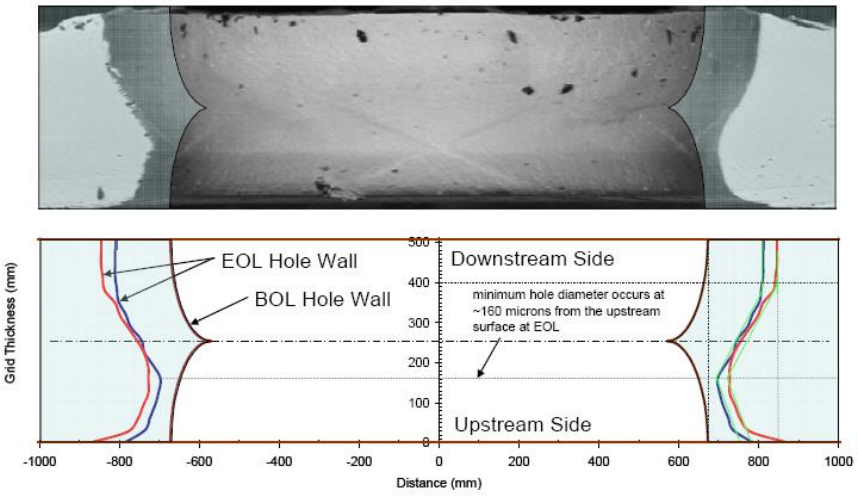

Fig. 9: NSTAR Gridlet Erosion after 8200 Wear Test [14]

Another effort of understanding lifetime performance was carried out on the NEXT thruster, another NASA ion engine being developed to flight status. As a result, a battery of tests have been performed on the thruster during its operational lifetime[18,19,20,21]. The diagnostics included both looking at the performance characteristics over time as well as the ion beam characteristics[22].

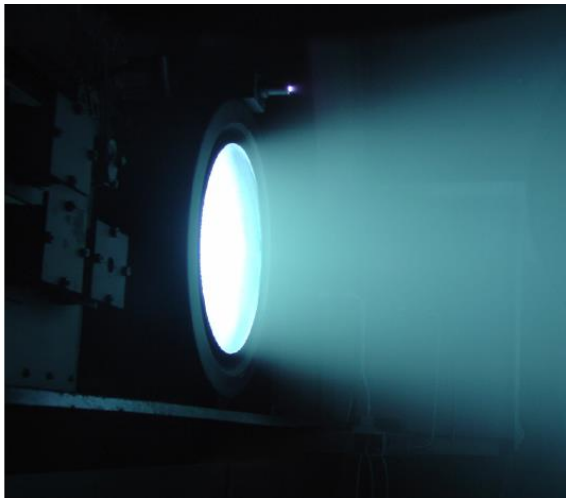

Fig. 10: NEXT Thruster [19]

Concerning the grid erosion, these were observed using CCD cameras that were mounted in the chamber on a vertical assembly. The pictures of the accelerator grid were taken every 250 hours for the first 1000 hours and every 1000 hours thereafter[18]. Although pit and groove erosion did not start to form on the thruster until 677 h[19], the total

erosion seen over 9000 hours showed that the accelerator apertures showed groove erosion close to 30% of the accelerator grid thickness. However, it was also shown that despite the erosion shown, the thrust still remained fairly stable, as well as the specific impulse. The research effort lead by Kamhawi suggested that when the groove erosion would be equal to the grid thickness (resulting in grid failure via structural failure), the NEXT thruster would have used 750 kg of Xenon, which would well surpass the lifetime requirement of 405 kg[18].

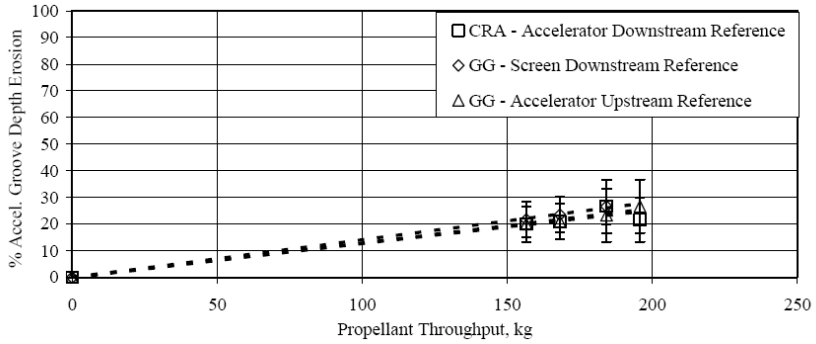

Fig. 11: Accel Grid erosion as function of propellant throughput for NEXT thruster testing [19]

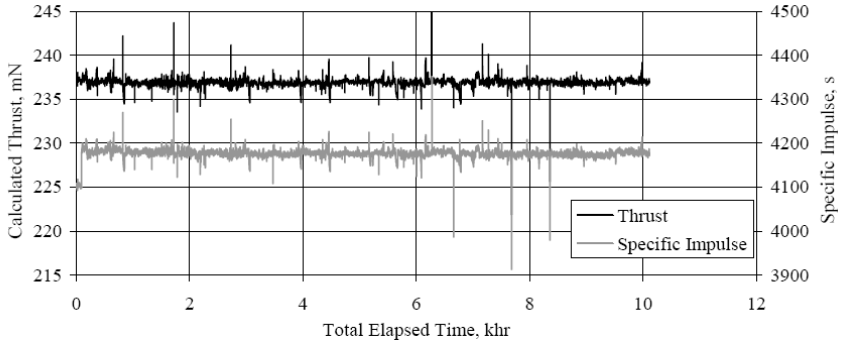

Fig. 12: Thrust and Specific Impulse at Full Throttle as function of time for NEXT thruster testing [19]

Beyond these studies, Wirz looked into the effects of the decelerator grid on the accelerator grid erosion process through simulation efforts via JPL's CEX3D code[22]. Grid erosion can be caused by lack of focus of the ion beam, but can also be caused by Charge Exchange ions (CEX). These ions are typically fast ions that hit a slow neutral and exchange charge by picking up an electron from the slow-moving neutral via collision. This exchange creates a fast-moving neutral particle as well as a very low energy ion. This CEX ion then can be attracted to the negatively-biased accelerator grid and causes erosion (such as pit and groove erosion) by colliding with the grid. These CEX ions are usually caused by the convergence of multiple ion beamlets that cause the main drive ions to be knocked from the beam, lose energy, and then collide with the unionized neutral propellant floating out of the discharge chamber.

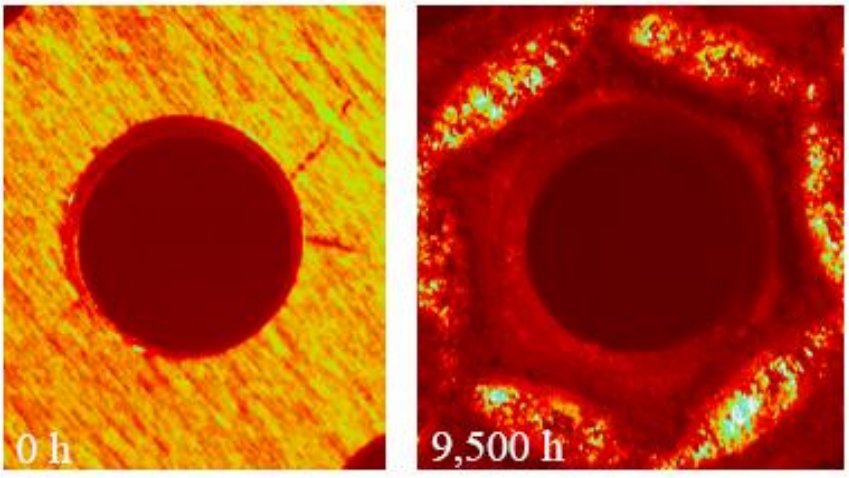

Fig. 13: Accel Grid erosion at 9500 hours compared to Beginning of Life [19]

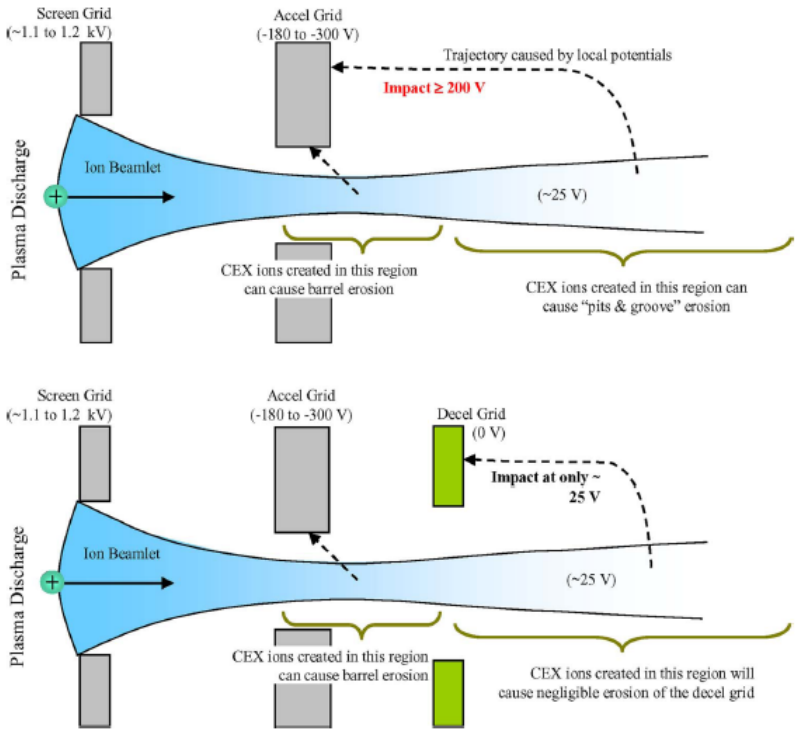

Fig. 14: Explanation of Decel Grid Effects [21]

According to the results from his simulation, using the decelerator grid configuration on the XIPS thruster (another NASA thruster in development), it would reduce the sputter yield by three orders of magnitude. The largest value of erosion rate (a.k.a.: sputter yield), ~275 µm/khr (pit-and-groove erosion), was reduced to practically zero in simulations. The incoming CEX ions that cause the erosion were also energized less due to not being directly exposed to the heavily negative bias of the accelerator grid, reducing the CEX bombardment energies from ~200 to 25 eV. This shows that the 3-grid setup drastically improves ion engine lifetime.

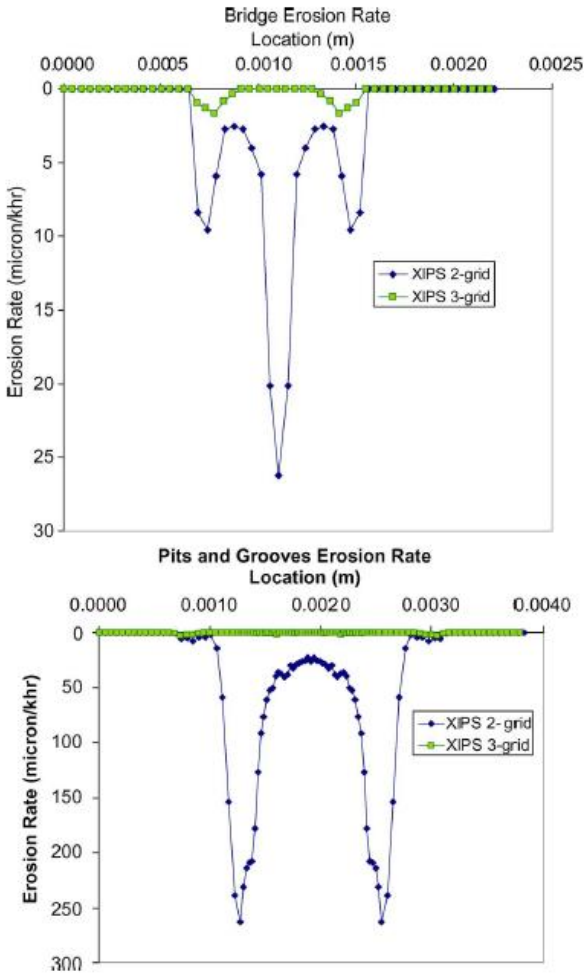

Fig. 15: Erosion Rate comparisons [21]

2.3. Plume Impingement on Spacecraft-Simulated

There have been a vast number of studies looking into the ion plume impingement effects on spacecraft components in order to look at the spacecraft mission lifetime operating parameters and predict the overall health of the spacecraft and payload throughout its life. Special attention is usually paid to the components that directly affect the quality of the mission, such as the payload or the solar arrays, which provide power to the whole craft, including the propulsion system.

A considerable amount of the effort that goes into understanding how the plume interacts with the spacecraft usually occurs after thorough testing of the thruster's beam environment. As such, extensive modeling has been done on Hall thruster plumes and its plasma environment[23,24,25,26,27,28,29]. Plume models are generated with data that is gathered from experimental testing or from actual flight data, such as the SMART-1[25,30,31,32] and Express-A[24,27,33].

For the simulations concerning the SMART-1 mission, the main goal was to develop a model using the Spacecraft Plasma Interaction System (SPIS) that would investigate the Hall thruster plume effects on the satellite's solar arrays. These effects would include spacecraft charging and structural erosion from plume exposure. One of the other main factors for creating this model was to investigate voltage fluctuations (on the order of 6 V) that resulted from solar panel rotation. Although the plume was thoroughly modeled, because of the orientation of the solar arrays with respect to the thruster, only the CEX ions generated from the plume were of any real concern for both erosion and spacecraft charging. Although Wartelski's work did not include any results for erosion, it showed that the plume did in fact cause voltage fluctuations along the solar panel on both the coverglass and interconnectors[25]. The interconnectors interact with the plume by collecting a large electron current from the plume plasma while the spacecraft ground collects a part of the ion current from the plume, resulting in the potential shifts.

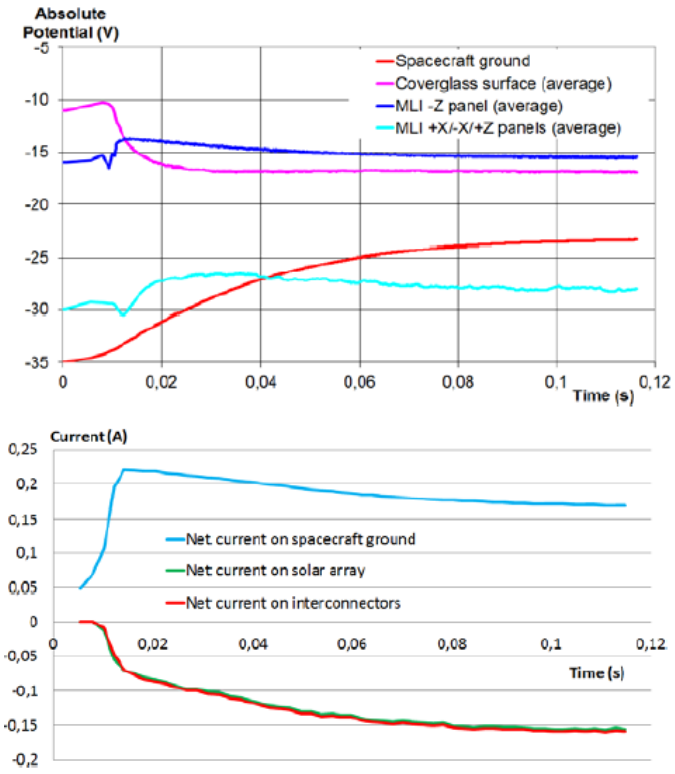

Fig. 16: Potentials (top) and Currents (bottom) on solar cells matched with SMART-1 flight data [25]

The Express-A satellite flight data was collected with the intent of looking at how the plume interacted with the spacecraft in terms of solar array contamination and induced torques on the solar arrays. Mikellides's model looked at two types of particle reflection on the solar panels: specular and diffuse. Specular reflection represented an elastic collision of the plume particle from the surface and that the particle is reflected away from the surface at the same angle and speed that it impacted the surface with; diffuse reflection presents a different situation in which the force imparted on the surface is normal to it and the particles are reflected with a very small velocity. From the flight data and computed torques from the model with both types of reflection, it showed that the solar arrays exhibited different reflective quantities based on the side of the solar

panel. This seemed to agree with previous flight data from earlier Express spacecraft that the surfaces had different reflective properties based on the side it was on. Data from this plume interaction model also looked at the sputter depths on the solar panels; the maximum depth reported was around 9 microns of material during the firing of one of the Hall thruster banks during a maneuver. Some minor deposition of material was reported around the edges of the panel[24].

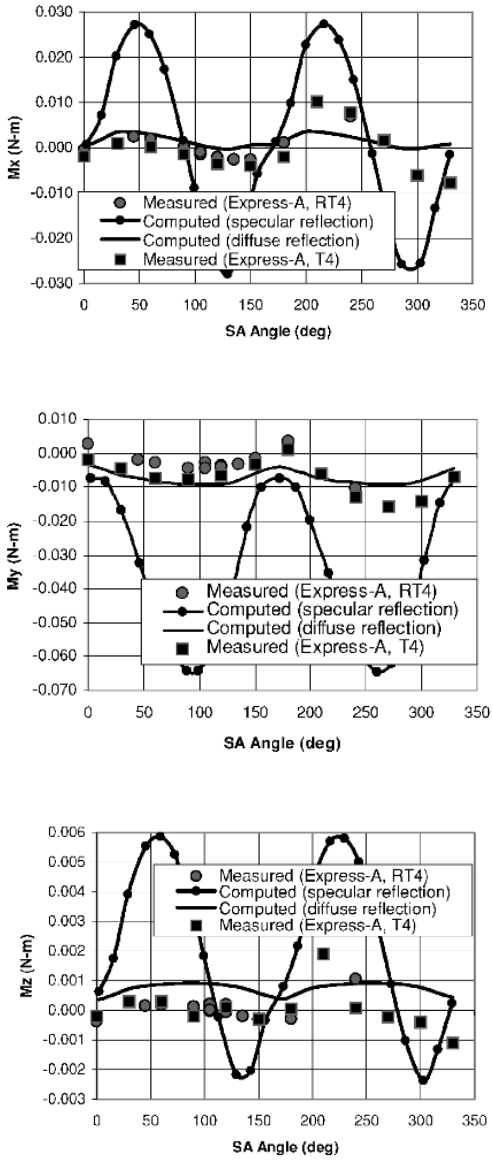

Fig. 17: Torques on Solar Panels with respect to solar array rotation [24]

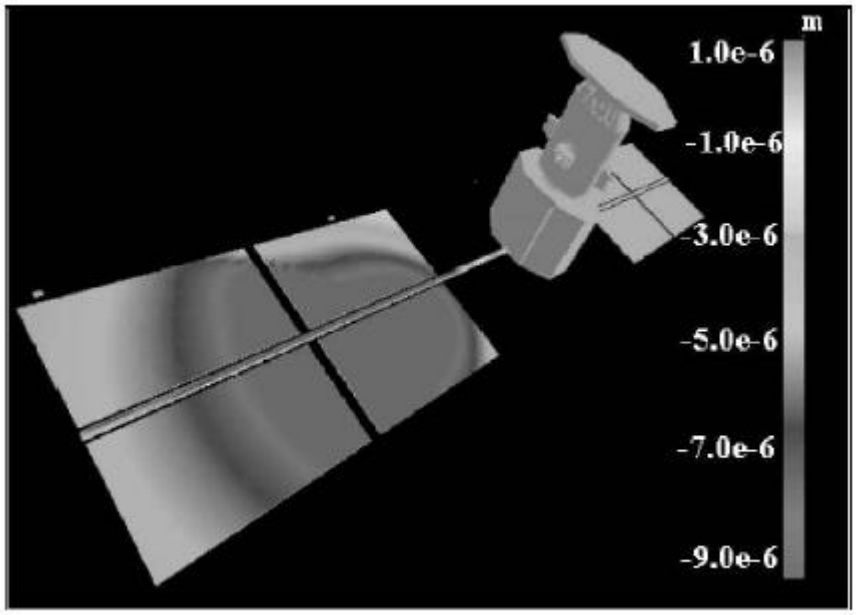

Fig. 18: Sputter depths on simulated Express-A panels [23]

Contamination on the spacecraft from EP plumes is always of high priority and, in addition to the tests performed on Hall thrusters, testing and modeling has been performed on the ion engine plumes as well. A portion of these modeling efforts focused on the NSTAR thruster used for the Deep Space 1 mission and the ion densities that would be generated from ions being sputtered out of the beam and returning to the spacecraft, or "backflow" ions. The efforts of Samanta Roy and Davis, respectively, show that the backflow ion density for the NSTAR is around $3x10^{12}$ #/m^3 and $5x10^{12}$ #/m^3[34,35]. Similar measurements were taken with the Hall thruster and are also on the order of 10^{12} #/m^3 in the back flow region of the craft. The work also shows that an ion density on the order of 10^{12}-10^{14} #/m^3 directly impinging on the solar panels, which may also lead to the large erosion depths seen on the solar array[24].

Although there is a wealth of simulation data concerning the plume's effects on spacecraft, there aren't many works focusing on the effects of the full beam plume on a spacecraft. Roberts and Hastings performed a study in which the effects of plume impingement were investigated. The work looked specifically at two missions: C-Terrestrial Observer Swarm (C-TOS) and TechSat21. Both of these missions employed a single Hall thruster on each of the microsatellites. The majority of the cases involved the microsatellites in cluster formations that were primarily elliptical. However, one formation of interest to this work was a formation in which two C-TOS craft are in a linear leader-follower formation at a distance of 500 m. The results of the investigation concluded that although the maximum particle fluence to the follower was 9.2 x 10^{11} #/s, this was lower than the fluence of the CEX ions from the follower by five orders of magnitude. However, this model did not look at any erosion effects or induced torques on the satellites[2].

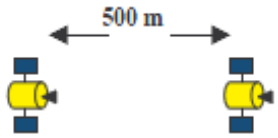

Fig. 19: C-TOS leader-follower formation [2]

In modelling the leader-follower interactions with the spacecraft, Roberts and Hastings had to take into account the magnetic field of Earth and its effect on the plume of the spacecraft. The geomagnetic field, which can be modeled as a dipole, can actually

$$\beta = \frac{Local\ Plasma\ Pressure}{Local\ Magnetic\ Pressure} \tag{2-4}$$

$$\beta = \frac{n_p k(T_e + T_i) + n_o k T_o}{\left(\frac{\left\|\vec{B}_{geo}\right\|^2}{2\mu}\right)} \tag{2-5}$$

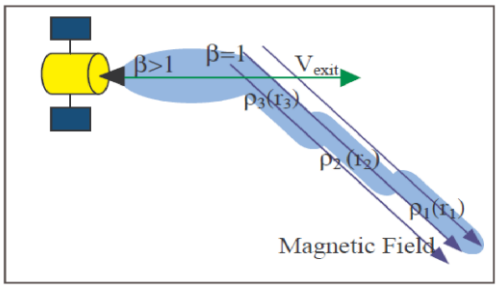

Fig. 20: Graphical representation of magnetic field effect on beam plume [2]

affect the plume of the beam through magnetic pressure. The description of this phenomenon can be summarized through the plasma parameter β, as described in Equation 2-4 & Equation 2-5[2].

As β becomes less than 1, the beam plume will become magnetized by the geomagnetic field and, as a result, will have its velocity redirected. This can prevent the beam plume from actually impinging on the follower in the formation, but as Equation 2-5 suggests, depends on a number of factors. These factors, and a further look into the geomagnetic field, will be available in Chapter 4.

2.4. Plume Impingement on Spacecraft Surfaces-Actual

Although simulation data is quite valuable, there is no substitute for experimental data. There is a wealth of data that can be gained from both laboratory tests and in situ measurements performed on spacecraft. As mentioned above, data has been gathered from flight missions, such as the SMART-1 [32] and Express-A [33] missions. This data collected from the on-board instruments was vital to the development of our understanding of the plume's effect on the on-board system. However, there are large limitations of the in-flight data gathered, the main one being that only certain types of data can be gathered due to the instruments on board the craft.

The SMART-1 mission recorded flight data using its sensor package, the Electric Propulsion Diagnostics Package (EPDP) and the Spacecraft Potential, Electron, and Dust

Experiment (SPEDE). The EPDP consisted of a Retarding Potential Analyzer (RPA), Langmuir Probe, and a Quartz Crystal Microbalance to measure deposited material. SPEDE could be operated as a Langmuir probe or an electric field mode that could monitor the electric field on the craft. However, the EPDP was limited by the fact that it could only monitor the backflow region for ion current. However, the data it collected was still valuable, as it measured a backflow ion density on the order of 10^{13} #/m^3 with peak ion energies of 35 and 65 eV. These densities seem to agree with many reported findings of backflow densities as mentioned above. Their sensors also seemed to pick up a very small amount of deposited material, although the data from that sensor was not fully analyzed at the time of this work[32].

The Express-A satellite, a Russian telecommunications spacecraft, recorded several sets of data over time that looked at the imparted torques on the spacecraft from the EP systems as well as solar cell performance. Although the torques and solar array reflection data were the same as reported earlier, this study from the flight data also looked at the comparison of the predicted solar array power versus the actual power. Their study of the solar array data showed that the performance of the solar array was initially better than expected and, after seven months, the performance on the array

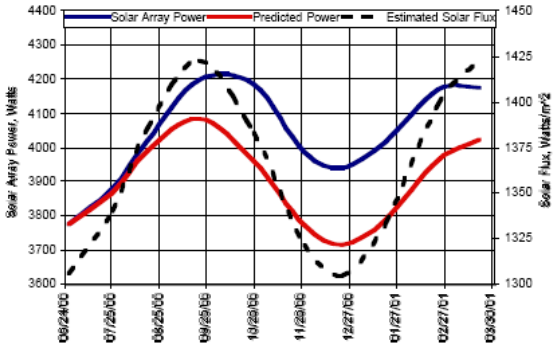

Fig. 21: Solar Array Power measurements [33]

started to degrade. After investigating further, Manzella indicated that the initial boost in performance might have been due to annealing on-orbit, which would then correspond to a higher degradation rate than predicted, indicating significant array erosion[33].

There have also been sets of experiments that used Hall thrusters in a lab setting in order to look at erosion results or interactions with solar cells [34,35,36]. The experiments performed by Pencil showed erosion rates of several spacecraft materials: Silver, Iron, Silicon Dioxide, and Borosil[36]. These experiments were performed while analyzing the plume environment of an SPT-100 near the end of its service life by placing the samples 1 m from the beam exit (radially) while being positioned at a 100° angle with respect to the beam exit. This is clearly in the backflow region of the thrust plume.

A more recent experimental effort of note was performed by Tartz[37] in 2012. Their experiment, which was conceived because of the advent of formation flight missions, sought to gather sputter yield data of Xenon on several materials, including

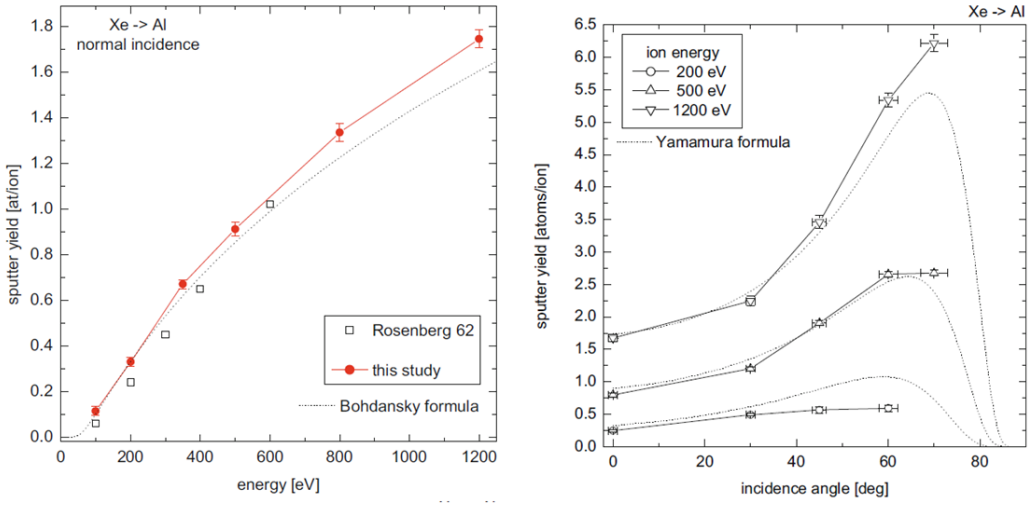

Fig. 22: Xe-Al Sputter Data [37]

Aluminum and Silver. These samples were to be examined via microscopy as well as through mass balance. These experiments utilized a variable-energy RF ion source that produced a current density of 3 mA/cm^2. The current on each sample, which was held 12 cm away from the ion source, had its current measured directly. In order to determine the sputter yield on each sample, the sample would be weighed using a microgram balance. The mass difference, combined with the current data, would allow for the calculation of the sputter yield. The microgram balance had a precision of 10 μg. Although Xe-Al sputter data is not new, there are very few sources. This paper, to date, is the second source of Xe-Al sputter in energy ranges lower than 100 keV. The sputter yields closely agree to the previously published Rosenberg[38] set. It also expands the previous data to a range of 1.2 keV, where the sputter yield is shown to be near 1.7 atoms/ion. It is of note that the sputter yields provided by the graphs in Fig. 21 are somewhat larger than the Eckstein theoretical model for Xe-Al sputter[12].

2.5. Formation Flight

As mentioned in Chapter 1, the desire for formation flight spacecraft missions are on the rise as the need for more innovative and economical approaches to these missions are becoming available with today's technology. However, as close proximity formation flight is still a relatively new concept for space missions, there is a need to understand and verify many concepts of formation flight, such as navigation, formation keeping, and propulsion control (to name a few). Besides looking at simulated missions (such as the earlier mentioned C-TOS mission), there are a few missions that will focus on keeping multiple spacecraft together in order to accomplish their objectives.

One such mission is the Proba-3 mission, which is a technology demonstrator mission from ESA that will demonstrate the validity of formation flight for science applications while it performs observations on the Sun's corona.[39,40,41]. This spacecraft will be in a leader-follower formation that varies in inter-spacecraft distance (ISD) from 100 m at the orbit apogee to 1.2 km in orbit perigee. In order to maintain the formation, the spacecraft employ sets of oriented microthrusters that use hydrazine as a propellant. As a result of the thruster choice, a very small total delta-v budget (1.6 m/s) is employed for the maintenance of the formation[40].

Another spacecraft mission employing a formation is the PRISMA mission based in Sweden[42,43,44,45,46,47]. This mission, launched in 2009, utilizes two satellites that orient themselves in an adjacent formation at close ranges (~100 m) and out to a leader-follower formation at larger distances up to 2 km. Like Proba-3, this satellite also uses hydrazine as its main propellant with a delta-v budget of 170 m/s[43]. Also, like Proba-3, this mission is a technology demonstrator to advance the viability of formation flight systems.

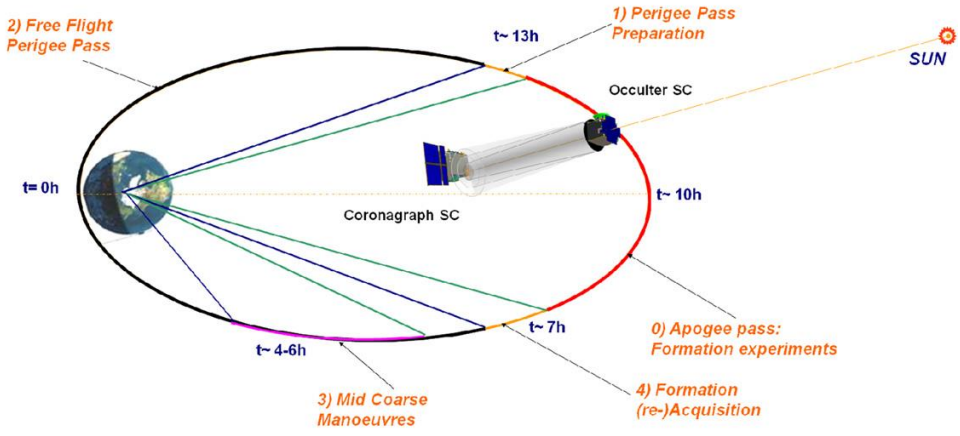

Fig. 23: Proba-3 Orbital Activities Schematic [41]

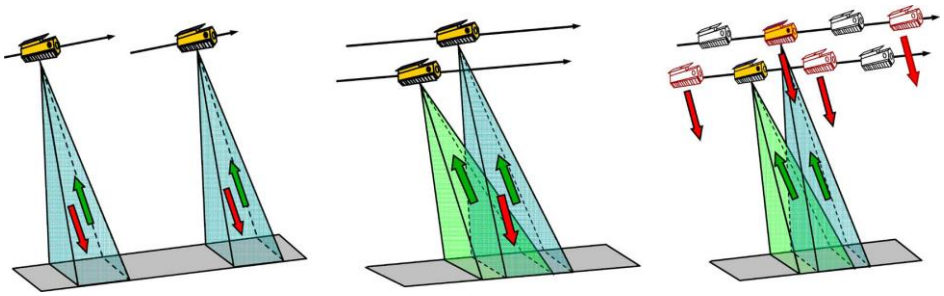

Fig. 24: Depictions of pursuit monostatic (left), bistatic (middle), and alternating bistatic (right) formations for TanDEM-X [48]

TanDEM-X, another testbed mission for formation flight, is an add-on for the TerraSAR-X mission in an attempt to expand its capabilities to include digital elevation modeling (DEM)[48,49,50]. These spacecraft are capable of multiple formation types, such as a monostatic formation (in which the craft are in a leader-follower formation at a distance of 30-50 km), a bistatic formation (in which the craft are within 2 km of each other but have a slight vertical separation), an alternating bistatic formation (aka the HELIX formation), and simultaneous transit. Each of these formations require very tight control (with the exception of the pursuit monostatic formation) and require accurate propulsive control.

The common thread among all three of these missions is that they currently use hydrazine cold gas thrusters that can offer highly accurate thrust bursts for formation keeping. However, each of the applications of these propulsion schemes differ immensely because of the individual needs of the spacecraft. With Proba-3, each of its hydrazine thrusters provide 1-N bursts for thrust and formation control, yet the delta-v budget is miniscule compared to the other two missions. However, Proba-3 needs to fire its thrusters more frequently because of the formation restrictions. A much greater delta-V

would be available to the mission if the monopropellant thruster were replaced with an EP system. However, the thrust duration would need to be greater due to the lower thrust levels. Because of the restrictions on short duration thrusting, it may be difficult to schedule maneuvers that would avoid all levels of plume impingement, so the potential for surface damage becomes clear.

2.6. Solar Array Research

Within the past two years, there have been recent advances in the studies of plume interaction with space-rated equipment, particularly solar arrays. One of the ways that the ion plume can affect the solar cell is by the erosion of the AR coating on the coverglass, which can affect overall efficiency.

A multi-faceted experimental effort carried out by Hoang involved exposing certain samples with 5, 10, and 15-year doses of ion fluence using a lab-mounted Hall thruster[51]. This test was carried out in three phases, but the results of interest were carried out in phase one of the experiment. The samples involved in phase one were exposed to UV radiation and 30 keV proton beams to simulate the environmental exposure seen in the GEO space environment. After simulated environment exposure, they were exposed to a xenon ion beam at 250 and 350 eV at normal incidence and 75° for solar cell coverglass sputtering. The final result after the 5 year dosage was a 2.4 micron erosion of the MgF_2-coated coverglass, as well as a change in the transmission properties[51].

This transmission change was caused by the erosion of the MgF_2 coating on the coverglass according to an in-depth study related to the Hoang group's effort on the

sputtering of the AR coating and its effect on the change in transmission properties by Yalin[52]. In this effort, experiments were performed to determine the sputter yields of MgF_2 mounted on CMG coverglass from Qioptiq at energies below 350 eV. This work used an ion source to impinge the samples in a climate-controlled environment to ascertain the normal incidence sputter yields as well as the angular yields of the material at 250 eV.

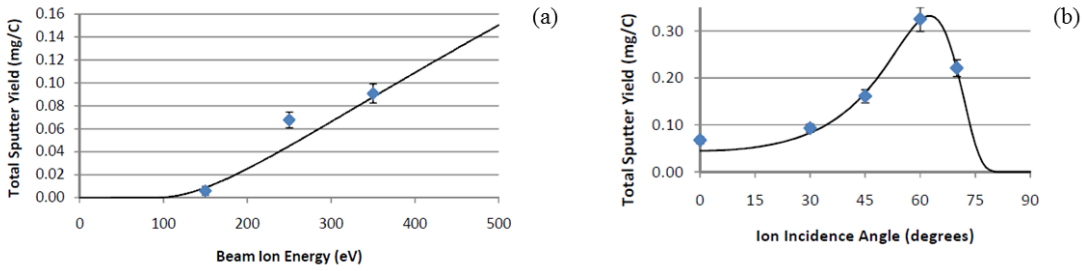

Fig. 25: (a): Normal incidence sputter yields for MgF_2; (b), Angular sputter yields for MgF_2 at 250 eV [52]

After exposure to the beam, the transmission properties of the coverglass were shown to have reduced by 4-6% in the 400-750 nm light wavelength range. Based on their experiment observations, this would result in a 3-5% overall cell efficiency drop based purely on the erosion of the AR coating alone.

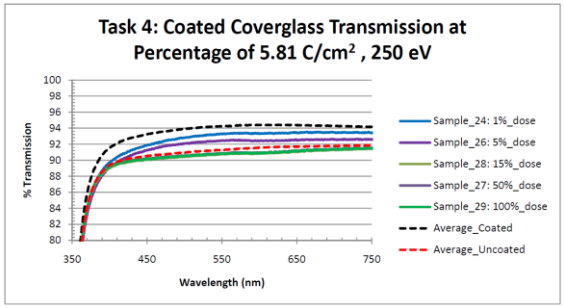

Fig. 26: Transmission readings based on ion exposure [52]

Another sputter study looking at transmission changes in AR coating was performed by Hu[53]. This study involved exposing ITO samples to an ion plume at varying energies and incidence angles to look at the transmission change as a result of erosion. This study also indicated transmission loss with erosion, with a 3-4% transmission loss after ~70 nm of erosion. They also reported erosion rates for the material, but only in arbitrary units.

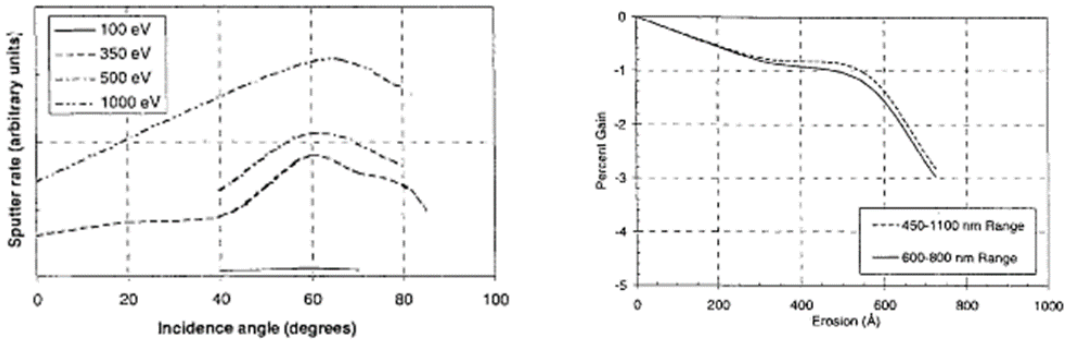

Fig. 27: ITO Angular Sputter Trends (right), ITO Transmission Changes (left) [53]

A more recent effort was undertaken by Varney looking at biased solar cells immersed in an arc jet plume as well as a Kaufman source. These solar cells were biased up to 300 V relative to spacecraft ground. Current collection trends were examined at different solar cell biases as well as being immersed in a low-density Xenon plasma later on. The experiments showed that the collected currents from the solar cells depend on the electron temperature of the plasma impinging on it. The experiments also show that the solar cells collected currents up to 150 μA from Hall thruster plasma at densities of 10^{12} #/m^3, which is comparable to the ion densities that would be seen from the backflow region of a Hall thruster[54].

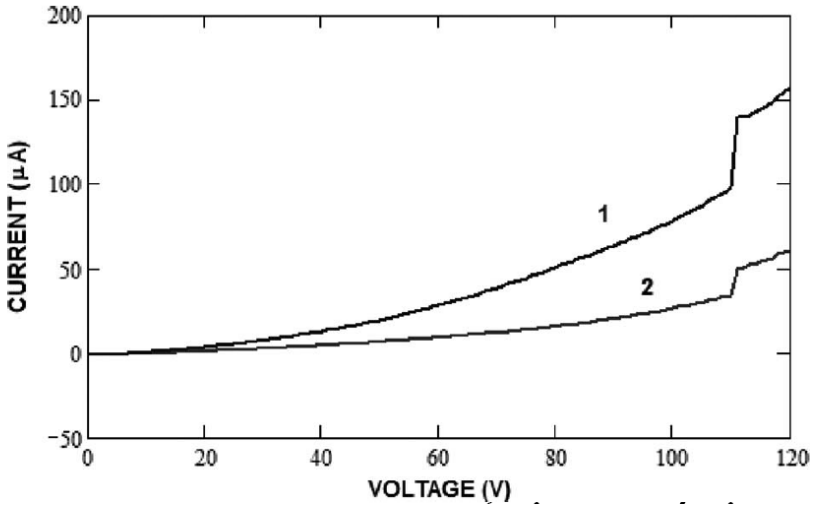

Fig. 28: Average Current collected on solar array [54]

3. Mathematical Modeling of Erosion

3.1. Overview

In order to validate the experimental results as well as to forecast the effects of plume impingement on spacecraft, a mathematical model was developed. This requires a model that will look at two things: 1) the ion-material interaction from the plume impingement on the target and 2) the overall expected beam fluence from the EP thruster in question. This model utilizes elements of the Eckstein/Bohdansky normal incidence sputtering model, Yamamura angular sputtering model, the sputter target's lattice geometry, as well as fluence trends observed by numerous lifetime test of the SPT-100 thruster. The model's main goal is to predict the amount of sputtered material based on the ion beam's current, incident energy, and angle of incidence. This model will also take into account the divergence of the ion plume, which will heavily influence the impact fluence based on the formation distance of the spacecraft. This chapter will look at the basic assumptions of the generic sputtering calculation from plume exposure and the fluence modeling aspect.

3.2. Sputtering Models

As defined by Eckstein in Section 2.1, sputtering is the process by which the surface of a material becomes eroded, surface atoms are removed, and the morphology of the surface gets modified. For the energy regime of this experiment, the sputter regime that we are most interested in is the *physical* regime, in which the surface is primarily modified through direct collision with the energetic particle. The Eckstein method itself is a modified version of the Bohdansky sputter yield estimating calculation.

3.2.1. Sputtering Yield Calculation-Eckstein

The basic mathematical definition of sputtering yield is shown as Equation 2-4[12]:

$$Y = \frac{\langle \#\ of\ atoms\ removed \rangle}{\#\ of\ incident\ particles} \tag{3-1}$$

As long as the amount of incident particles that impact the target are known, a sputtering yield can be derived. As such, the Eckstein method of calculating sputtering yield is based on a curve fit through experimental data that is published on the interaction in question.

$$Y(E_0) = q s_n^{KrC}(\varepsilon) \frac{\left(\frac{E_0}{E_{th}} - 1\right)^{\mu}}{\frac{\lambda}{W(\varepsilon)} + \left(\frac{E_0}{E_{th}} - 1\right)^{\mu}} \tag{3-2}$$

$$\varepsilon = E_0 \left({}^{m_2}/_{m_1 + m_2}\right)\left({}^{a_L}/_{Z_1 Z_2 e^2}\right) \tag{3-3}$$

The equation is primarily a function of the energy of the incident particles, E_0, but also depends on the following: the nuclear stopping power of the KrC potential, s_n^{KrC} (Equation 3-4), the threshold energy of the target, E_{th}, and the fitting parameters of q, λ, and μ[12]. Equation 3-4 itself is a function of the reduced energy of the interaction (Equation 3-1) and the Lindhard screening length, a_L (Equation 3-5), based on the atomic number, Z, of both the incident and target atoms. The author would like to point out that the term $W(\varepsilon)$ is just a shortcut term that refers to the denominator of Equation 3-4[12].

$$s_n^{KrC}(\varepsilon) = \frac{0.5 \ln(1 + 1.2288\varepsilon)}{\varepsilon + 0.1728\sqrt{\varepsilon} + 0.008\varepsilon^{0.1504}} \tag{3-4}$$

$$a_L = \left(\frac{9\pi^2}{128}\right)^{\frac{1}{3}} a_B \left(Z_1^{\frac{2}{3}} + Z_2^{\frac{2}{3}}\right)^{-\frac{1}{2}} \tag{3-5}$$

Combining all of the above elements generates a logarithmic-looking curve that peaks at a certain energy level and then begins to fall, which usually occurs in the hundreds of keV. An example of a fitted curve is shown below in Fig. 29.

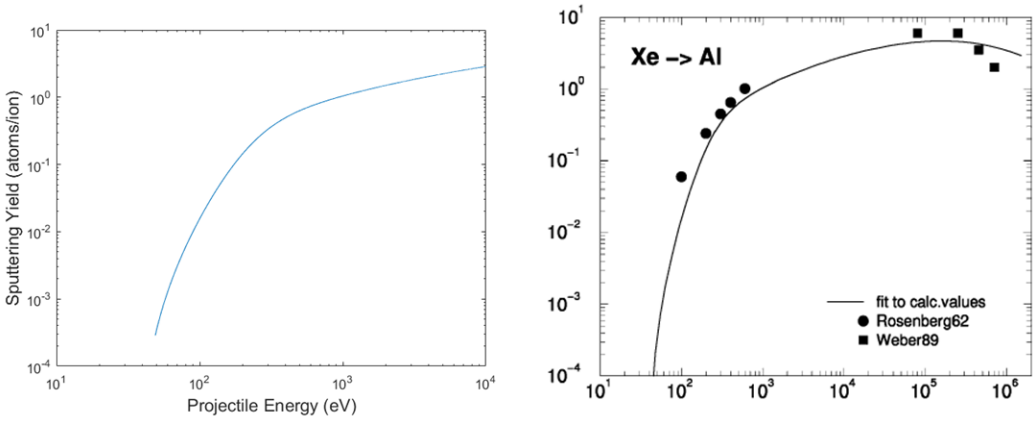

Fig. 29: Comparison of Calculated Eckstein Curves; MATLAB Model (left), Referenced Data (right, [12])

3.2.2. Sputter Yield Calculation-Bohdansky

Although the Eckstein method is partially based on experimental data, the Bohdansky equation[55,56] involves using the properties of the nuclear stopping power of the interaction, the incident energy of the reaction, E_0, and a scaling factor, Q, based on either experimental data or a best fit to arrive at the sputter yield estimation. A notable aspect of this calculation method is that it is purely dependent on the ratio of the threshold energy, E_{th}, to the incident energy of the beam particle. It only relies on one scaling factor, unlike the Eckstein method, which relies on three fit parameters in order to generate the proper curve fit. The Bohdansky equation, as seen in Equation 3-6, typically

generates a similar curve to the Eckstein fit, but is usually around 15-30% larger, depending on the scale factor's sensitivity[55].

$$Y(E_0) = Qs_n^{KrC}(\varepsilon)\left[\left(1-\frac{E_{th,Boh}}{E_0}\right)^{2/3}\left(1-\frac{E_{th,boh}}{E_0}\right)^{2}\right] \quad (3\text{-}6)$$

As mentioned before, both the Bohdansky and Eckstein sputter models rely on Eth as a parameter for the fit. Eth, the threshold energy, represents the lowest energy at which the interaction's sputter yield begins to increase by orders of magnitude to an appreciable level of sputter. Normally, this parameter is found theoretically. It can also change with the types of interaction the target can experience as well as having the possibility to change with incidence angle[57]. It is generally shown that the theoretical threshold energy is an order of magnitude lower than the actual threshold energy. The actual threshold energy can be found, through more recent studies[37], by fitting existing sputter yield data for that specific interaction and treating it purely as a fitting parameter.

3.2.3. Erosion Modelling

In order to analyze the results of the experiments, the samples themselves have to be measured through a profilometer, which will nominally limit our analysis to 2-D profiles that we must use in order to compare to the projections from this model. As a result of this, a few assumptions must be made for the model: 1) The exposed profile is approximated as a square cross-section; 2) The exposure area to the beam is under a constant bombardment from ions at a specific energy for a given time; and 3) The beam spot size of the ion beam is much larger than the exposure cross-section.

For assumption one, the simulated cross-section is rectangular as the sample itself is a rectangular slab and the sample has a shield leaving a rectangular cross-section exposed to the beam. Nominally, if the density of the ion beam is sufficient, it should generate a uniform erosion profile that is consistent with the area left exposed by the sample shields. However, it is also known that ion sputtering will generate a non-uniform sputter profile near the edges of the etch shield. As the sputtering interaction begins, material begins to be removed from the selected region. However, as material under the sputter shield is removed, secondary sputter interactions will form near the edges as the area under the sputter shield will have expanded and cause a small expansion under the shield. This is known as anisotropic sputtering[12].

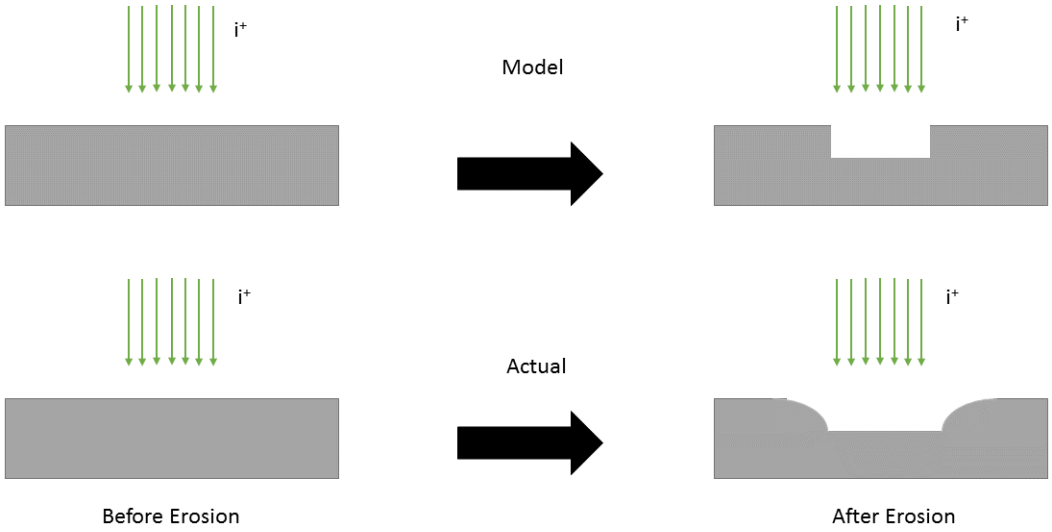

Fig. 30: Erosion Profiles, Model vs. Actual

For assumption two, the beam is assumed to produce a constant stream of ions at a specified current. This assumption is fairly reasonable but is not exactly accurate; during operation of the ion source, the beam current seen by the sample contains very

minor fluctuations that do not exceed 5% of the beam current. However, this is quite small compared to the overall current hitting the sample so this assumption can be made to simplify calculations. The justification for assumption three also relates somewhat to the second. The beam spot size of the ion source is much larger than the sample's exposed surface area. As a result, not only will the beam bombard the entirety of the sample surface area, it will also be fairly constant and consistent as the samples will be within the core of the beam, where it is assumed that the velocity of the ions are uniform.

Now, with the main assumptions of the model in hand, the severity of the sputter can now be evaluated. Each material has a density that can be used to estimate the number of atoms removed from the material. If the depth of the erosion is known, we can then estimate the number of atoms removed using the exposed cross-sectional area, the mass density, and the molecular mass of each of these materials. This relation is shown in Equation 3-7 below.

$$N_{atoms} = \frac{\rho_{sample} d_{erosion} A_{exposed}}{m_{atomic}} \tag{3-7}$$

With the number of atoms sputtered from the material as a result of the ion impingement, we now have to relate this back to quantities that we can use for the sputter estimation. For this, we can relate the number of atoms lost back to the sputter yield, as shown in Equation 3-8. The main variables that we control are as follows: the energy of the incident particles, E_0 (in eV); the rate of ions impacting the target, F (in ions/sec); the exposure area, A_{ex} (in m^2); and the time of exposure, t (in sec). The dependent quantities

are: sputtered atoms (N_{atoms}) and sputter depth ($d_{erosion}$, in meters). Equations 3-9 and 3-10 relate the exposure area current to the impact rate.

$$N_{atoms} = Y(E_0)Ft \quad [atoms], \quad Y(E_0) = {}^{N_{atoms}}/_{Ft} \left[\frac{atoms}{ion}\right] \tag{3-8}$$

$$I_{sample} = envA_{exposed} \ [A] \tag{3-9}$$

$$F = {}^{I_{sample}}/_{e} \ [m] \tag{3-10}$$

When combined with the sputter yield estimation from either the Eckstein curves, Bohdansky curves, or collected data, these present a mathematical estimation of the sputter depth based on the independent variables mentioned above. Since noble gases are being used for the impingement experiments, the calculation of such is very straight-forward as the samples themselves should not be reactive. However, the Eckstein method is noted that the sputter yield fits for noble gases are subject to inaccuracies up to 30%[11].

3.2.4. Angular Sputtering

For beam incidence angles > 0°, an angular fit formula has to be used in order to approximate the sputter yield for the appropriate interaction of incident and target particles. Eckstein has also developed an angular fit equation for these instances. However, due to the lack of fit parameters for the equation, the original Yamamura[37,58] angular fit equation was used. This equation (Equation 3-11) is reliant on fit parameters, as well. However, these parameters (Equation 3-12 and Equation 3-13) are only reliant on the ratio of threshold energy to the incident energy. This also helps to

determine the optimal sputter angle, α_{opt}, through the use of this ratio as well, shown in Equation 3-14.

$$\frac{Y(\alpha, E_o)}{Y(0^\circ, E_o)} = (\cos\alpha)^{-f} exp\left[f((1-\cos\alpha)^{-1})\cos\alpha_{opt}\right] \tag{3-11}$$

$$f = f_{sig}\left(1 + 2.5\left(\frac{\int}{1-\int}\right)\right) \tag{3-12}$$

$$\int = \sqrt{E_{th}/E_o} \tag{3-13}$$

$$\alpha_{opt} = 90^\circ - 286.0\left(P\Big/\sqrt{E(eV)}\right)^{0.45} \tag{3-14}$$

$$P = \left(\frac{a}{R_o}\right)^{3/2}\left[\frac{Z_1 Z_2}{\left(Z_1^{2/3} + Z_2^{2/3}\right)^{1/2}}\right]^{\frac{1}{2}} \tag{3-15}$$

It is important to note that the parameter *P* (Equation 3-15) is actually converted from Yamamura's fit parameter, Ψ, which is the ratio of *P* and the root of incidence energy. By itself, *P* is an abbreviation used by Tartz for the product of Ψ and the root of the incidence energy, which is also dependent on the lattice parameter of the material as well as the Lindhard screening length, a_L (Equation 3-5).

3.2.5. Matlab Model

With both normal incidence and angular incidence models covered, the sputter yield curves from both types of models for any material can be generated using either fitted experimental data or fit parameters generated from previous research. Using simple arrays representing the incident energy range of the beam (E_0), range of incident angles (θ), and the fit parameters represented in each of the equations, graphs can be recreated like the examples below in Fig. 30 using parameters from Rosenberg and Tartz[13]. It is important to note that there is an approximately 30% difference between the Eckstein and Bohdansky models, with the Eckstein model usually under-predicting the sputter yield.

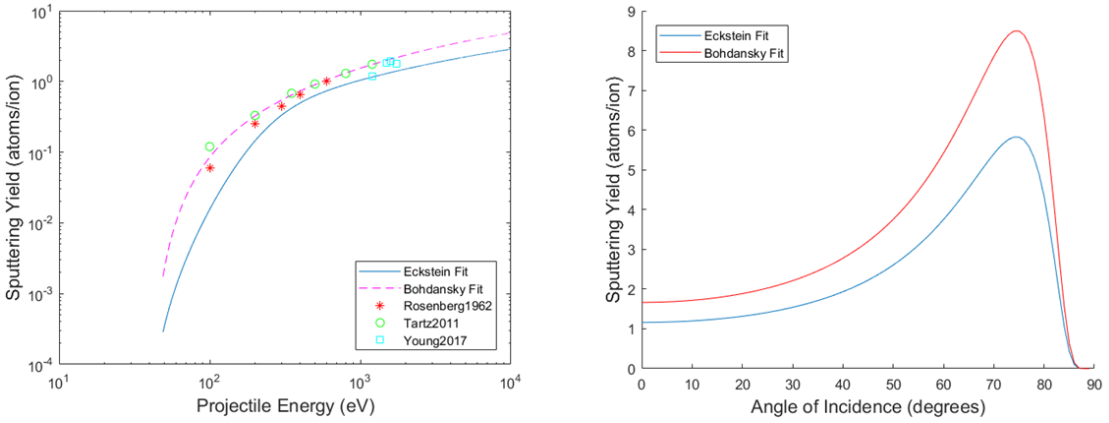

Fig. 31: Normal Incidence Xe→Al Sputter model (left); Angular Incidence Xe→Al Sputter model (right)

One other important note is that the angular fit models from this work are based on the Bohdansky curve-fit values for those specific incidence energies. As shown in Section 3.2.4, the Yamamura curve fit encompasses all angles from 0-90˚. Although the experimental values could be used for the origin point of the model, for ease of analysis, the 0˚ incidence point will be based on the Bohdansky fit for the appropriate material.

This will represent only a slight shift from the normal incidence data, as it only serves to shift the curve on the y-axis of the model.

With the theoretical models of the materials examined in this work, we can then estimate the amount of material lost through plume erosion using the equations from Section 3.2.3. We can then track the progression of the erosion based on the time of exposure and the amount of ion fluence impacting the target area.

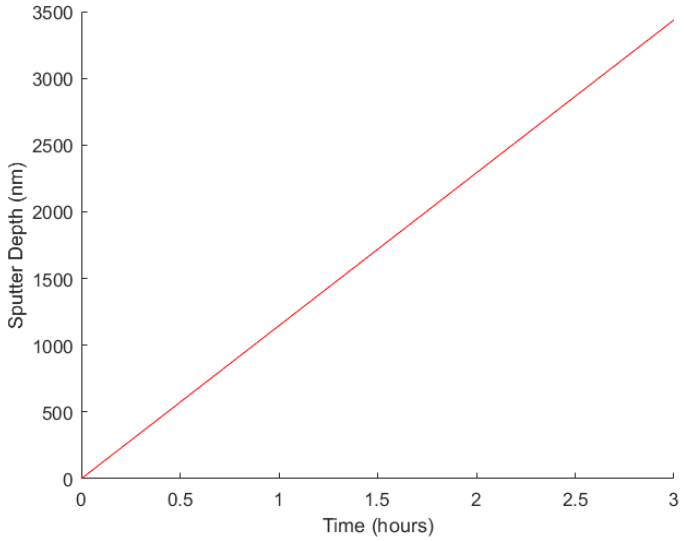

Fig. 32: Sample Erosion case

As shown in Fig. 32, the erosion profile is linear as long as the ion fluence is constant and there are no unexpected changes to the surface area (such as orientation change, catastrophic damage, etc.). This trend holds for all sputter yields and energies, although the slope of the erosion profile will change based on the sputter yield of the material at the conditions of the ion plume.

Another important factor to note for this modeling technique is that both the Bohdansky and Eckstein methods are only taking into account single component

interactions (i.e.: Xe→Al or Xe→Ag, etc.). While the Eckstein method can be expanded to handle alloy targets by just using the composition percentage of the target and applying the appropriate sputter yields to the components, it is not meant to handle compound targets[12]. Presumably, since the Bohdansky method is only slightly different, the same assumption can apply to this method, as well. This means that for properties such as Equation 3-3, which has an atomic number dependence, this method cannot apply directly to analyzing compound materials, such as MgF_2. To this end, this effort aims to expand the capabilities of these methods by introducing an effective atomic number based on the composition of the compound targets. This Z_{eff} will be provided by the method used by Murty[59] as shown in Equation 3-16. For reference, *f* in this equation represents the fraction of the individual atom in the compound.

$$Z_{eff} = \sqrt[2.94]{{f_1}^{2.94}(Z_1)^{2.94} + {f_2}^{2.94}(Z_2)^{2.94} + \cdots} \tag{3-16}$$

4. Mathematical Modelling of Ion Plume

In order to accurately gauge the lifetime of the components of a spacecraft during orbital maneuvers, several factors have to be known: the duration of exposure to the ion beam, the incident energy of the beam, the impact fluence of the beam to the different surfaces of the spacecraft, and the incident angle of these impacts to the target surfaces. However, as mentioned in Chapter 2, the ion plume can be redirected due to geo-magnetic field interference. As a result, the plume has to be modelled in order to find the projected path of the plume and whether it intersects with the spacecraft in any way. This magnetic field interference can also change the incident energy of the beam which will be explained in Chapter 10.

To anticipate the changes in the beam throughout orbital maneuvers with a wide test matrix of conditions, it is desirable to analyze the conditions throughout the specific orbit of the spacecraft as it progresses through the maneuver. To this end, we are looking at orbit-stabilizing maneuvers that will keep it in a specific orbit, but can also be expanded to orbit-raising maneuvers, as well. This chapter will look into each section of the Matlab model that will calculate the approximate duration of beam impact and how it achieves this.

4.1. Orbital Modelling

To look at the effects of the plume as it propagates from the leader spacecraft to the follower, we have to look at the local properties of the geomagnetic field and its effect on the plume as it propagates from the leader to the follower. However, as we're looking at multiple orbital parameters and formation distances in the test matrix, we will need to be able to look at the plume as it propagates throughout the entirety of the maneuver.

At the start, we will look at the basic orbital parameters of the maneuver, from the semi-major axis, *a*, of the orbit, to the starting co-ordinates of the leader spacecraft. From the semi-major axis, we can calculate the period of the orbit, as in Equation 4-1, with μ representing the Gravitational Parameter of Earth, 3.986×10^5 km^3/s^2. The period can then be used to determine the time-steps for the Matlab model to use. We can also use this to determine how many orbital steps we want to look at over the duration of the examined orbit as shown in Equation 4-2 and Equation 4-3.

$$T = 2\pi\sqrt{a^3/\mu} \tag{4-1}$$

$$n = \frac{360}{\left(36 * \left(10 * n_{accuracy}\right)\right)} \tag{4-2}$$

$$t_{step} = T/360n \tag{4-3}$$

$$\theta_{offset} = 180\left(\frac{d_{formation}}{1000}\right)\Big/\pi a \tag{4-4}$$

$$h = \sqrt{\mu\left[abs\left(a(1-e^2)\right)\right]} \tag{4-5}$$

Looking at the leader's starting point, we can use the desired formation distance to learn the follower's coordinates. From the leader's true anomaly, θ, we can determine the

true anomaly of the follower spacecraft by looking at the desired formation distance and finding the new true anomaly using the arc length of the orbit as displayed in Equation 4-4. Now that the locations of the spacecraft are known, we can also look at the other parameters that are important to us, such as the angular momentum of the orbit, *h*. This would be found through utilization of the semi-latus rectum of the orbit, as illustrated in Equation 4-5.

Now that we have the initial positions of the spacecraft, we need to put the coordinates into the geocentric frame. In order to do this, we can place the coordinates into the Perifocal coordinate frame using angular momentum, the eccentricity of the orbit, *e*, and the true anomaly of the spacecraft. The following equations outline the process described in this paragraph.

$$\vec{r}_{coef} = \frac{h^2}{\mu}\left(1 \Big/ \left(1 + (e\cos\theta)\right)\right) \ , \ \ \vec{r}_{peri} = \vec{r}_{coef}\begin{bmatrix}\cos\theta \\ \sin\theta \\ 0\end{bmatrix} \qquad (4\text{-}6)$$

$$\vec{v}_{coef} = \mu/_h \ , \qquad \vec{v}_{peri} = \vec{v}_{coef}\begin{bmatrix}-\sin\theta \\ e + \cos\theta \\ 0\end{bmatrix} \qquad (4\text{-}7)$$

Once we have the position vector in the Perifocal frame, we can then place it in the Geocentric coordinate frame. To do this, we use a rotation matrix to transform the coordinates into the appropriate coordinate frame. This rotation matrix utilizes the following orbital parameters: inclination *i*, the right ascension of the ascending node Ω,

and the argument of perigee ω. These matrices are represented by Equation 4-8 through Equation 4-10.

$$R_3(\omega) = \begin{bmatrix} \cos\omega & \sin\omega & 0 \\ -\sin\omega & \cos\omega & 0 \\ 0 & 0 & 1 \end{bmatrix}, \quad R_1(i) = \begin{bmatrix} 1 & 0 & 0 \\ 0 & \cos i & \sin i \\ 0 & -\sin i & \cos i \end{bmatrix},$$
$$R_3(\Omega) = \begin{bmatrix} \cos\Omega & \sin\Omega & 0 \\ -\sin\Omega & \cos\Omega & 0 \\ 0 & 0 & 1 \end{bmatrix} \tag{4-8}$$

$$Q_{geo-peri} = R_3(\omega)R_1(i)R_3(\Omega), \quad Q_{peri-geo} = \left[Q_{geo-peri}\right]^T \tag{4-9}$$

$$\vec{r}_{geo} = Q_{peri-geo}\vec{r}_{peri}, \quad \vec{v}_{geo} = Q_{peri-geo}\vec{v}_{peri} \tag{4-10}$$

4.2. Magnetic Field Modelling

After plotting every step of the observed orbit, we now need to look at the local geomagnetic conditions of the orbit in order to determine the local magnetic pressure. To do this, we incorporate the magnetic model of Earth into the analysis. As mentioned in Chapter 2.3, the geomagnetic field of Earth can be simplified to a dipole approximation, with a slight polar tilt from the geographic poles of Earth represented by θ_M, the tilt of the

$$\vec{B}_r = -2\cos\theta_M \left(M/R^3\right)\hat{r}$$

$$\vec{B}_\theta = -\sin\theta_M \left(M/R^3\right)\hat{\theta} \tag{4-11}$$

$$\vec{B}_\varphi = 0$$

magnetic poles. A polar form of the coordinates was provided by Roberts and Hastings[2] which is represented in Equation 4-11. A simple representation of the fluctuation of the magnetic field along a test orbit is displayed in Fig. 33.

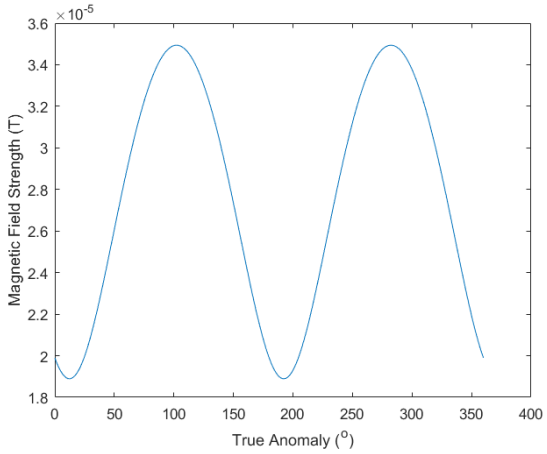

Fig. 33: Magnetic Field Strength along test orbit: a=7478 km, e=0, i=63.4°, RAAN=0°

For the purposes of our Matlab model, we convert the magnetic field equations from polar to Cartesian for ease of analysis within the geocentric coordinate frame. This equation listed below is an integral part of the Matlab model looking at the local magnetic field strength to determine the magnetic pressure.

$$B_x = \frac{3M}{\left\|\vec{r}_{magnetic}\right\|^5}(xz)$$

$$B_y = \frac{3M}{\left\|\vec{r}_{magnetic}\right\|^5}(yz) \tag{4-12}$$

$$B_z = \frac{M}{\|\vec{r}\|^5}\left(3z^2 - \left\|\vec{r}_{magnetic}\right\|^2\right)$$

From here, as in the previous section, we will need to convert the magnetic field to the geocentric frame in order to analyze the local field strength in the proper coordinate frame. This leads to a similar rotation matrix with the main exception that this rotation is around the magnetic axis, θ_M. This will allow for the conversion to the geomagnetic frame. The rotation matrix and process are represented by Equation 4-13 through Equation 4-15.

$$R_{magnetic} = \begin{bmatrix} \cos\theta_M & 0 & \sin\theta_M \\ 0 & 1 & 0 \\ -\sin\theta_M & 0 & \cos\theta_M \end{bmatrix} \tag{4-13}$$

$$\vec{r}_{geofield} = R_{magnetic}\vec{r}_{geo} \tag{4-14}$$

$$\vec{B}_{geo} = R_{magnetic}\vec{B} \tag{4-15}$$

4.2.1. Beta Modelling

As mentioned in the previous section, the local geomagnetic conditions can be used to find the magnetic pressure at a specific set of coordinates. The magnetic pressure, as described in Equation 4-16, is the energy density of the magnetic field in that region of space. For convenience, Equation 2-5 is reproduced here as Equation 4-19. β determines the flight path of the plume due to the influence of the magnetic pressure. Of note is that β is not affected by the directed kinetic energy of the beam; only the plume density and component temperatures of the beam have an effect on the particle pressure. The ion temperature, although present, is usually sufficiently low to be considered negligible in this parameter's calculation.

$$P_{mag} = \left\|\vec{B}_{geo}\right\|^2 \Big/ 2\mu_0 \tag{4-16}$$

$$\vec{v}_{exit,\beta>1} = \vec{v}_{beam}\left[-\left(\frac{\vec{v}_{geo}}{\left\|\vec{v}_{geo}\right\|}\right)\right] \tag{4-17}$$

$$\vec{v}_{exit,\beta<1} = \frac{\vec{v}_{exit}\cdot\vec{B}_{geo}}{\left\|\vec{B}_{geo}\right\|^2}\vec{B}_{geo} \tag{4-18}$$

$$\beta = \frac{n_p k(T_e + T_i) + n_o k T_o}{\left(\frac{\left\|\vec{B}_{geo}\right\|^2}{2\mu_0}\right)} \tag{4-19}$$

If β>1, the plume will travel normally as it propagates from the beam exit, with its normal exit velocity and appropriate plume expansion, shown as Equation 4-17. However, if β<1, the plume becomes magnetized and will begin to be guided in the direction of the magnetic field, with the plume velocity represented by Equation 4-18. With the geomagnetic field model in place, we can now look at β at any point around Earth's magnetic sphere of influence and we can look at the trending of β for the following parameters: orbital altitude, plume density, and the ISD of the leader-follower spacecraft.

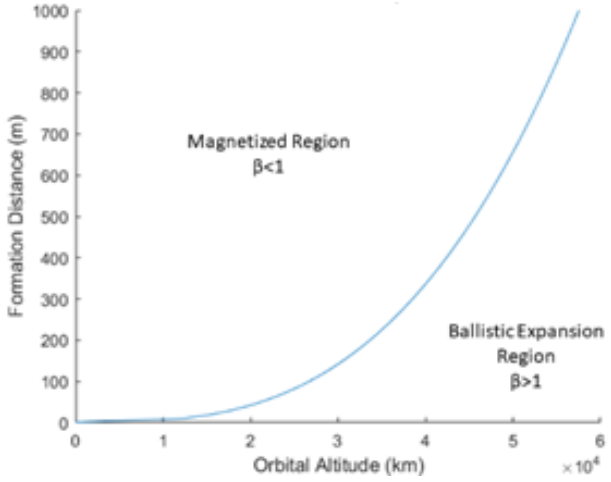

Fig. 34:Sample Beta Transition Graph

In Fig. 34, we examine the general trend of the location of the β transition point as a function of orbital altitude at a fixed electron temperature and plasma density. The blue line in the graph represents β=1, with the region above the line being β<1 (or magnetized region) and the region below representing β>1 (or the ballistic expansion region). As the altitude increases, the magnetic field strength drops off quadratically; likewise, as the formation distance grows, the beam fluence drops off quadratically, as well. This trend is to be expected as per Equation 2-5. Also, since β increases proportionately to both plasma density and electron temperature, the ballistic expansion region grows under the β transition graph as shown in Fig. 36.

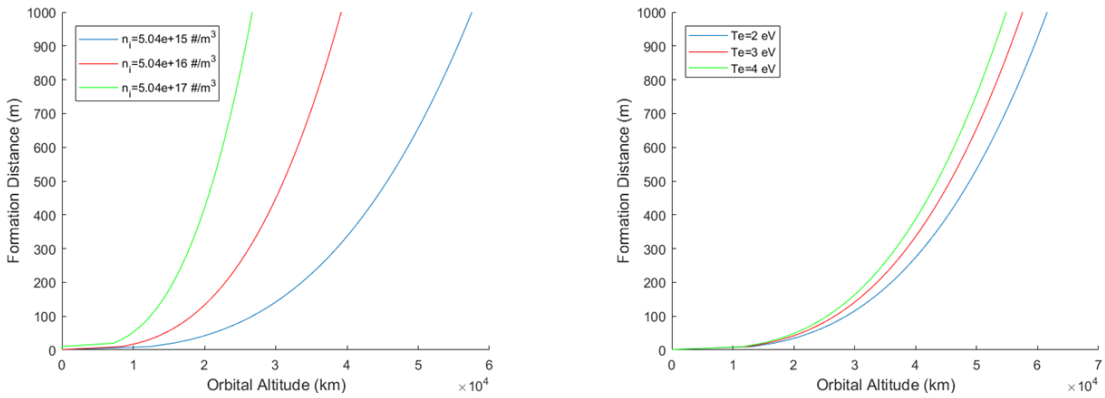

Fig. 36: Beta Transition w.r.t. n_p @ T_e=3 eV (left); Beta Transition Point w.r.t. T_e @ n_p=5.04x10^{15} #/m^3 (right)

The other dramatic source of change for the β transition is a primary function of orbital altitude, due to the quadratic weakening of the magnetic field strength as altitude increases. From this trend alone, formation flight with plasma thrusters face much greater risks at altitudes higher than LEO, especially in the region beyond GEO. Fig. 36 features an annotated version of Fig. 35 with markers for the boundaries of LEO and GEO altitudes.

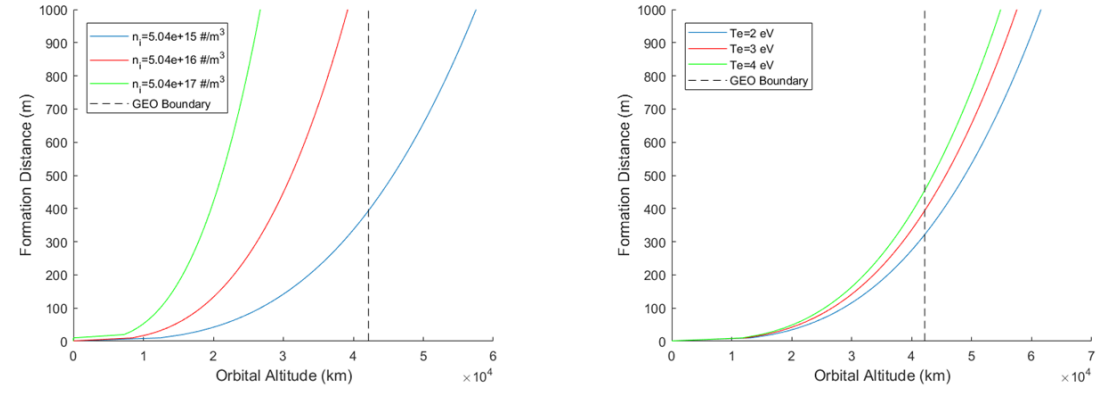

Fig. 35: Beta Transition w.r.t. n_p @ T_e=3 eV (left); Beta Transition Point w.r.t. T_e @ n_p=5.04x10^{15} #/m^3 (right)

Although electron temperature (T_e) is directly proportional to the plasma pressure, it does not have as dramatic of an effect on the location of the β transition as does the plume density. This is solely because of the types of ion plumes examined in this work; most electrostatic ion plumes have an electron temperature of ~1-3 eV, such as the plume of the SPT-100.

As for the SPT-100 thruster itself, the standard plume density is shown to be orders of magnitude larger than provided in the sample curves from Fig. 36. According to Goebel and Katz[3], the nominal operational beam current of the SPT-100 is 4.5 A, which is around 2.83x10^{19} #/m^3. However, for the effort from Pencil looking at the SPT-100 performance, the calculated standard operating density is around 1.73x10^{19} #/m^3, which is still in the predicted operating regime from Goebel[36]. At this much larger plume density, we can now see a drastic change in the location of the β transition. The effect of the quadratic reduction of the magnetic field is now more noticeable along with the quadratic reduction of plume density from the beam exit.

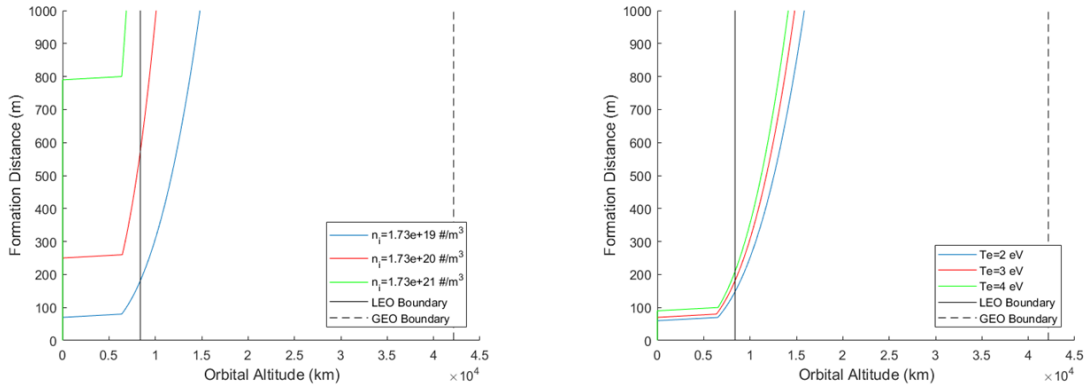

Fig. 37: Beta Transition w.r.t. n_p @ T_e=3 eV (left); Beta Transition Point w.r.t. T_e @ n_p=1.73x10^{19} #/m^3 (right)

Although the region of GEO and beyond is still a viable threat to the safety of the follower spacecraft from plume impingement, we now have a much larger region of threat beyond LEO, as well. This region between LEO and GEO, where the majority of spacecraft operate, has now become a danger zone for mission operations from plume impingement, with the right amount of plume density. But, with the utilization of such thrusters as the SPT-100 for station-keeping and orbit raising, the threat from plume impingement can now be fully realized.

4.3. Ion Plume Fluence Modelling

After the orbital conditions have been recorded and the local magnetic conditions have been verified, we now need to figure out the impact density of the plume, if any. As such, this effect needs to also be accounted for in the plume propagation. As referenced earlier, the beam density falls off quadratically the farther away from the beam exit plane. This effect can be observed directly by utilizing the Randolph and Park formula for the current density trending of the SPT-100[36]. Plots of the current density from this fit confirms the quadratic reduction, as shown in Fig. 38. As a result, a simple $1/r^2$ is inserted into the beam current term for the propagator to account for the density dropoff.

$$j = \frac{R^2}{r^2}\left[k_0 exp\left(\frac{-(\sin\theta)^2}{k_1^2}\right) + k_2 exp\left(\frac{-\theta^2}{k_3^2}\right)\right] \tag{4-20}$$

$$k_0 = 0.31732\ \tfrac{mA}{cm^2},\ k_1 = 0.48743,\ k_2 = 1.2279\ \tfrac{mA}{cm^2},\ k_3 = -11.073^{\circ 2}$$

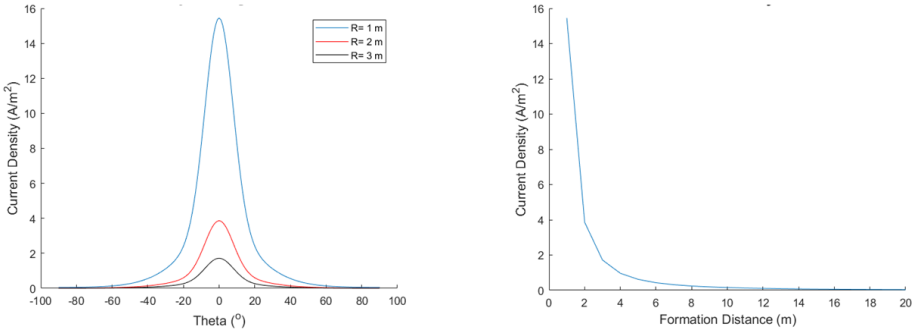

Fig. 38: (left) Plume Density profile of SPT-100, (right) Thrust Axis Density Profile

4.3.1. Fluence-Energy Relation

As mentioned in earlier sections, the parameter β is a measure of the local plasma pressure of the plume. A major factor of this is the particle density of the plume, as it is directly proportional to the pressure as shown in the numerator of Equation 2-5. However, as seen in Equation 4-19, it has also been shown that the kinetic energy of the beam does not directly factor into this parameter.

$$I = env_{beam}A = en\sqrt{2e\varphi/m_i}\,A \tag{4-21}$$

$$I = e^{\frac{3}{2}}nA\sqrt{2\varphi/m_i} \tag{4-22}$$

$$I \sim \sqrt{\varphi} \tag{4-23}$$

$$v_{beam} = \sqrt{2e\varphi/m_i} \tag{4-24}$$

Yet, if the kinetic energy of the beam does change, if the particle density remains constant, the particle fluence of the beam will change. Equation 4-24 shows the beam

velocity of the plume as derived from standard energy relations. We also know, from standard electric relations, that the beam current can be defined as a function of the beam velocity, given that the particle density and impact cross-sectional area are known. We can then insert Equation 4-24 into this relation, as shown in Equation 4-24 and is even more evident with further manipulation in Equation 4-21.

From this, it can be derived that, given the density and area remain constant, the current is then a function of the kinetic energy of the beam (Equation 4-22). Also, as the fluence of the beam is defined as the beam current divided by the electric charge (Equation 4-25), it can be derived that the fluence of the beam is then also proportional to the kinetic energy of the beam, as seen in Equation 4-26. Thus, we can determine the beam fluence for all energies based on an initial operating particle density and beam energy of a specific ion source, as seen in Equation 4-27 and Equation 4-28.

$$f = {}^{I}\!/_{e} = e^{\frac{1}{2}} nA\sqrt{{}^{2\varphi}\!/_{m_i}} \tag{4-25}$$

$$f \sim \sqrt{\varphi} \tag{4-26}$$

$$f_{beam} = f_{\varphi}\sqrt{{}^{\varphi}\!/_{\varphi_0}} \tag{4-27}$$

$$I_{beam} = I_{\varphi_0}\sqrt{{}^{\varphi}\!/_{\varphi_0}} \tag{4-28}$$

4.4. Matlab Model

In order to estimate the damage potential of the beam plume throughout a variety of conditions, it is essential to calculate all the local parameters throughout the maneuvers that the spacecraft are performing. For this, not only do the local conditions of the spacecraft need to be calculated at every timestep, the plume propagation needs to be observed within each timestep as well. As mentioned in Chapter 4.2.1, the plume has the potential to be diverted from its original flight path due to geomagnetic interference within the formation distance. However, even if the plume is diverted, the plume still has an associated velocity along the magnetic field line, as shown in Equation 4-18. However, since this diverted plume can still impact the spacecraft, we must be able to map both the spacecraft position and the relative position of the plume of the leader spacecraft at every point in the maneuver. Utilizing MATLAB, we are able to look at any maneuver from the leader and the follower spacecraft with a certain formation distance and calculate the impact time of the plume throughout the maneuver, given the local conditions.

Before the model is explained in detail, there are a few assumptions that must be taken into account: 1) For analysis purposes, the orbits examined in this work will be circular orbits, although this theory can be extended to more general orbits; 2) the

$$t_{hit} = \frac{\left(\frac{d_{formation}}{1000}\right)}{v_{beam}} \tag{4-29}$$

$$tol = \frac{d_{formation}}{1000} \sin 15° \tag{4-30}$$

follower spacecraft will have a tolerance window in which if any part of the plume hits, the model will count it as a hit on the spacecraft; 3) no transition effects of the parameter β will be taken into consideration, as it is outside the scope of this work; 4) the plume is modeled as a packet with a center of mass that can be easily observed in the model while assuming the basic expansion angle of the plume wherever $\beta>1$.

The impingement model takes in a particular orbit to examine with these conditions: starting point (in the form of true anomaly), orbital altitude (in km), eccentricity, inclination, RAAN, the argument of perigee, the beam energy (in eV), and the formation distance that's anticipated. Because of the nature of the leader-follower formation, the follower spacecraft must be within the same orbit as the leader, although at an offset position in the orbit, which the model determines based on the formation distance via Equation 4-4. The model also determines the initial beam velocity based on the kinetic energy of the beam, as shown in Equation 4-24.

From here, we need to determine how to break up the orbit into its timesteps. From the initial orbital conditions, the period of the orbit can be calculated. Based on the number of increments that we want to observe, we can then easily split this up into manageable timesteps for the program. Also, based on the kinetic energy of the beam and the formation distance of the spacecraft, we can calculate the expected time of impact of the plume. However, since we also have these parameters, we can determine the expected interaction field of the spacecraft. Since the model is looking at the propagation of the plume in a rudimentary sense, a sphere of influence, or tolerance window can be added to the follower spacecraft. This is based on the non-geomagnetically manipulated beam divergence angle and the formation distance, which is outlined in Equation 4-30. As

expected, this tolerance window will grow or shrink based on the anticipated ISD of the formation. From here, we can calculate the local magnetic field strength based on the projected orbit that insert into the model (as covered in Section 4.2).

We now have the established environmental factors the model has to take into account. Now, we must examine the orbit step-by-step in order to determine whether the plume impacts the follower spacecraft. To observe the plume propagation, we look at it in its own timescale between origin and its expected impact time, as calculated in Equation 4-29. Looking at a time interval *dt*, we can determine the plume's position relative to the leader spacecraft via simple kinematics. However, the model's job is to determine what the value of β is at the plume's local position. If $\beta>1$, the velocity will follow from Equation 4-17 and perform as normally expected; if $\beta<1$, the velocity will then follow Equation 4-18 and become guided by the geomagnetic field, diverting its direction. This can cause the plume to still hit the spacecraft based on the local conditions or to miss the follower entirely. However, based on the follower spacecraft's sphere of influence (SOI), if the plume intercepts that volume, the model considers it as an impact on the spacecraft, due to the potential width of the plume after the geomagnetic interference.

$$\vec{r}_{plume,leader} = \vec{r}_{geo,leader} + \left(\vec{v}_{exit,leader} * dt\right) \tag{4-31}$$

These impacts are then represented within a hit graph, or a graph that shows the intersections between the plume and the SOI of the target spacecraft. This graph takes all intersections of the sphere into account, including at intermediate distances between the beam exit and the target. This graph, in effect, shows the potential distances that plume impingement can occur for a given set of orbital conditions, based on the target's SOI.

However, it is important to note that the only impacts that count as a “hit” for the purposes of the model are the hits that occur at the specified distance under observation. An example of a hit graph is pictured in Fig. 39.

In this graph, it can be seen that the plume impacts the follower spacecraft over the entire orbit. The yellow sections of the graph represents the intersection with the SOI. However, shown on the graph between the ISD of 140-250 m, hits are shown in these intermediate regions, as well. However, as mentioned above, this graph depicts any intersection of the plume with the SOI in yellow. As such, only impacts at the maximum ISD are considered to be “hits”.

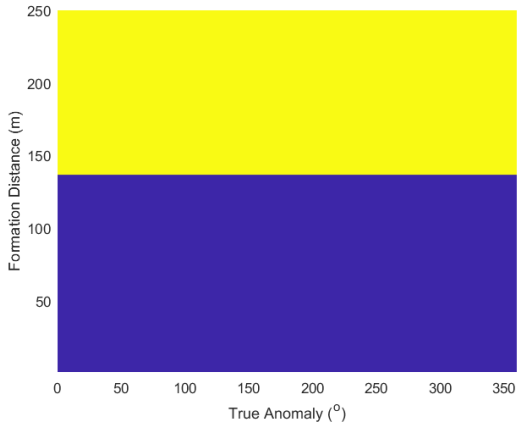

Fig. 39: Sample Hit Graph from MATLAB model

Based on the number of hits from the analysis, the model then calculates the number of impacts recorded throughout the orbital maneuver. We also assume, for convenience, that if the plume impacts the spacecraft within that timestep the plume must impact for the entirety of that timestep. Taking this into consideration, we can calculate the total amount of time that the plume will impact the spacecraft. This time can be taken to the erosion model for analysis of sputter depths as discussed in Section 3.2.5.

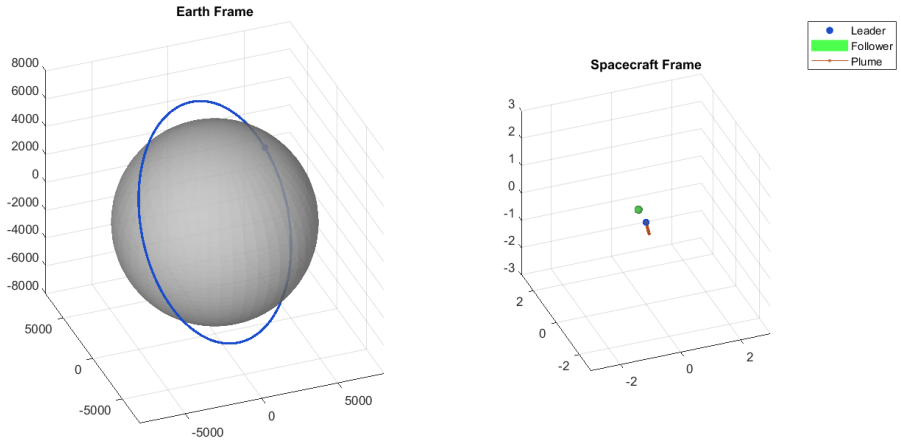

Fig. 40: Sample Trajectory from Plume Matlab Model

5. Experimental Facilities

5.1. Overview

In order to carry out the experiments we propose in this work, a variety of equipment ranging from vacuum chambers and ion sources (to carry out the experiment) to analysis equipment such as scanning electron microscopes and optical profilometers to analyze the topography and characteristics of the exposed samples was used. This chapter will outline the details of the equipment used to carry out the experiments and its evaluation.

5.2. Vacuum Chamber

The plume impingement experiments have to be carried out in a vacuum-like environment for the ion beam to propagate. The vacuum chamber used in this experiment is a custom-designed pressure vessel from Kurt J. Lesker Company. This chamber has an internal volume of approximately 128 L with an 46.7 cm diameter and 74.7 cm interior length. The chamber is capable of internal pressures of $1x10^{-8}$ torr, although these pressures were not required for the experiments contained in this work. Internal pressure is monitored through a combination of thermocouples, a capacitance manometer, and an ion gauge for pressures below 1 mTorr. The vacuum chamber also utilizes a magnetically-levitated turbopump with

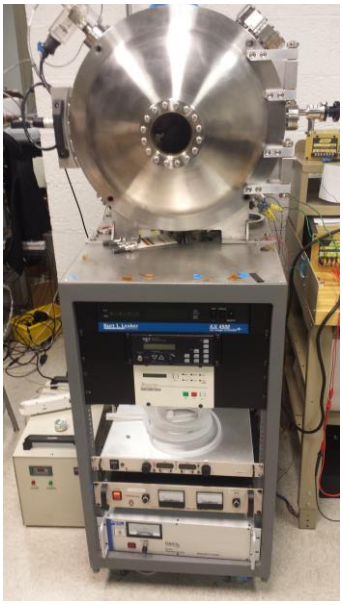

Fig. 41: Experimental Facility with Power Supplies and Recirculating Chiller

butterfly valve that allows us to accurately control the internal pressure inside the chamber for a variety of testing conditions. A complete listing of the equipment attached to the chamber is provided below in Table 1.

Table 1: Vacuum Chamber Components

Pumps	
Roughing	Pfeiffer Duo 10 M Rotary Vane Pump
Turbomolecular	STP-301 Turbomolecular Pump
Controllers	
Multi-Gauge	KJL-4500 Ionization Gauge Controller
Throttle Valve	MKS 651C Pressure Controller
Turbomolecular	STP-301/451 Turbopump Controller
Sensors	
Thermocouples	KJL-6000 Thermocouple Tubes
Manometer	MKS 626B Capacitance Manometer
Ionization Gauge	Bayard-Alpert Ionization Gauge

5.3. Ion Sources

5.3.1. SPPL-1 Ion Source

In order to carry out our earlier experiments with plume impingement, a lab-grade ion source was created in order to observe the elemental composition changes and topographical changes induced by argon ion plume impingement. This source was capable of changing the beam energy up to 300 eV as well as varying the beam current output to the target[60]. A detailed description of this source is available in Appendix E.

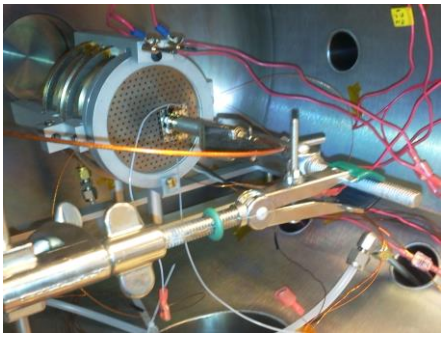

Fig. 42: SPPL-1

5.3.2. Tectra GenII Ion Source

Due to the variety of experiments that are required for this study, a decision was made after preliminary testing to move to the Tectra GenII Ion Source. This ion source provides expanded capabilities from the SPPL-1, such as a variable beam energy up to 2kV and a beam current of up to 20 mA at standard working distance. The sputter gun also provides beam neutralization through the form of a biased tungsten filament neutralizer.

Fig. 43: Tectra GenII Ion Source (image provided from www.tectra.de/plasma-source)

Unlike the SPPL-1, which was made as a lab-model DC ion engine, this ion source uses electron cyclotron resonance (ECR) to ionize neutral particles using radio frequency (RF) waves. This method of ionization allows for a non-contact method of ionization, as the DC method requires a direct exposure to both an anode and cathode for the discharge required to make the plasma. In addition, the GenII is equipped with an all-ceramic plasma cup, which allows for the ionization of reactive gases (such as oxygen). For this source, the ionization waves are provided by a magnetron source that is directly attached to the rear of the ion source.

The GenII ion source can use a variety of gases. For the purposes of preliminary testing, Argon gas was used to validate the erosion modelling referenced in Chapter 3. The bulk of the experiments (as well as the major contributions from this work) were performed with research-grade xenon, as this is most representative of the propellants used for EP systems. The gas is fed from a tank-mounted regulator through a variable leak valve mounted directly to the GenII to moderate gas flow into the vacuum chamber. This allows for fine control of particle fluence for the experiment. It is important to note that due to the use of heavy gases (i.e.: argon and xenon), frequent oxygen/air plasma cleaning is needed to reduce/eliminate buildup of sputtered molybdenum from the grids, as this will reduce the output of the source and ultimately cause isolation issues between the grids. Heavy buildup can be removed using a diamond grinding wheel.

The GenII is divided into four main components: the magnetron, the anode grid, the extractor grid, and the neutralizer filament. As mentioned above, the magnetron is used to provide the ionization wave to the gas fed into the discharge chamber. The anode and extractor grids (made of molybdenum) make up the ion optics of the device, which both set the ion beam energy (anode) and extract the ions from the discharge chamber (extractor). In addition to the potential electrical isolation issues mentioned above, the anode must also be properly insulated from the gas inlet via insulation wool. If the wool is compromised, an arc can form between the anode and the gas inlet due to the conduction path provided by the plasma if the anode potential is high enough. The neutralizer is made of a tungsten filament that allows for the thermionic emission of electrons to make the area around the beam exit charge-neutral. The list of power supplies and their matching components are listed in Table 2.

Table 2: GenII Power Supplies

Component	Power Supply	Capabilities
Anode	Glassman FJ2P60	2000 V, 60 mA
Extractor	Glassman EH5N20L	-5000 V, 20 mA
Neutralizer	Acopian A015HX1000M	15 V, 10 A
Magnetron	Tectra Magnetron	4000 V, 60 mA

5.4. Diagnostic Equipment

5.4.1. Retarding Potential Analyzer (RPA)

In order to analyze the beam conditions, we are employing the use of an RPA. This instrument allows us to observe the beam current and energy of the ion source during normal operation. From these readings, we can derive the beam flux at different spots of the beam as well as get an overall picture of what the beam geometry and current will look like as a function of both axial and radial propagation.

Fig. 44: Kimball Physics FC-71 A Faraday Cup w/energy analyzing grids [50]

To this end, we are employing the Kimball Physics FC-71A[61] Faraday cup with attachable energy analyzing grids to convert it to an RPA. An RPA usually utilizes four grids: 1) a floating grid

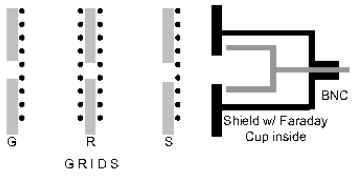

Fig. 45: FC-71 A Grid Layout [50]

that floats to the potential of the beam being analyzed; 2) a suppression grid that significantly reduces/eliminates any oppositely-charged particles that are not desired in the measurement; 3) allows only particles above the voltage set by the grid into the collection chamber; and 4) a secondary suppression grid that keeps any background particles of opposing charge scattered by the particle impact on the collector to be repelled back into the collector to reduce the effect on the current collection of the collector. However, the FC-71A is composed of three grids: a floating grid, discriminator grid, and a suppression grid for backscattered particles. With the grid set-up as specified, it is really meant to analyze one type of particle beam at a time instead of a beam composed of both ions and electrons. However, with the small amount of background electrons in the beam, the effect on the measured current is negligible.

However, with prolonged use of the RPA, there is a need to regularly replace the grids. Exposure to the xenon beam at the energies and durations required for the experiments will erode the tungsten mesh from the grids. Eroded mesh from the beam will result in inaccurate beam current readings which will result in high standard deviations in the experimental readings and sputter yields.

5.4.2. Veeco Wyko NT1100 Optical Profilometer

In order to measure the erosion experienced by each sample, an optical profilometer was employed to directly examine the 2-D surface profile of the sample in specific areas. This instrument, provided by the University of Maryland MEMS Sensors and Actuators Lab (MSAL), uses white-light interferometry in order to determine the depth of the surface under the scan area. These scans can be performed in either Vertical Scanning Interferometry (VSI) or Pressure Scanning Interferometry (PSI) mode[62]. VSI

mode uses two different wavelengths of light to create destructive interference in the viewing area, which allows the instrument to examine the topography of the sample. PSI mode uses one wavelength of light, which is more accurate, and is meant for erosion depths up to 150 nm. Although PSI mode is meant for higher resolution scans, it is also meant for smoother samples with very little variation such as optical glass or super-polished metals[63]. This setting is also more sensitive to vibration and other environmental factors which can interfere with the scanning process. With this and the potential roughness of the erosion area in mind, all sample data from this device was acquired using the VSI method of profilometry.

When a scan is performed, the data is converted into a contour image with heat-map coloring corresponding to the height ranges observed in the scan area. From this, 2-D profiles can be extracted from the contour image, where average heights of selected parts of the profile can be calculated. The instrument, which at its lowest magnification has a viewing area of 1.35 x 0.95 mm, can scan a sample profile down to the precision of ±1Å.

While the precision of the instrument is amazing, due to the width of the sample cross-section, the lowest resolution scan is the only possible way to determine the depth throughout the entire area of interest (AOI). This scan uses the 5x magnification of the instrument with the viewing area listed above. However, due to environmental conditions in the scan area (i.e.: vibration, gusts of air from vents, etc.), the scans may have a variance up to ± 30 nm as long as the scan is well-focused. The other issue is due to the scanning method of the device; the depth of the sample must exceed 150 nm in these conditions to have a reliable scan.

This method of profilometry, as implied, is non-invasive. As a result, the samples can be preserved for future experiments or scans should they be necessary. Optical profilometry offers higher resolution scans than their contact profilometer counterparts, but their main disadvantage lies within relying on the light reflection from the samples; if the sample is too reflective, the scans can be inaccurate. In addition, if the sample has black discolorations from burns, it will also affect the scan. However, with the samples examined for this work, no issues have occurred. Sample output from the device can be seen in Fig. 46.

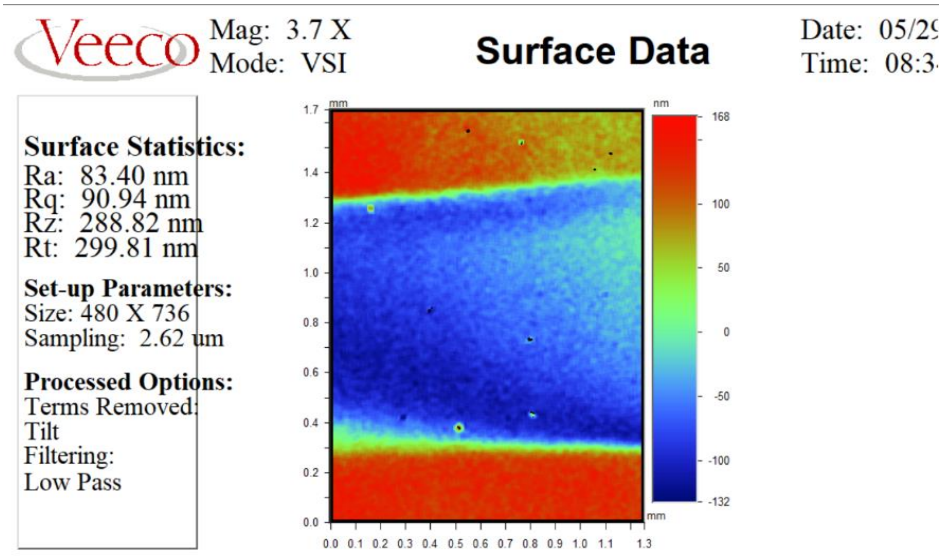

Fig. 46: Sample output from NT1100 Optical Profilometer

5.4.3. Veeco Wyko NT3300 Optical Profilometer

Throughout this project, data was also collected using an NT3300 Optical Profilometer provided by the University of Maryland FabLab (part of the Maryland

Nanocenter). This optical profilometer is a slightly newer version of the NT1100 with similar resolution limits. This profilometer was kept in a clean-room environment and as such, most measurements were relatively unaffected by the surrounding environment, resulting in slightly improved scans of the samples. Also, as with the NT1100, the data acquired from the NT3300 was taken using the VSI method of profilometry.

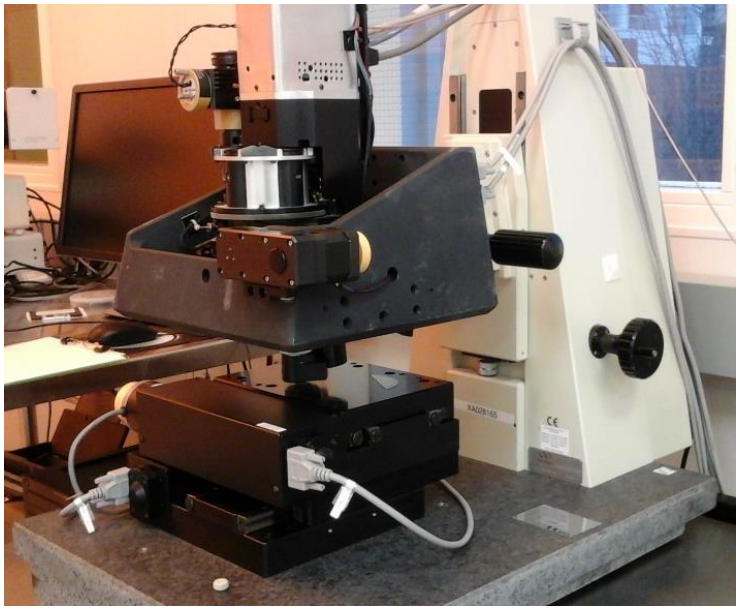

Fig. 47: Veeco NT3300 Optical Profilometer

5.4.4. Scanning Electron Microscope (SEM) with Electron Diffraction Spectrometer (EDS)

Throughout the experiment, several SEM scans were taken of samples that were exposed to the ion beam. These images were taken to assess the topography of the exposed areas as well as the elemental composition of the target areas. This was performed using a Hitachi SU-70 SEM with an attached Brüker EDS device, which can give target area compositions by using x-ray excitation. Data from these measurements has appeared in prior published work from the author[60].

6. Experimental Procedures

6.1. Overview

This section will outline the steps of performing an erosion experiment along with some of the basic operating guidelines for the experiment from the prep of the experiment to the analyses performed on the data collected from the experiment. This section will provide a detailed look into the profilometry analysis as well as the error analysis for each data point reported.

6.2. Erosion Testing Procedure

To gather the sputter yield data for each material, the sample has to be directly exposed to a representative plasma beam within a vacuum chamber. These samples have to be reasonably flat in order to ensure that whatever effect the plasma sputter has on the sample, it is not significantly affected by variable topography. From there, these samples will be placed in the chamber and erosion will take place while current readings of the samples will take place *in situ*. This data will then be related to the erosion depth observed from the profilometer and, through analyzing the depth using the equations from Section 3.2.3, a sputter yield for a specific sample can be obtained.

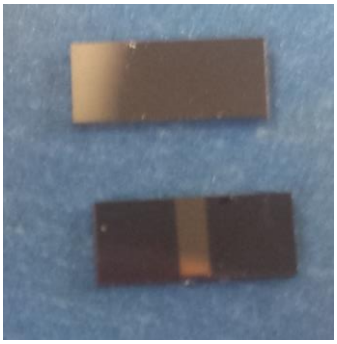

Fig. 49: Photo of uneroded Al sample (above) and eroded Al sample (below)

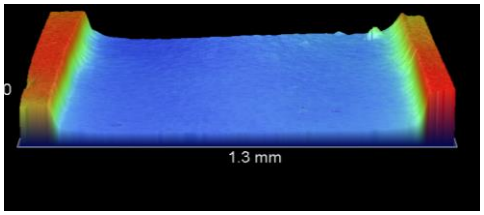

Fig. 48: 3-D Representation of Sample Scan from Veeco NT3300

The material samples, fabricated within the

University of Maryland FabLab, were created by coating a 500 μm thick silicon wafer with the maximum applicable layer possible for that specific material on the sample. The samples have the following thicknesses: a 1 μm thick coating for aluminum; a 500 nm layer of Magnesium Fluoride; a 600 nm layer of ITO. These layers were applied through atom layer deposition on the silicon wafers and then split into multiple 3 x 7 mm samples for use on the sample holder mounted to the RPA. The use of the silicon wafer is two-fold: 1) the coating of the silicon wafer will provide an ultra-flat surface for the material to lay on, which lowers the potential errors from profilometry analysis; 2) the samples can be cut to exact measurements using a computerized diamond rotary saw to slice the coated wafers. It is also important to note that the exposed area is 3 mm^2. This allows for the scans from the Veeco profilometer to look at the entirety of the exposed area as well as the edges of the unexposed borders. The representative scan is pictured in Fig. 49.

The experiment was performed by doing the following: 1) The sample is mounted into the RPA sample holder and then placed in front of the ion source in a manner similar to Fig. 42; 2) the vacuum chamber is then pumped down to a standard operating pressure of around 0.2-0.4 mTorr, which is the pressure at which the mean free path within the chamber was more than sufficient for the beam to propagate properly; 3) the plasma source is then ignited and the desired beam conditions for the experiment are set; 4) once the beam begins propagating, the picoammeter begins recording the beam current from the RPA for the duration of the experiment. The picoammeter is usually set to look at a total number of loops, data points per loop, as well as the total number of milliseconds between each loop. Although the total number of loops is manually set based on the estimated time for the experiment, the other parameters are kept at 20 data points per loop

every 15000 milliseconds (15 seconds). This provides an optimum number of data points to average over as well as preventing the device from having one loop spill into another, causing recording issues. Once the experiment is over, the sample is then removed after a small cooling period and placed inside the sample case to await scans on the Veeco profilometer.

After each erosion experiment, the current data is then post-processed to find the average erosion current for the experiment. The data from the picoammeter is output through a LabView text file (.lvm), which can be read through Microsoft Excel. This file contains the averaged current for every loop recorded by the device. There is also a second output .lvm that reports every single beam current recording per loop, just in case the first output file has any suspect reported averages. The reported averages are then imported into an Excel workbook to look at each loop's recorded current average. Here, we can then derive the actual beam current that hit the exposed surface area of the sample, based on the expected distance away from the collector (for angled samples, as they have a stand that is a significant distance away from the RPA collection orifice) as well as the difference ratio between the collector and the exposed surface area for the samples. This can be performed via simple manipulation of Equation 4-21. Once this is known for every loop, the averaged current can be reported for the duration of the experiment as well as the standard deviation of the reported current loops. These are reported as the standard deviation of the population of data and are also only reported to 1-σ.

Due to relatively high vacuum pressure for these sputter experiments, there is the potential for impurities to be deposited on the surface. For more on this subject, please refer to Appendix D.

6.3. Profilometry Analysis Procedure and Sputter Yield Calculation

After a sufficient time has passed, the samples are then taken to the University of Maryland FabLab for scanning on the Veeco profilometer. Although this environment is a clean room environment, due to the shallow depths expected (<500 nm), multiple scans are taken within the same scan region of the sample (~10-12) to allow for the variation between scans (from either instrument noise or unintended environmental factors such as sudden vibration or changes in pressure). This lengthy process is repeated for each sample in the entirety of this work to ensure high-quality data. After these scans are taken, they are then post-processed through the Veeco proprietary software, Vision32, as seen in Fig. 46.

Vision32 can analyze the average depth of the entire sample from the viewing window of the scans as well as provide other possible metrics of interest, such as surface roughness values, etc. However, for the purposes of this experimental effort, we're choosing to look purely at the average depth of the sample. In order to report this, we can take the sample data and divide it into five individual sections, as seen in Fig. 50. Sections 1-4 represent the unexposed sample area visible in the scan

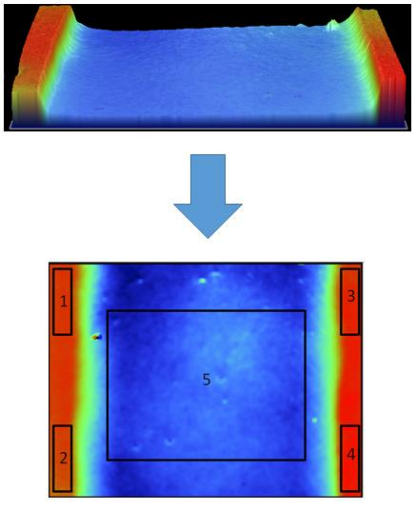

Fig. 50: Sample Analysis Diagram

window; Section 5 represents the exposed and eroded area of the sample. From here, a low-pass filter is applied to the scan data to eliminate noise from the sample, which would represent gradients in the data which represent less than 5% difference of the points next to that respective point. This process leaves a smoother profile for analysis.

Each of these sections has their respective average depths recorded within the section boundaries. From here, the average of the unexposed area of the sample is found by looking at the average height of each side (with the left and right being represented by Sections 1-2 and 3-4, respectively) and then averaged. With the average height of the unexposed area found, we now subtract the average depth of Section 5 to get the overall depth of the sample caused by the beam exposure. This process is repeated for each sample scan and each result is then used to find the average depth for that sample. The standard deviation of these measurements are reported as the standard deviation of the population and are also reported to 1-σ.

The results of both the profilometry scans and the current data are then tabulated together to find the sputter yield for each sample, as per the methods presented in Section 3.2.3. From these, the reported sputter yields are the average of all the accepted samples from the effort, with their standard error of the mean reported as 2-σ.

7. Project Results: Aluminum

7.1. Overview

One of the potential side effects of ion plume erosion is the exposure of the spacecraft's vulnerable electronic components. These components are usually shielded by very thin layers of aluminized mylar (such as BoPET), a material that combines thin sheets of mylar and very thin-film aluminum, in order to protect the vital components from thermal stress and micrometeorite impact. Multiple layers of this material are usually used, as some aluminum layers of the material have been known to be at least 4.5 μm thick[64]. Given the fact that for any spacecraft, there could be an aluminum layer that could only be hundreds of microns thick, it stands to reason that the electronics could be at a reasonable risk for erosion damage from the ion plume.

As aluminum is a standard aerospace structure, it is a highly viable material to perform erosion testing on. However, with the exhaustive testing of aluminum already done[13] with xenon ion plumes, this effort can use these experiments to not only validate the testing methods for gathering the sputter yield data, but the data can also be expanded to look at higher energies that would encompass the energy regime of high specific impulse electric thrusters. In the section below, we will present the work

Table 3: Aluminum Experimental Test Matrix

Test Conditions, 1200 eV	Test Conditions, 1500 eV
1200 eV, 0°	1500 eV, 0°
1200 eV, 30°	1500 eV, 30°
1200 eV, 0°	1500 eV, 60°

performed on our aluminum samples from both the Tectra ion source, as well as earlier work from our SPPL-1 source. Table 3 contains the experimental test conditions for all the samples tested in the remainder of this chapter.

7.2. Experimental Results

7.2.1. 1200 eV Experiments

Although there has been published data at this energy level from Tartz[37], since these were the first experiments performed with this method, the prior datasets published were used as calibration data for the method used throughout this work. The following data represent the individual experiments that make up the 1200 eV data points, as represented in Table 4.

Table 4: 1200 eV Sputter Data

Sample #	Incidence Angle (º)	Average Ion Rate (ions/sec)	Ion Rate Std. Dev (%)	Duration (min)	Depth (µm)	Sputter Yield (atoms/ion)
6	0	1.31E13	6.72	15	1.24E-1	1.896
7	0	1.67E13	5.11	15	1.63E-1	1.959
9	0	1.08E13	5.75	40	2.87E-1	2.002
2	30	3.96E13	9.57	10	2.34E-1	1.784
5	30	2.30E13	4.30	8	2.18E-1	3.582
6	30	1.54E13	2.46	15	1.82E-1	2.377
7	30	2.71E13	3.88	15	1.23E-1	0.911
1	60	1.47E13	0.98	15	5.06E-1	6.898
2	60	1.01E13	1.54	15	3.71E-1	7.396

With the exception of the 30˚ data points, most of the samples show small variations within the measurement sets themselves. It is also noteworthy that the sputter yields for the normal incidence data show very reasonable agreement with previously publish data.

7.2.2. 1500 eV Experiments

The following data represents a newly experimentally derived dataset for 1500 eV for this specific sputter interaction. This data was taken to expand the wealth of sputter data to energies that would represent a specific impulse of 5000 seconds for an electrostatic thruster. With the exception of the spread of the data for the 60˚ case, most of the data shows reasonable agreement and variation for these types of experiments.

Table 5: 1500 eV Sputter Data

Sample #	**Incidence Angle (º)**	**Average Ion Rate (ions/sec)**	**Ion Rate Std. Dev (%)**	**Duration (min)**	**Depth (µm)**	**Sputter Yield (atoms/ion)**
2	0	1.59E13	13.70	10	1.55E-1	2.933
4	0	2.31E13	2.23	20	2.56E-1	1.670
13	0	6.37E12	28.73	35	1.59E-1	2.147
7	30	1.38E13	14.86	20	2.23E-1	2.435
8	30	1.07E13	18.19	20	2.08E-1	2.924
13	30	2.70E13	6.38	15	2.85E-1	1.753
1	60	9.66E12	3.73	15	3.01E-1	6.254
2	60	1.14E13	1.75	15	4.57E-1	8.093
3	60	1.18E13	1.81	15	5.71E-1	9.745

7.2.3. Sputter Yield Data

The datasets from the previous sections were averaged to produce the datasets presented in this section. This data represents the extent of the experimental data taken from the aluminum experiments and was then used to determine the theoretical models discussed in later sections. All error bars are representative of 2-σ.

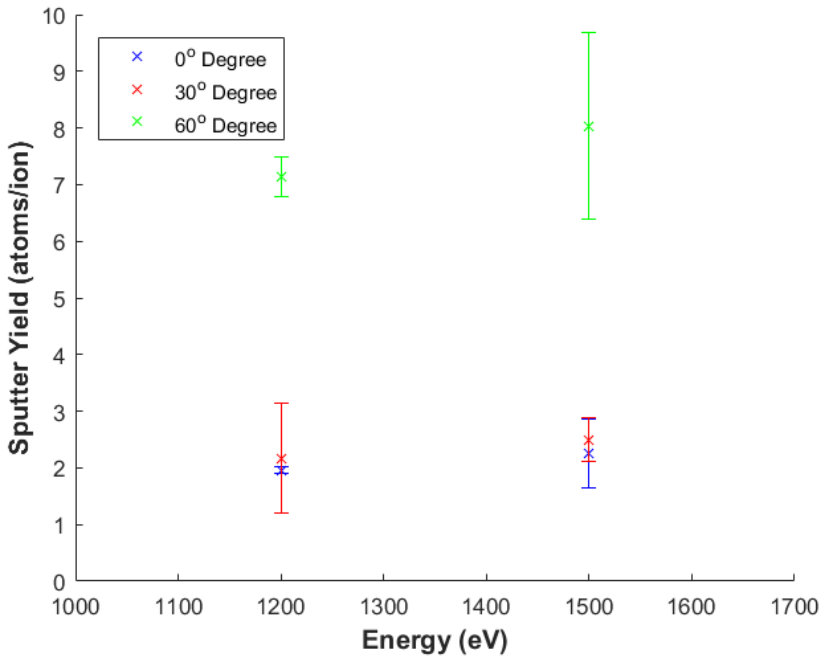

Fig. 51: Aluminum Experimental Sputter Yield Data

The normal incidence sputter yield values for 1200 eV are in good agreement with both prior established experimental data from Tartz and the established Eckstein fits. The 30˚ and 60˚ incidence data for 1200 eV show agreement with Eckstein fits and Tartz data. The 1500 eV data points for all incidence angles show an expected increase that is consistent with the increase in incidence energy. Among each incidence angle each data

point increases linearly with energy, which is an expected trend (this will be more evident with the AR sputter data shown in later chapters).

7.3. Sputter Yield Theoretical Fits

7.3.1. Bohdansky Normal Incidence Fit

With the normal incidence data, we can now derive the Bohdansky parameters for the normal incidence fit for all energies. Using the equations from Section 3.2.2, we are able to perform a parametric curve fit to find the appropriate parameters for the best normal incidence fit to the data. Utilizing the curve fitting tool from Matlab, we are able to find these parameters for the experimental data.

Table 6: Al Sputter Model Parameters

Parameter	Quantity
Q	20.67
E_{th}	34.85 eV
f_{sig}	1.8
R	0.4048 nm

Based on the best-fit Bohdansky curve, the parameters chosen were, in fact, close to the Tartz parameters, which was an expected outcome. There are only slight changes to these parameter based on this effort's experimental data points, especially the new 1500 eV data point. The parameters Q and Eth from this effort were used to map the Tartz data points as well and they show excellent agreement with the established experimental data, as seen below in Fig. 52.

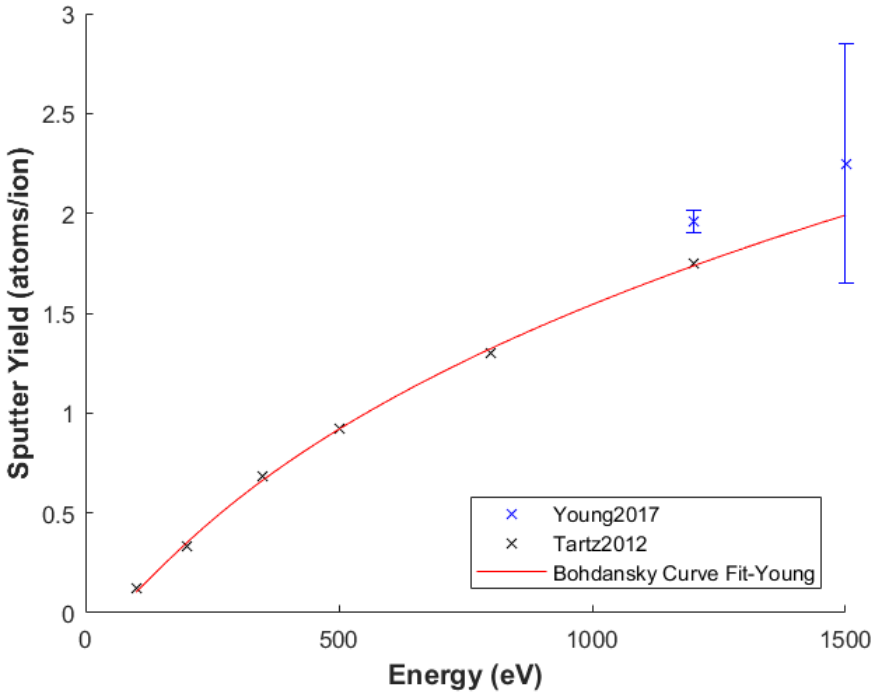

Fig. 52: Aluminum Bohdansky Fit

7.3.2. Yamamura Angular Incidence Fit

The angular fits for Aluminum are relatively straight-forward, since the only remaining parameter that is of importance is the f_{sig} parameter available from the Yamamura text[57]. The angular fit shows reasonable agreement with the 30˚ and 60˚ data, although the latter shows an almost 20% disagreement with the theoretical curve. The results of the fit are shown in Fig. 53.

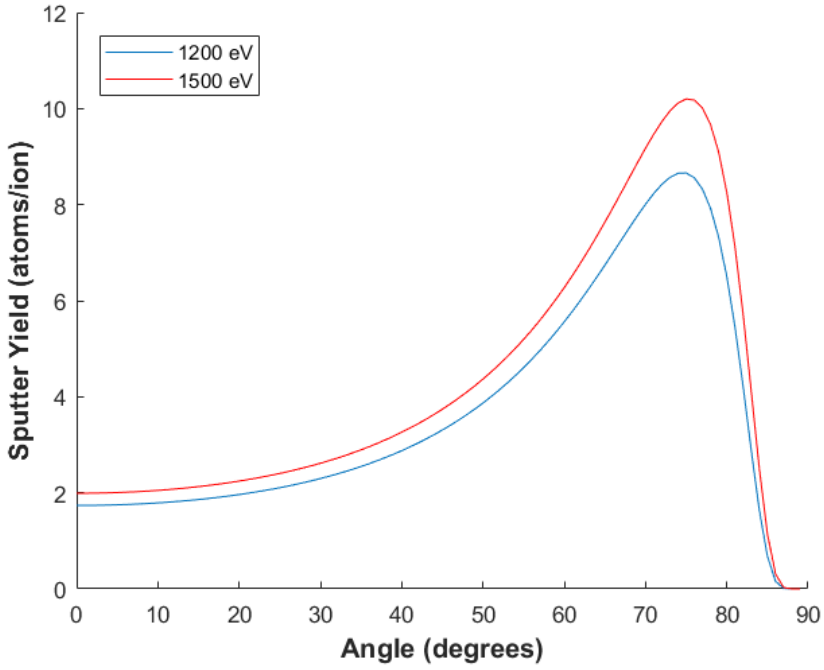

Fig. 53: Aluminum Angular Incidence Fit

7.4. Discussion

As mentioned in the previous sections, the experimental data from this effort shows reasonable agreement with previously established data, although not without some interesting deviations, especially within the angular incidence fits.

As shown in Fig. 52, the normal incidence data from this effort is within reasonable agreement with the Bohdansky model and a slightly higher sputter yield from the Tartz data for 1200 eV. This may be accounted for with the method by which the data is gathered to determine the sputter yield, as mentioned in Section 6.3. Likewise, the 1500 eV data follows with the Bohdansky fit set by the trend line also with reasonable

agreement. Also, as not entirely unexpected, the Bohdansky fit also under-predicted the experimental data by ~10%, which is well within acceptable published tolerances of fits involving noble gas sputtering[12].

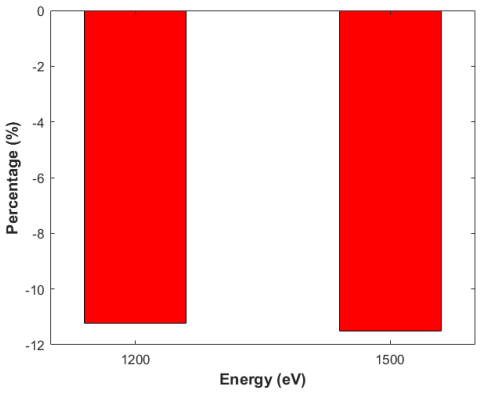

Fig. 54: Al Experimental-Theoretical Difference

For the Yamamura fits of the aluminum data, the data tends to fit very well with the 30° incidence data and the 1200 eV data at this incidence is also comparable with Tartz[37]. However, while not entirely unexpected, there is a reasonable variance with the 60° incidence data, showing ~20% variance from the model. This can also be expected due to the noble gas sputtering effect for these type of modeling techniques.

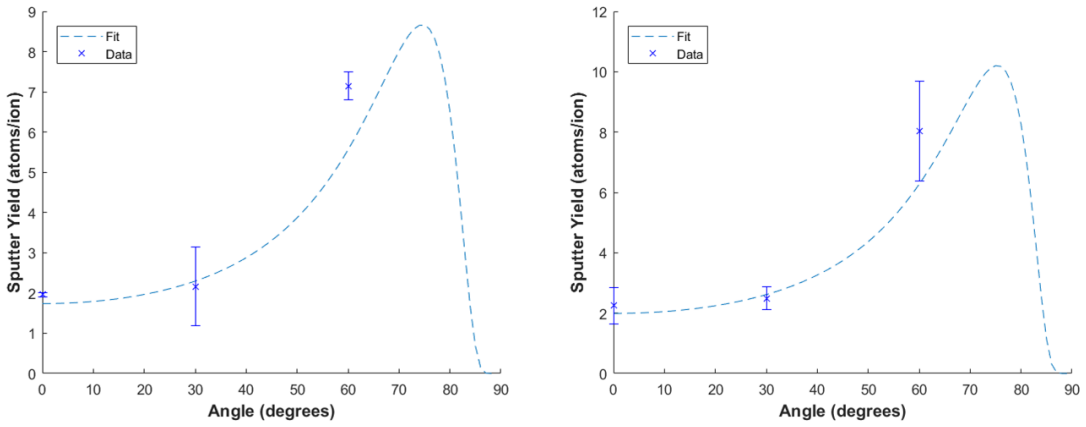

Fig. 55: Aluminum Sputter Yield Comparisons between Yamamura fit and experimental results, 1200 eV (left) and 1500 eV (right)

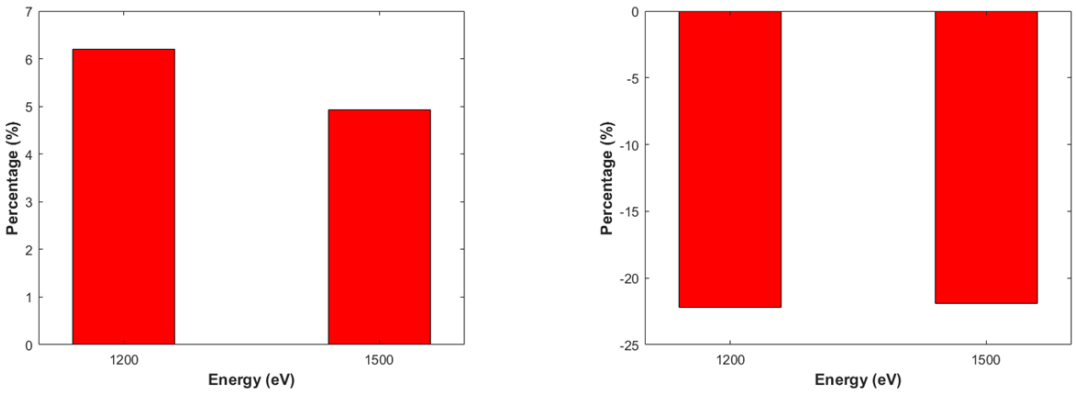

Fig. 56: Aluminum Comparisons from fit to experimental data, 30° (left) and 60° (right)

Although the vacuum of space is a relatively cold environment, heating of the material is also a possible outcome for damage based on the effects of the ion beam. As such, melting the samples in the target area was a concern throughout the aluminum experiments. During preliminary experiments with aluminum, the sputter yields that were reported previously were of a significantly higher sputter yield than expected, especially at higher incidence angles.

It was previously thought that this may have been due to measurement error, but upon further inspection, the material exhibited evidence of material flowing into the exposed area as well as burns on part of the sample. Although the melting point of Aluminum is 933 K, this will change based on the ambient pressure of the material's environment, according to the Clausius-Clapeyron relation, as shown in Equation 7-1[65]. Based on the vacuum chamber's operating pressure during the experiments, the aluminum would have a melting temperature of 644 K, a significant drop from the standard melting point in 1 atm. For the purposes of our experiments, this would then limit the amount of current that can impinge on the sample during an experiment in order to prevent melting.

$$\ln\left(\frac{P_2}{P_1}\right) = \frac{-\Delta H_{vap}}{R}\left(\frac{1}{T_2} - \frac{1}{T_1}\right) \quad (7\text{-}1)$$

Although the experimental conditions had to be adjusted for this experimental effort, these types of considerations will not be taken into account on orbit. For close maneuvers, the particle flux could be as high as 10^{19} #/m^2-s, which were the particle flux values at which some melting was reported on preliminary samples during experiments. Flux values of individual maneuvers will be reported in Chapter 10.

8. Project Results: Magnesium Fluoride

8.1. Overview

Magnesium Fluoride, as mentioned in earlier chapters, is an anti-reflective (AR) coating for space-rated solar panels. This material is very important for focusing certain wavelengths of light to increase performance on the solar cells. If the AR coating is eroded, the efficiency of the solar cells will be reduced by 3-5% because of changes in the transmission properties of the coating[52]. If the coating is completely eroded, the maximum amount of efficiency loss will be expected. As most space-rated panels are only 20-25% efficient, this is a significant drop in power just from erosion of the AR coating alone. This chapter will look into the results from the MgF_2 erosion studies as well as the representative theoretical curves. The test matrix of these erosion experiments is listed in Table 7. Individual sputter data is contained in Appendix A.1. Magnesium Fluoride Samples.

Table 7: Anti-Reflective Coating Experimental Test Matrix

500 eV Test Conditions	750 eV Test Conditions	1000 eV Test Conditions	1250 eV Test Conditions	1500 eV Test Conditions
500 eV, 0˚	750 eV, 0˚	1000 eV, 0˚	1250 eV, 0˚	1500 eV, 0˚
500 eV, 30˚	750 eV, 30˚	1000 eV, 30˚	1250 eV, 30˚	1500 eV, 30˚
500 eV, 60˚	750 eV, 60˚	1000 eV, 60˚	1250 eV, 60˚	1500 eV, 60˚

8.2. Experimental Results

The sputter yields, like the results from Section 7.2.3, show linear trending within their respective incidence angles and show reasonable agreement with that trending. The data also shows expected increases based on Yamamura-style trending. Further remarks about the data will be presented in their respective sections. All error bars are reported to 2-σ.

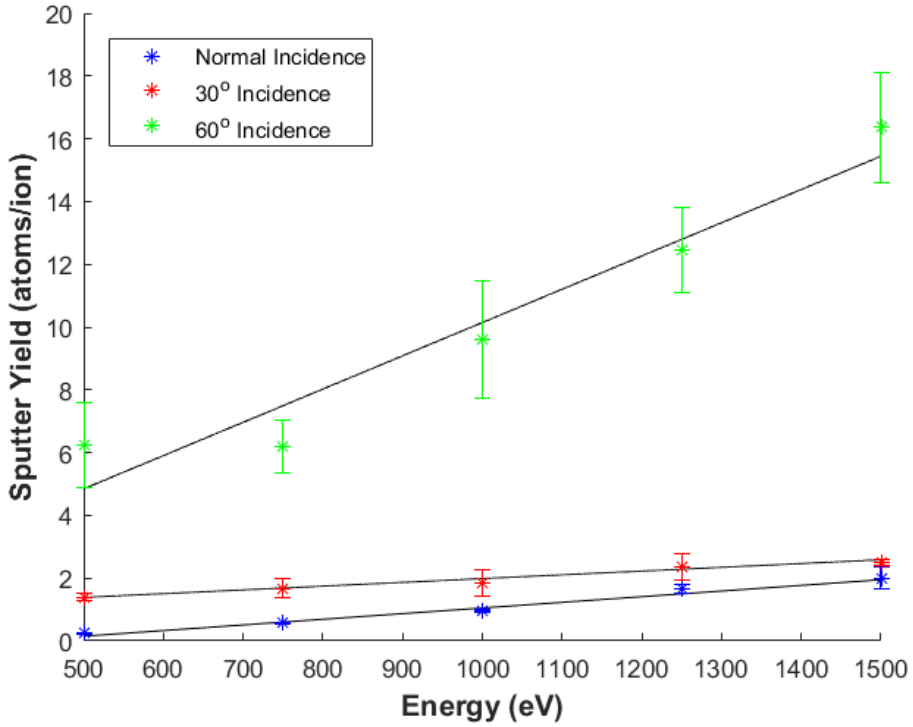

Fig. 57: Xe→MgF_2 Sputter Data

8.2.1. MgF_2 Normal Incidence Data and Fit

With the analysis methods used for determining the sputter yield, the sputter yields show reasonable agreement with each other. However, it is noticeable that the lower energy runs for the MgF_2 samples the standard deviation of the sputter yield are

slightly higher than the energies above 1000 eV. This is due to a scanning issue based on the depths of the sample, as mentioned in Section 5.4.2. The normal incidence data also shows reasonable agreement, trend-wise, with the prior experimental results by Yalin.

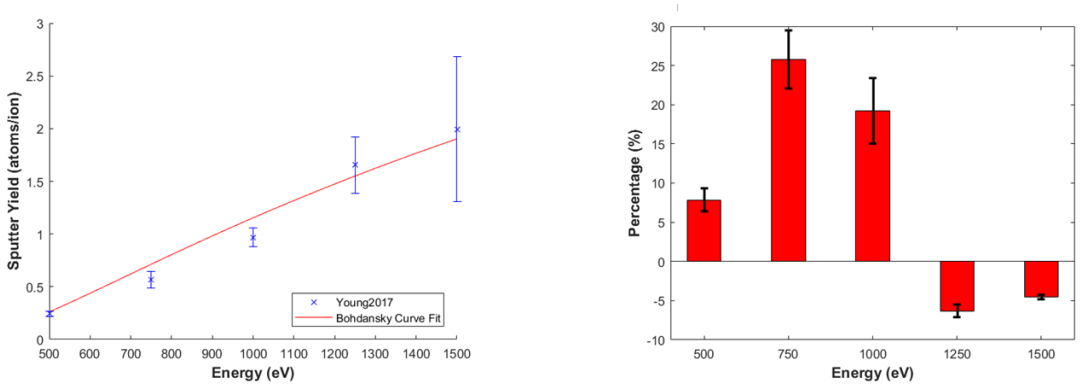

Fig. 58: MgF2 Bohdansky Fit (left) and Percentage Difference from Bohdansky Fit (right)

The Bohdansky fit for this data also shows reasonable agreement with the experimental data, with at least 75% agreement among all energies tested. This is within the 30% limit set out for noble gas sputter models. Consequentially, this fit also shows good agreement with the previous Yalin data at the lower incidence energies from that effort. The fit parameters are listed in Table 8. The strength of the fit is listed in Table 9.

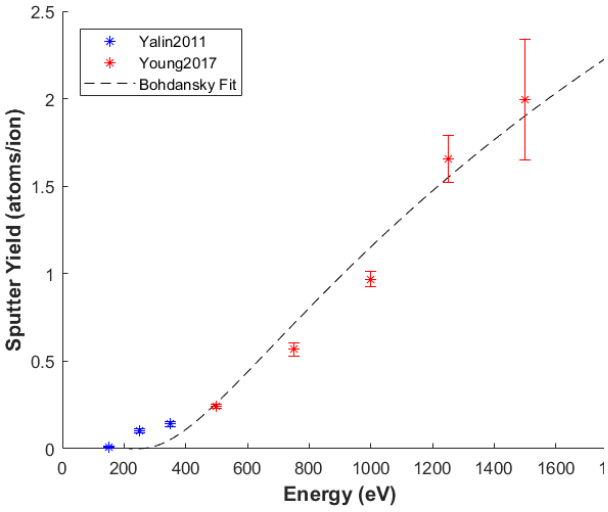

Fig. 59: MgF2 Normal Incidence Fit with combined Sputter Data

Table 8: Magnesium Fluoride Fit Parameters

Q	E_{th}	Z_{eff}	f_{sig}	R
22.81	231.1 eV	10.4051	1.53	0.306 nm

8.2.2. MgF_2 Angular Incidence Data and Fit

As with the normal incidence data, the angular data shows linear trending within each respective incidence angle and also shows reasonable Yamamura-like trending across incidence energies. For the most part, the error bars show reasonable agreement with ~6% across most data points with the exception of 750 eV and 1250 eV at 30° incidence and 1250 eV and 1500 eV at 60° incidence. For the 30° incidence data points, these measurements may have been affected by burns on the surface of the samples or possibly poor scan quality. For the 60° incidence data, they mildly exceed the model uncertainty by 1% and 10%, respectively, possibly due to fitting techniques, which will be discussed below. However, the data for the most part are in reasonable agreement within their respective experimental condition.

Table 9: MgF_2 Goodness Parameters

SSE	0.1094
R-Square	0.9728
Adjusted R-Square	0.9683
RMSE	0.135

As expected, the sputter yields increase with respect to both incidence energy as well as incidence angle. It is also interesting to note the significant increase in the sputter yield as the angle increases (i.e.: 500 eV's sputter yield increasing almost by a factor of 6 versus any similar change from aluminum). As shown in Fig. 57, it does decrease as the

energy increases but not to a significant degree. This may be due to the compound nature of the material or the weakness of the bonds inside this material.

Also of note are the difficulties of fitting the angular data for MgF_2 to the Yamamura curves based on the data from Fig. 57. As the accepted theory stands, the Yamamura equation is heavily dependent on a parameter known as f_{sig}, as shown in Equation 3-12. This parameter is referenced from the text published by Yamamura for an individual sputter reaction (such as Xe→ Mg, for example). In the case of the compound targets in this effort, however, these parameters have trouble encapsulating the effect of the Yamamura curves, either vastly over-estimating or underestimating the experimental data.

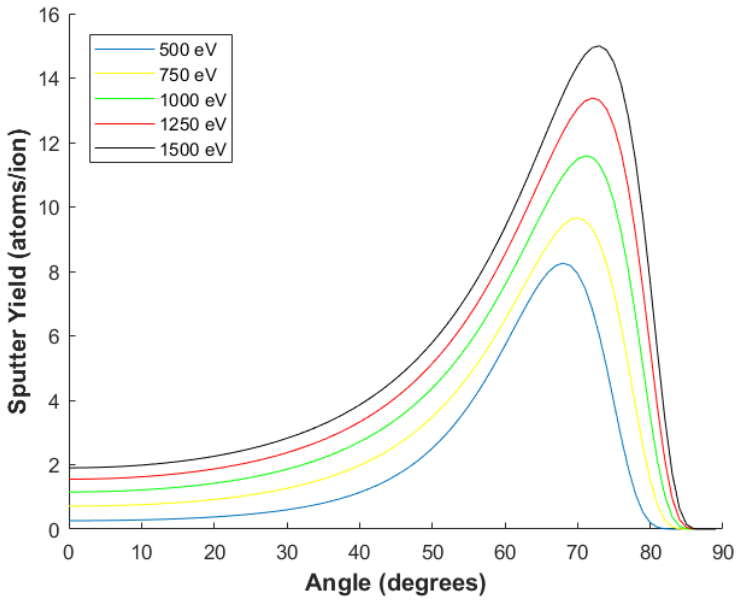

Fig. 60: MgF_2 Angular Sputter Model

To alleviate this, it is necessary to modify the Yamamura method by making f_{sig} a new parameter that has to be found versus incorrectly referencing the parameters from

Yamamura. Converting f_{sig} into a new fitting parameter, we are able to somewhat fit the angular data of MgF_2. The angular model, as shown in Fig. 60, shows reasonable agreement with experimental data, with the exceptions of 500 eV at 30° incidence and 1500 eV at 60° incidence. This may be due to the fitting method for f_{sig} in addition to the difficulty for gathering the 500 eV sputter data at 30° incidence. Further discussion of these fitting difficulties is located in Appendix B.

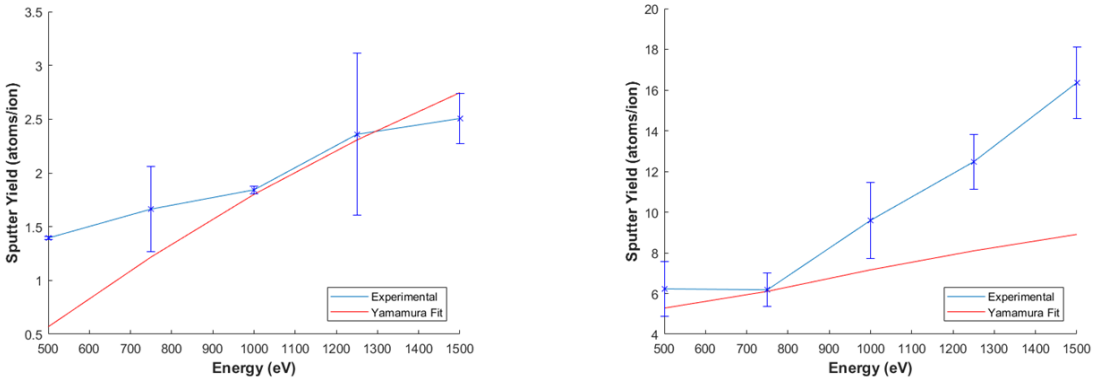

Fig. 61: MgF2 Angular Sputter Data Comparisons, 30° (left), 60° (right)

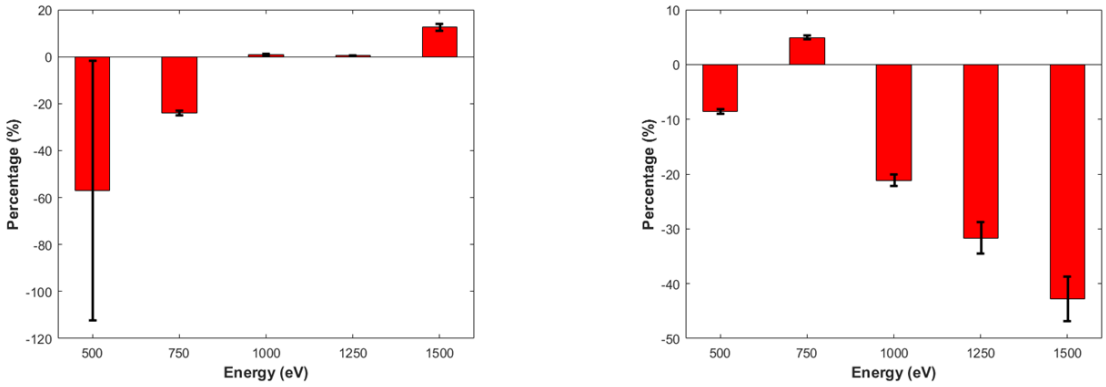

Fig. 62: MgF_2 Angular Fit Comparisons, 30° (left), 60° (right)

9. Project Results: Indium Tin Oxide (ITO)

9.1. Overview

As with Magnesium Fluoride, Indium Tin Oxide (ITO) is an anti-reflective (AR) coating that is capable of focusing certain wavelengths of light in order to augment solar cell efficiency in orbit. Like MgF_2, ITO is space-rated material for solar cell coverglass, but has no published sputter data. One of the goals of this work is to present a set of data to the engineering community in order to talk about potential material choices for space mission applications. And, as with Chapter 7 and 8, the experimental results presented in this chapter will be combined with their respective theoretical fits. The test matrix for these experiments is contained in Table 7. Individual sputter data is contained in Appendix A.2. Indium Tin Oxide Samples.

9.2. Experimental Results

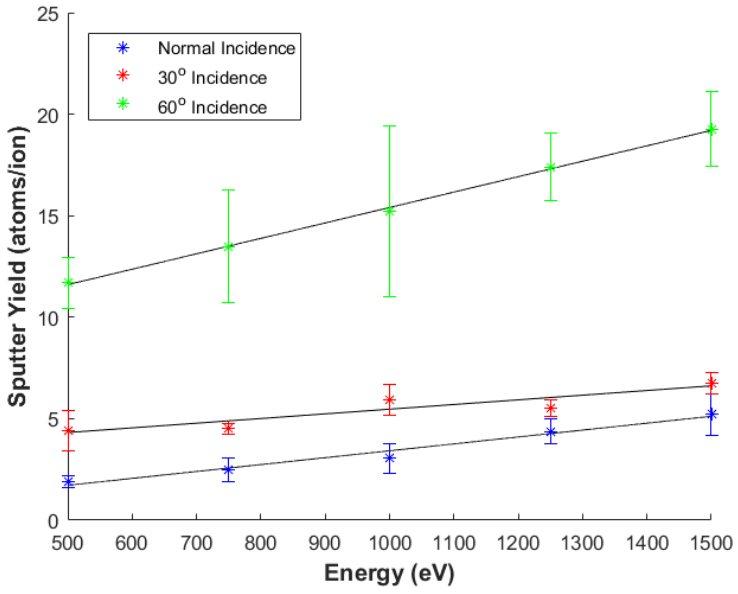

Fig. 63: Xe→ITO Sputter Data

As with the MgF_2 data, the data shows linear trending among its respective incidence angle. It also shows the appropriate sputter yield increases as the incidence angle increases. The sputter yields are considerably larger than MgF_2 for all testing points, as well. To compare, the sputter yield at 500 eV is comparable to the sputter yield at 1500 eV for a normal incidence MgF_2 sample. This means that ITO is far less resistant to sputter than MgF_2 overall. As expected, this also holds true for the other incidence angles, as well. All error bars for Fig. 63 are 2-σ.

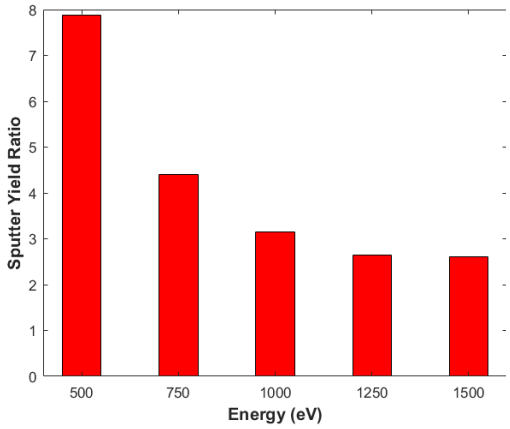

Fig. 64: Comparison of ITO and MgF_2 Sputter Yields, Normal Incidence

9.2.1. ITO Normal Incidence Data and Fit

The data shown in Fig. 63 shows excellent agreement with the linear trend, with very small errors (~20% or less at 2-σ), well within the impingement model limits as

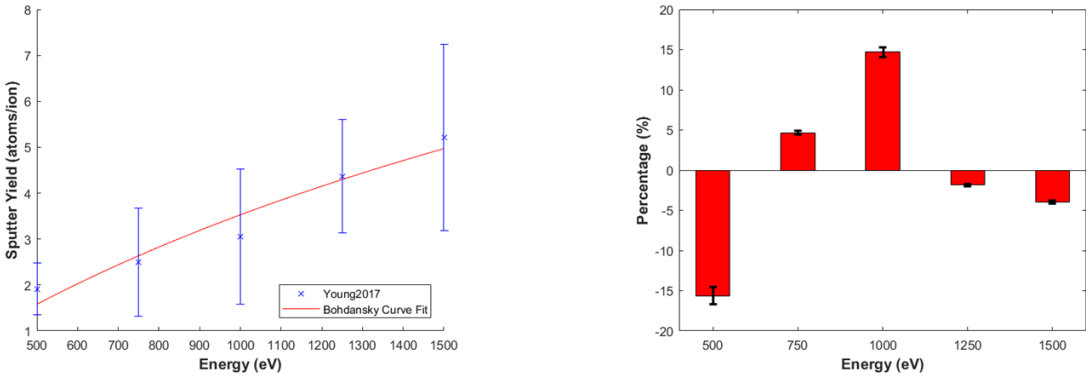

Fig. 65: ITO Bohdansky Fit (left) and Percentage Difference from Bohdansky Fit (right)

mentioned by Eckstein[12]. This agreement also extends to the Bohdansky fit of the data, as all data is within ~15% of the expected theoretical fit. The fit parameters and goodness metrics are listed in Table 10 and Table 11, respectively.

Table 10: ITO Fit Parameters

Q	E_{th}	Z_{eff}	f_{sig}	R
60.21	105.1	45.5061	1.25	1.012 nm

Table 11: ITO Goodness Parameters

SSE	R-Square	Adjusted R-Square	RMSE
0.4182	0.9433	0.9243	0.3733

In relation to the chart from Fig. 64, the vast difference in sputter yields could possibly be explained by a number of factors. The most obvious, according to the theoretical fits, have to be the difference in threshold energy. As described in Chapter 3.2.2, the threshold energy is the energy at which the sputter yield starts to become significant and increases significantly in magnitude. ITO's threshold energy is 54.5% lower than MgF_2, as shown in the theoretical fit with evidence from the normal incidence sputter data from both this work and the data from Yalin[52]. Also, the density of ITO is also considerably higher than MgF_2, which would mean there are more atoms per volume and, thus more atoms to sputter away per incident ion.

9.2.2. ITO Angular Incidence Data and Fit

The angular incidence data shows its typical trending as seen in Chapter 8.2.2, with linear trending within the respective incidence angle and the typical increases in the data as the incidence angle increases. The error bars reported all show tight agreement with the individual measurements used, with the highest set of error bars approaching ~20% for 1000 eV at 60° incidence, well within the tolerances for the sputter estimation and modeling methods as mentioned in previous sections. This data is much higher than the MgF_2 angular data, as expected due to the significant increase from the normal incidence data as mentioned in the previous section. However, the sputter yields reach as high as 19 atoms/ion, which is significantly higher than the yields experienced by MgF_2. As with the MgF_2 data, the Yamamura fit for ITO required using f_{sig} as a fit parameter. With the appropriate parameters mentioned in Table 10, the fit is displayed in Fig. 66.

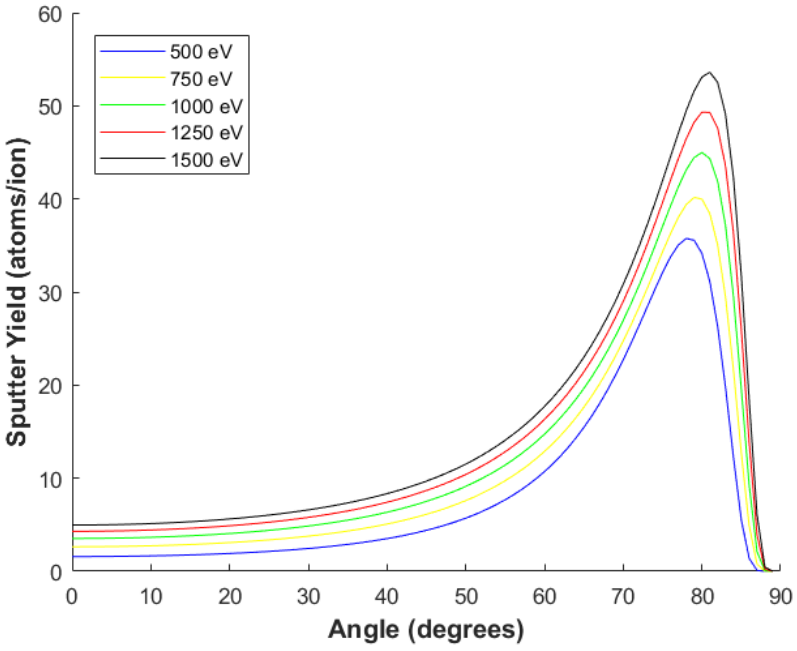

Fig. 66: ITO Angular Sputter Model

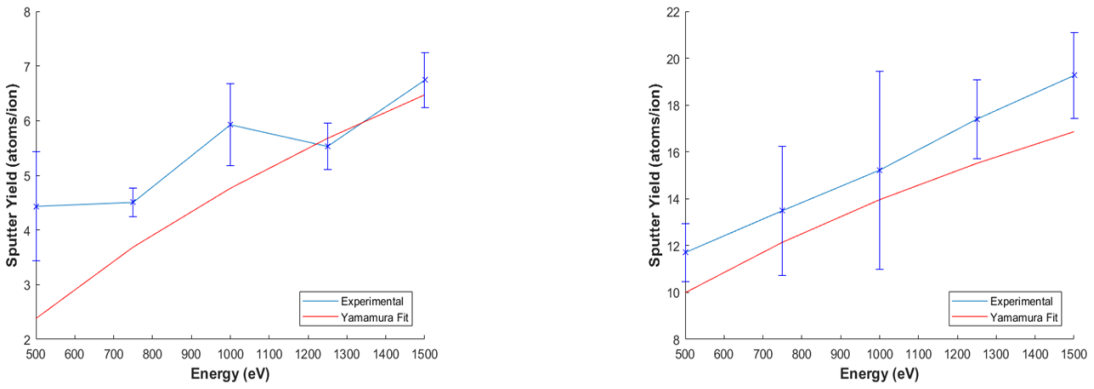

Fig. 67: ITO Angular Data Comparisons, 30° (left), 60° (right)

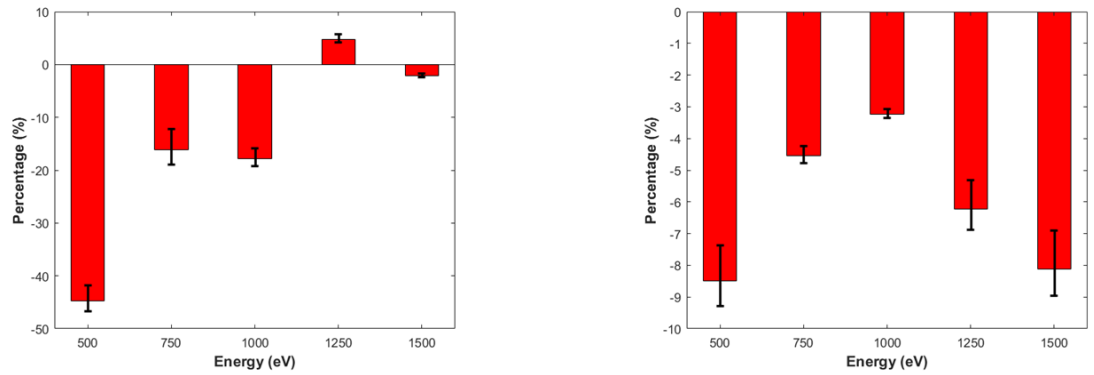

Fig. 68: ITO Angular Fit Comparisons, 30° (left), 60° (right)

As shown in Fig. 67 and Fig. 68, the angular model shows reasonable agreement within the 30° incidence data with the exception of the 500 eV data point, which is outside of the 30% boundary for noble gas sputtering. However, as mentioned in Chapter 8.2.2, the f_{sig} fitting may be partly responsible, as a similar issue has occurred with the MgF_2 data at this particular energy level, as well. With the exception of this particular experimental condition, all others are within 20% tolerance of the model. The 60° incidence shows excellent agreement with the model, with all test points within 10% of the Yamamura fit, although the model is slightly under-predicting the experimental data.

10. Formation Flight Erosion Study

10.1. Overview

As mentioned in Chapter 0, plasma plume erosion from spacecraft can inflict multiple types of damage to a spacecraft surface, most notably material erosion from direct impingement. Although a variety of missions try to design around plume impingement, there may be situations that arise that may not be able to avoid direct ion beam contact with another spacecraft. And, unlike CEX exposure from the plume, direct impingement from the plume is much more energetic and has the capability to leave a lasting impact on the surface of the spacecraft.

Under laboratory conditions, direct plume impingement is a simple matter and erosion can occur to a certain degree of predictability as long as the testing conditions are known. However, unlike the linear evolution of sputter from direct plume impingement, there are a few other factors to consider in orbit. The geomagnetic field at a given orbital altitude, the plume density, and the formation distance are just some of the factors that can affect the plume impingement properties of a formation.

This study aims to utilize a rudimentary model to observe the evolution of erosion effects of plume impingement while in orbit performing a representative maneuver. It will provide an estimate for depths of erosion caused by the impingement as well as how the environmental factors affect the plume's propagation and, ultimately, the erosion profile expected for a certain maneuver. The goal of this study is to provide general safe boundaries for spacecraft to operate within close formation.

10.2. Study Parameters

Although there are myriad orbital conditions that are of interest for this study, ultimately there were three types of orbital conditions that were considered: LEO, GEO, and Sun-Synchronous. Each of these orbits have very unique characteristics. LEO has the distinction of not only being the most popular orbital region of choice for most mission profiles but also having the highest geomagnetic field influence on the plume due its orbital altitude. Meanwhile, Sun-Synchronous orbit is of interest because of the number of high-profile formation flight missions taking place there, such as the A-Train satellite constellation. Finally, GEO is also an interesting profile for the orbital study as the geomagnetic field has very little influence at these distances, but they can possibly still be a factor.

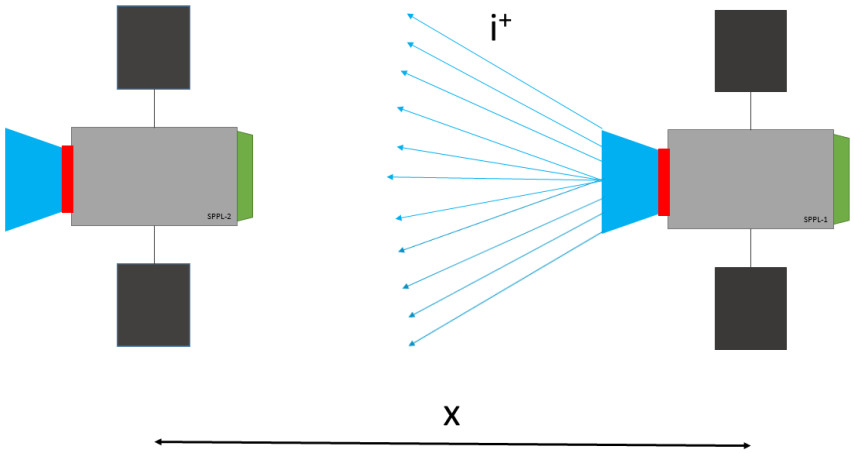

Fig. 69: Study Spacecraft in Leader-Follower Formation

The study will look at two spacecraft in each of these orbital scenarios, with them being in a leader-follower formation. The leader-follower formation, the most generic spaceflight formation, also presents the most direct possible path for the plume to follow, if unimpeded. This formation will be observed with a range of ISD's from 50-1000 m.

This study will also look at the effects of the plume's kinetic energy (ranging from 500-1500 eV) on the erosion of the surfaces.

As one would expect, the plume properties have a significant impact on the erosion profile of the target. As such, we have established parameters for the plume based on the plume density, derived from the BHT-HD-600 Hall thruster nominal operating parameters from Roberts[2] as well as Ekholm[66], which is $1.47x10^{18}$ #/m^3. This was to ensure that the test case of the model produced similar exposure results to the aforementioned efforts. The density, except when observing density effects on a particular orbit, will remain constant throughout the study. The summarized study parameters are located in Table 12.

Table 12: Formation Flight Study Parameters

Orbital Altitude	**Orbital Inclination (deg)**	**Formation Distance (m)**	**Beam Energy (eV)**	**Plume Density (#/m^3)**
LEO: 400 km	0-90 in 15 increments;	50, 100, 250 500,1000	500, 1000, 1500	$1.47x10^{18}$, $2.08x10^{18}$, $2.94x10^{18}$, $3.60x10^{18}$
Sun-Sync: 705 km	98.14	50, 100, 250 500,1000	500, 1000, 1500	$1.47x10^{18}$
GEO: 35786 km	0	50, 100, 250 500,1000	500, 1000, 1500	$1.47x10^{18}$

After establishing the parameters of the beam and the orbit, an orbital simulation is performed, which looks at the propagation of the plume and the potential impact on the follower spacecraft. After looking through an entire orbit, the model calculated the number of hits on the spacecraft and calculates the total exposure time to the follower spacecraft. The data output from this model also takes the geomagnetic environment around both spacecraft into account. With this and the knowledge of the beam parameters at the target, we can then estimate the erosion seen by the spacecraft through a simple erosion model with the time and apparent fluence of particles on the target. For further detail on both the erosion and orbital models, see Chapters 3 & 4, respectively.

10.2.1. Study Assumptions

Although the model used for this study has been described in detail in Chapter 4, there are also additional assumptions for the purposes of this analysis. The largest assumption to take into account is that the Earth is inertially fixed for the purposes of this model. That means that although the magnetic pole is used within this model, the magnetic pole is also fixed due to this assumption. Therefore, the geomagnetic field environment will not rotate as the spacecraft completes its orbit; this will introduce small variations in the local field relative to what would have been seen if the Earth's rotation was included. The degree of the variation would increase with each additional orbit. This approximation will have the greatest (but minor) impact on the Sun-sync orbits, a lesser impact on LEO orbits, and practically no effect on GEO orbits. Another assumption made for the geomagnetic field is that the field is approximately the same around both the leader and the follower spacecraft. This may not normally be the case for larger

formations, but for the ISD's observed within this effort, the difference between the magnetic fields are negligible.

As for the interaction criterion for the study, recall that the follower spacecraft is given a sphere of influence (SOI) involves a base interaction sphere for the spacecraft with an expanding diameter based on the plume width. This width is the expected width of the plume if it experienced purely ballistic expansion all the way to the expected ISD. The plume itself is considered to propagate ballistically with a 15° half-angle. A hit is considered if the plume intersects with the SOI of the spacecraft. This is determined if the difference of the distance between the position of the follower spacecraft (also represented as a center of mass) and the plume's center-of-mass is less than the tolerance factor and the representative radius of the spacecraft, as represented in Equation 10-1. For this study, the representative spacecraft SOI radius is 4 m, and the cross-sectional area for this spacecraft is based on this radius. This area is also split into three equal parts: one representing the aluminum structure and the other two representing the panels. It is important to note that while the area of the panel is 1/3 of the cross-sectional area in normal incidence, it is appropriately modified when entering an angled incidence, reducing the cross-sectional area accordingly.

$$\sqrt{\left(\vec{r}_{follower} - \vec{r}_{plume}\right)^2} + \leq tol + .004\ [km] \tag{10-1}$$

In relation to the plume interaction with the spacecraft, the plasma parameter β has a huge role to play in determining the plume's direction and other properties with respect to plume impingement. As mentioned in Section 2.3, β is the local ratio of plasma pressure to magnetic pressure. The plasma pressure, as shown in Equation 2-5, consists of

the electron and ion pressures as well as neutral pressure. For the purposes of this work, an electron temperature of 1 eV (or 11,604 K) was used and the ion temperature is represented as 10% of the electron temperature. This is reasonable, since in an electric thruster plume, the ions are sufficiently immobile compared to the electrons. It is important to note that the neutral pressure has been neglected for this analysis. However, due to the low temperature of the neutrals (~300 K) combined with the relatively low density of neutrals in most orbits, this should be a reasonable assumption.

Another important assumption to note is the rotation of the solar arrays during the orbit. Due to the simplicity of the model, the solar arrays will be fixed for all time during the analysis. However, we are instead looking at the best and worst case scenarios for panel erosion on orbit. Best case scenarios will keep the solar panels fixed at normal incidence throughout the orbit; worst case scenarios will keep the solar panels fixed at a 60° incidence angle throughout the orbit. While this is highly unrealistic due to the constantly changing position of the spacecraft in relation to the sun during most orbits, this effort's main goal is to find the potential amount of sputter in each of the orbits observed.

Finally, all orbits are assumed circular, with both argument of latitude and true longitude at epoch equal to 0°. Note that argument of perigee and true anomaly are not defined for circular orbits, and the right ascension is not defined for equatorial orbits.

10.3. Test Case Results

As mentioned above, the leader-follower formation from the effort by Roberts[2] was utilized to test the accuracy of the simulation efforts for this work. According to Roberts, the C-TOS leader-follower formation experienced particle impacts to the spacecraft for approximately 16-18 minutes during its one orbital maneuver within one portion of the orbit according to Fig. 70. It is also noteworthy to indicate that they expect the CEX impingement to have a higher flux of particles to the follower than from direct impingement itself, yet will contribute very little to erosion.

Table 13: C-TOS Leader-Follower Parameters [2]

Altitude	1100 km
Inclination	63.4°
ISD	500 m

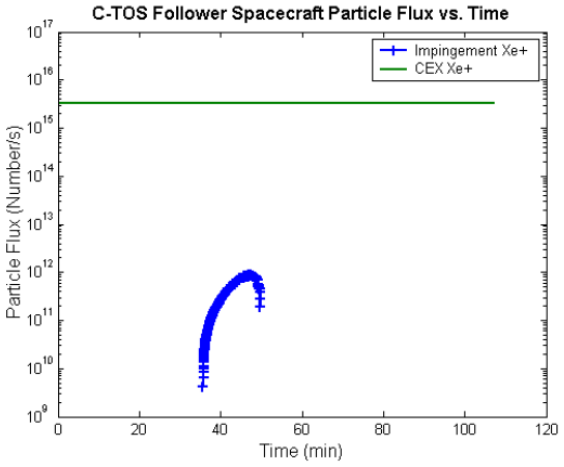

Fig. 70: C-TOS Impingement Flux [2]

The simulation from this effort, shows no correlation with the prior work. The simulation shows that the plume makes no contact with the follower spacecraft. Based on the magnetic field model shown in Chapter 4.2, the magnetic field strength of the C-TOS orbit is considerably strong, fluctuating between 18-35 μT as shown in Fig. 71. This field strength provides a strong magnetic braking effect when the β transition effect occurs.

This braking effect has an effect on the overall velocity of the plume as it propagates from the leader spacecraft. After the β transition effects are felt, the plume velocity is affected based on the local geomagnetic field vector. Not only does this serve to reduce the speed of the plume, it also changes the direction of the plume based on the local field vector. An example of the contrasting plume velocities are shown below in Fig. 72.

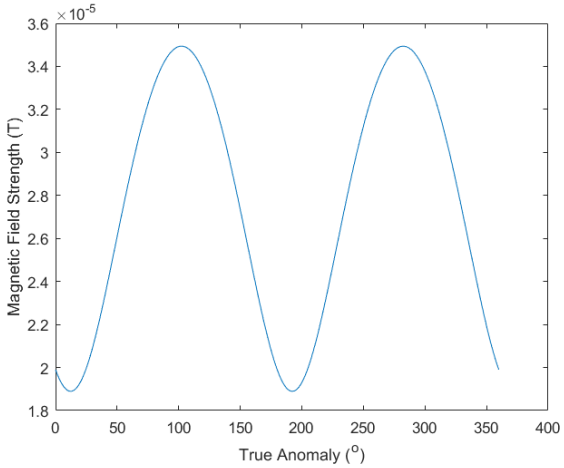

Fig. 71: C-TOS Geomagnetic Field Environment

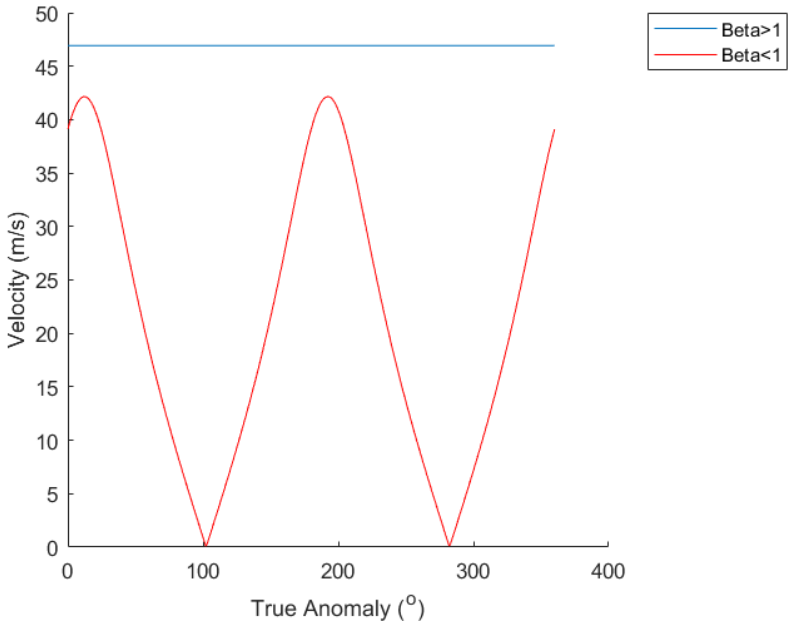

Fig. 72: Plume Velocity scenarios in C-TOS orbit

From the strength of the plume velocity, it is easy to see that the speed is clearly dictated by the strength of the magnetic field. But, because of the interference of the magnetic field, the plume also takes its direction, as well, as indicated in Equation 4-18.

This interference not only introduced the braking effect shown above, but it also turns the plume into the direction of the local magnetic field. Because of this, the plume as shown in this test case has at least 25° divergence from the plume centerline, as seen in Fig. 73.

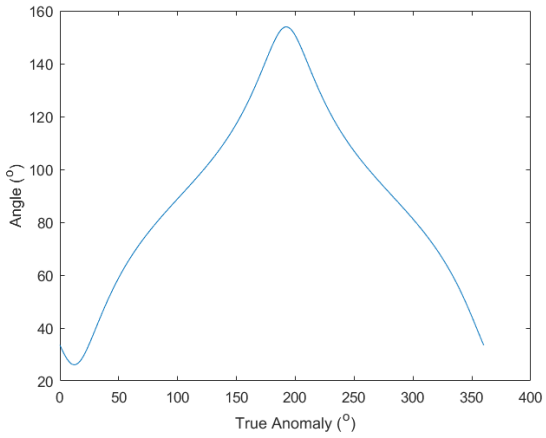

Fig. 73: C-TOS Plume Divergence Angle vs. True Anomaly

This divergence, in fact, can be clearly seen in the simulation as the leader-follower formation is modeled in orbit. As seen in Fig. 74, the plume (the red line) propagates normally for a short distance before the β transition point. After the transition, the plume

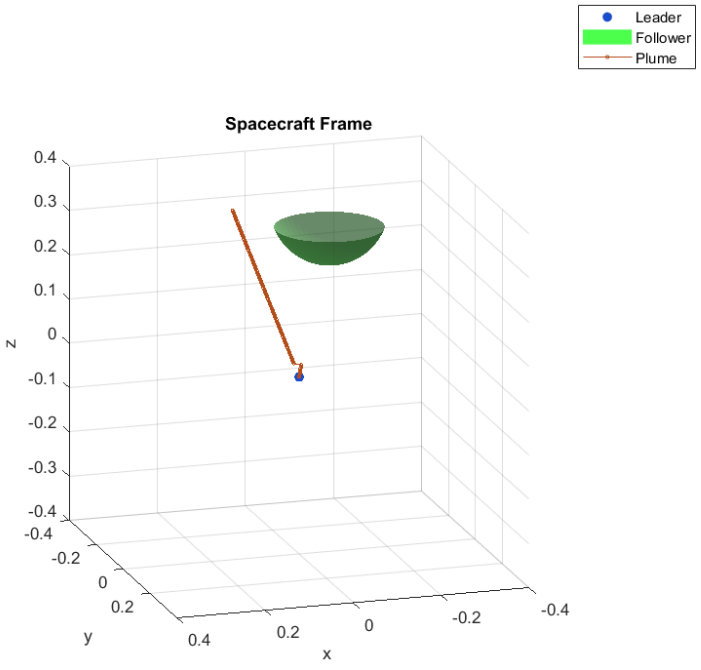

Fig. 74: C-TOS Plume Flight Path @ θ=0°

then diverges based on the local magnetic field vector as shown in Fig. 73. The plume, as shown, never intersects the sphere's SOI. It is noteworthy to mention that although the plume trajectory changes abruptly as the β transition occurs, this may be due to the lack of knowledge of the transition region as β nears 1. The change of direction is still expected, however, and does not change the overall result of this simulation.

10.4. LEO Case Study

Low Earth Orbit (LEO) is home to many Earth observation missions, and as such, could become a focal point for formation flight missions of all types in the near future. To this end, a comprehensive study was performed for a range of orbital inclinations as well as ISD's, as shown in Table 12. The orbital altitude chosen (400 km) coincides with the International Space Station (ISS). This section will work to summarize the results of the case study, with the majority of the data available in Appendix A.3. LEO Erosion Study Datasets. For reference, unless otherwise noted, the plume density used for these observations is 1.47×10^{18} #/m^3.

10.4.1. Plume Exposure Observations

Because of the strength of the geomagnetic field environment (shown in Fig. 75) at this altitude, there is very little erosion reported for the majority of orbital inclinations until i=75°. From here, although the field strength is much higher on

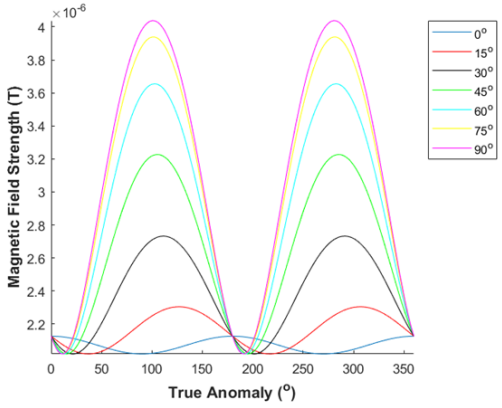

Fig. 75: LEO Geomagnetic Field Environment

average, there are also very large fluctuations of the field throughout the orbit. But, due to the alignment of the geomagnetic field, the plume exhibited by the leader spacecraft fails to propagate beyond a small distance from the spacecraft, preventing any erosion at most inclinations, even at ISD's of 50 m.

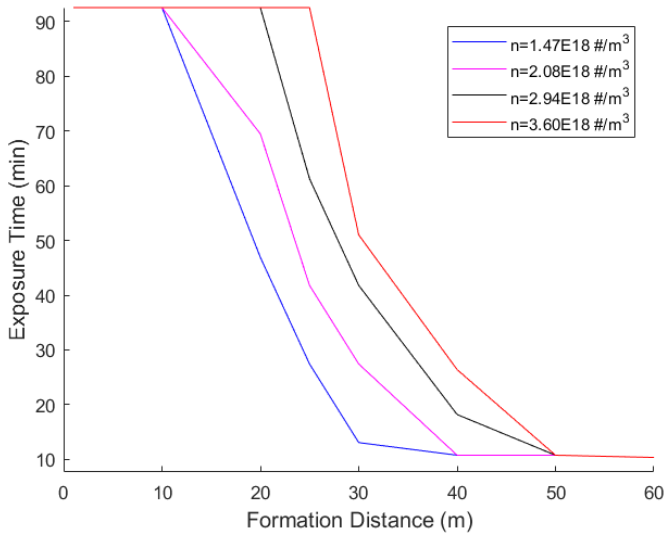

Fig. 76: Exposure Time vs. Formation Distance w.r.t. Density

The first noteworthy observation is the variance of the exposure properties of the plume with respect to the change in density. As Equation 2-5 would suggest, the plasma density is directly proportional to β and, as such, plays an important role in determining the interaction properties of the plume to the follower spacecraft. This is verified by looking at the impact of plume density on the exposure times at a single orbital inclination, as shown in Fig. 76. As expected, the transition point from complete exposure to partial exposure begins to shift farther away from the leader spacecraft at higher plume densities.

It is worth noting that the BHT-HD-600, which served as the basis for the assumed plume density, is a 600 W Hall thruster designed for only 36 mN of thrust[65]. As shown, just increasing the density by a factor of 2.5 extended the full exposure transition point by 15 m (150%). Therefore, it would stand to reason that high thrust EP systems would pose a much higher risk for close formation spaceflight missions, which is a reasonable expectation due to higher plume densities. This trend is also in agreement with the β modelling trends, as shown in Section 4.2.1.

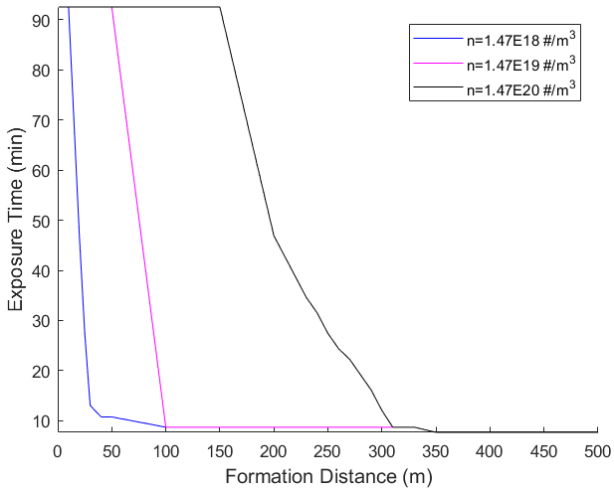

Fig. 77: Exposure Time vs. Formation Distance w.r.t. Density Magnitudes

However, at these density levels, the full exposure transition point still stays relatively close to the spacecraft. With this in mind, if we examine the behavior of the transition point as we increase the magnitude of the density, we find that the transition point moves much further towards the follower spacecraft, as shown in Fig. 77. With the first and second magnitude increases, we see a 500% increase in transition distance at 1.43×10^{19} #/m^3 (50 m) and a 1500% increase at 1.43×10^{20} #/m^3 (150 m), respectively. A density level of 10^{19} is consistent with another EP system, the SPT-100, a 1.35 kW

thruster[36]. At the highest magnitude analyzed, if we assume that all the other thruster characteristics are constant, then we can assume that the beam current will be increased, as shown in Equation 4-21. With this in mind, the density output would result in a tenfold increase in the power of the thruster to 13.5 kW, which puts it in the operating regime of the Pratt & Whitney T-220HT in both thrust current and output power[67].

Another noteworthy observation is the increase in exposure time with respect to the orbital inclination. As mentioned above, orbital erosion at the ISD's within this test show no erosion until a 75° inclination. However, at 75° and 90° inclinations, very small exposure times were reported for the leader-follower formation. This is due to the geomagnetic field environment mentioned above. Although the strength (and fluctuation) of the environment increase with the higher inclination, the exposure times as a whole increase slightly. Both inclinations show exposure times that are inversely proportional to the ISD. This is somewhat expected, as the density also decays in this fashion as the

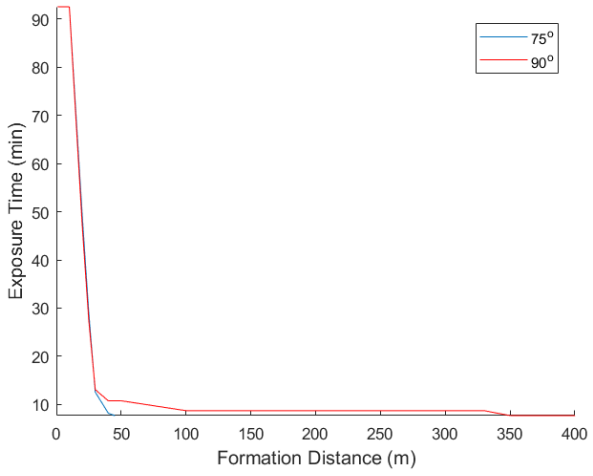

Fig. 78: Exposure Time vs. Formation Distance w.r.t. Inclination, n=1.47E18 #/m^3

plume propagates from the leader spacecraft. However, the higher inclination also shows a higher minimum of exposure time, which is expected due to the weaker magnetic field

at some portions of the orbit versus the lower inclination. These trends are shown in Fig. 78.

With the low plume exposure times in LEO, it is reasonable to assume that these incidences of erosion occur in small regions of the orbit where the magnetic field is weakest. These regions, according to the simulation, also indicate varying degrees of energy loss of the plume, which will be discussed in a later section.

10.4.2. LEO Erosion Results

With the plume interaction properties of LEO determined, we must look at the actual erosion characteristics from these orbital conditions. As expected, the trend of the erosion depths show an increasing linear trend with respect to both energy and time exposed. Likewise, at higher ISD's, the follower spacecraft experiences less erosion due to the quadratic drop in plume density. As mentioned above, there is no erosion reported for LEO with the exception of the higher orbital inclinations, specifically 75˚ and 90˚. Here, the orbital conditions allow for small windows of plume interaction that result in surface erosion on the follower spacecraft.

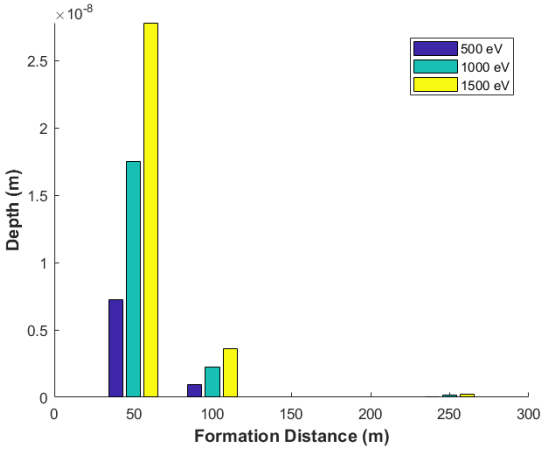

Fig. 79: LEO Al Sputter Data, *i*=75˚

As for the levels of erosion themselves, most cases show generally light erosion of aluminum, with the maximum erosion occurring at a beam energy of 1500 eV and ISD

of 50 m for all LEO orbital conditions, with a depth of approximately 30 nm based on the structural cross-section mentioned in Section 10.2.1. It is important to note that a layer of BoPET is 4.5 μm thick, so erosion of one layer of the BoPET sheath would take approximately 1500 orbits. As with all of the depths reported in this work, this depth is representative of one complete orbit with constant thrust.

Likewise, the AR coatings of the solar cells, in most of both the best and worst-cast scenarios, show minor amounts of erosion for the majority of the orbits that show erosion. However, in the best and worst case scenarios, there are some orbital parameters that show AR coating failure in one orbit. These come from a beam energy of 1500 eV and an ISD of 50 m. At these conditions, MgF_2 erosion ranging from 55 to 130 nm is observed in the best and worst cases, respectively; similarly, ITO shows erosion depths of 411 and 754 nm for the best and worst cases. This, according to Yalin[52], would significantly affect the transmission properties of the coating, thereby experiencing a significant drop in power to the solar cells. And, as expected from earlier chapters, MgF_2 is significantly more resistant to plasma erosion than ITO in all cases, as the erosion is practically an order of magnitude higher in all cases when exposed to the same flux levels. It is also noteworthy that due to the higher erosion rates of ITO, there are more orbital conditions in which significant damage or outright failure of the AR coating occurs. Represented in Fig. 80 below shows the representative trends of the AR sputtering.

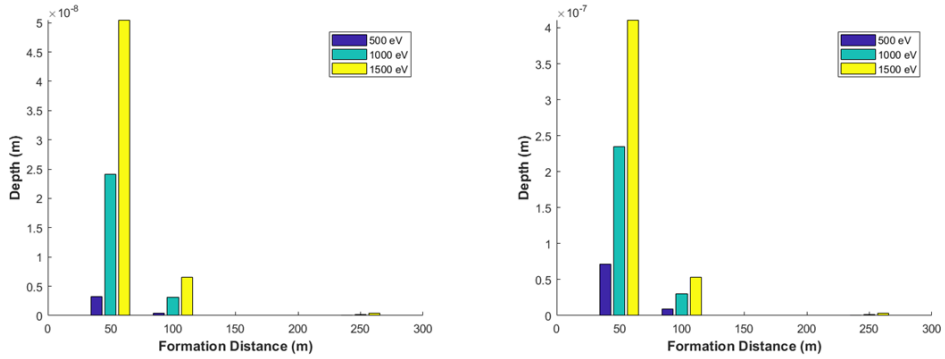

Fig. 80: LEO AR Sputter Data, *i*=75°-MgF_2 (right) and ITO (left)

The remainder of the sputter data covering all scenarios can be located in Appendix A.3. LEO Erosion Study Datasets.

10.5. Sun-Synchronous Erosion Results

Sun-Synchronous orbits are a unique case within this study due to the fact that, unlike the other two orbital conditions, this type of orbit always has the solar panels locked in a 90° incidence, where sputter of the AR coating is not possible. It is also unique due to the significant variation of the magnetic field for this set of orbital conditions. While there are many Sun-Sync orbits that can be observed, this particular orbit observed belongs to the A-Train[68] constellation, which has many satellites in leader-follower formations,

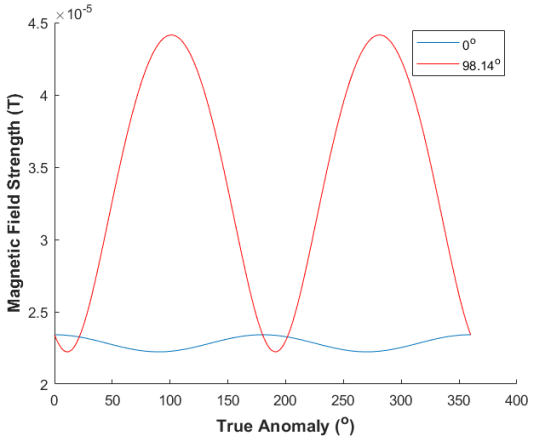

Fig. 81: Sun-Sync Geomagnetic Environment

but at distances much larger than those observed in this study.

As shown with the LEO study, the magnetic field oscillation does increase proportionally to the orbital inclination. As such, due to these high oscillations, there are small pockets of exposure at higher ISD's that also show energy loss at these locations. Overall, the erosion environment is similar to the environment found in LEO at 90° inclination. The sputter depth levels are also very similar, but due to being in a higher orbit than from the LEO study, the orbital period is slightly longer, resulting in slightly higher levels of erosion. The sputter depths displayed show the expected quadratic fall in sputter depth as the flux falls due to the distance from the beam exit, as shown in Fig. 82.

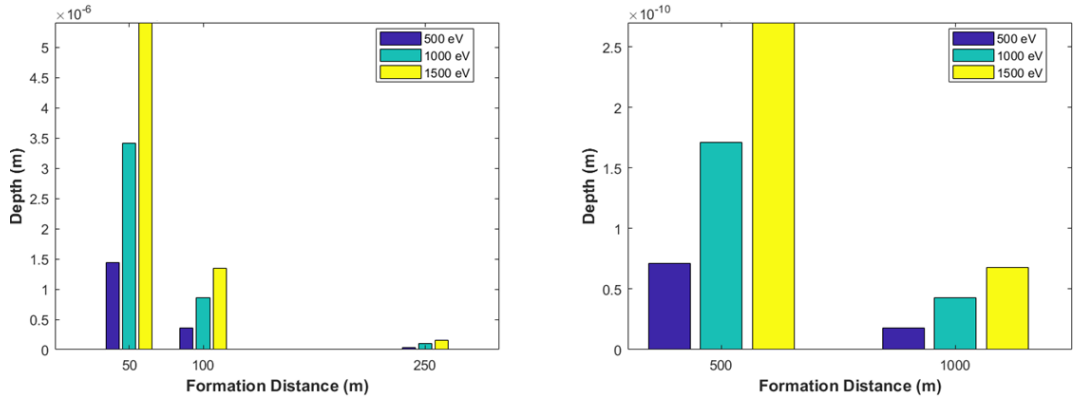

Fig. 82: Sun-Sync Sputter Depth Data

10.6. GEO Erosion Results

As noted in the earlier sections, the geomagnetic field weakens as the orbital altitude increases, resulting in a more dangerous impingement environment than can be seen at lower altitudes. However, due to orbital inclination (0° inclination), the magnetic field fluctuations seen will be similar to that of LEO at that inclination, but with a substantially lower field magnitude (0.4% of LEO-400 km). With these conditions in mind, β is expected to be significantly larger than the others in the study due to the weakness in the geomagnetic field.

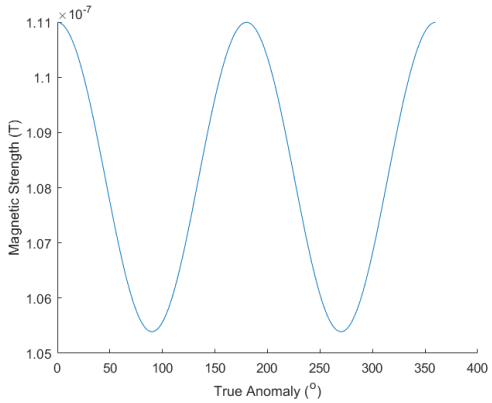

Fig. 83: GEO Geomagnetic Field Environment

Because of the orbital conditions, the erosion profile remains constant for all ISD's examined at this orbital altitude. With β>>1, the beam constantly propagates and does not get overcome by the local magnetic pressure in this region. Furthermore, because of the constant thrusting throughout one orbit during this maneuver, the erosion threat is very high, with the orbital period being approximately 24 hours. The erosion data shows, as expected, very significant levels of erosion for all materials, reaching as high as ~79 µm of Al erosion, 0.15 mm (best case) for MgF_2, and 1.2 mm (best case) for ITO for plume exposure at 1500 eV and 50 m ISD. Even at best-case scenarios for the AR coatings, at these levels the 100 nm thick AR coatings will be completely sputtered away and the coverglass will begin to erode; this will result is a significant loss in

efficiency of the solar panel. The erosion results will be contained in Appendix A.5. GEO Erosion Study Datasets.

10.7. Energy Loss Observations

As mentioned in the previous sections, there were multiple instances throughout the study in which there were regions of the orbit in which the plume still managed to impinge on the follower spacecraft, but at slightly reduced energy levels than those normally held by the plume. These regions, although odd at first, can be explained by the interactions of the magnetic field with the velocity vector of the plume. As shown in Equation 4-18, the velocity vector when $\beta<1$ is dependent on the dot product, or the projection, of the velocity, $\vec{v}$, on the magnetic field vector, $\vec{B}$. With this in mind, these energy loss regions all take place where $\beta<1$; therefore, these energy loss regions are the direct result of magnetic braking due to the interaction of the field with the velocity. It is also reasonable to assume that within these regions, there would be a sufficiently low magnetic field to allow for the beam to impinge on the spacecraft.

For example, one set of orbital conditions that this energy loss phenomenon occurs at is during Sun-Sync at an ISD of 500 m. Here, there was a very small amount of exposure to the plume during the orbit. This exposure was shown to occur both in instances where there was a very weak magnetic field as well as a β slightly less than 1. As reasoned above, the energy loss occurs also during the minima of the magnetic field strength experienced through these orbital conditions. This also occurs at the 1000 m ISD, but with even less exposure. This is shown in Fig. 84.

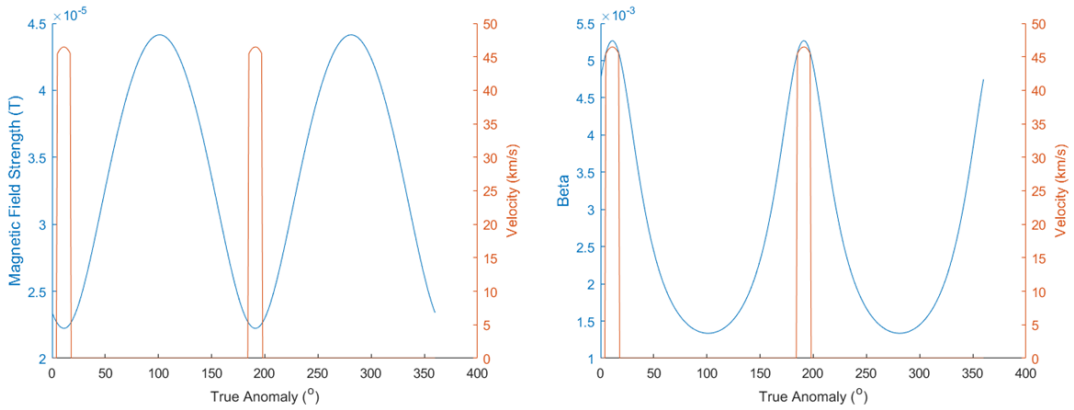

Fig. 85: Sun-Sync Magnetic Field Strength and Impact Velocity vs. Orbital Position (left); Sun-Sync Beta and Impact Velocity vs. Orbital Position (right)

As reasoned above, the energy loss is a result of the geomagnetic field interaction with the ion plume. When β<1, the plume velocity becomes a product of the projection of the velocity vector on the geomagnetic vector and the geomagnetic vector itself. As a result, when β<1, the plume velocity essentially becomes directly proportional to the geomagnetic field. This will result in reduced velocities when β<1 if the vector allows for direct impingement to the follower spacecraft. It is also observed that during these instances of impingement, while the magnitude of the velocity is slightly reduced, the majority of these instances show a near-zero velocity along one axis, as shown in Fig. 85.

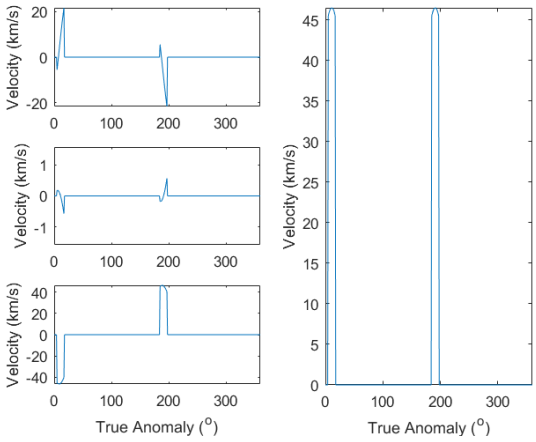

Fig. 84: Sun-Sync Velocity Vector, ISD 500 m, Energy: 1500 eV (right); Velocity X-Axis (top left), Velocity Y-Axis (mid left), Velocity Z-Axis (bottom left)

Like in the Sun-Sync case, similar results were shown at LEO in similar conditions, as well. Unlike in Sun-Sync, however, the erosion occurs at slightly higher magnetic field strength, as shown in Fig. 86. This means that these energy loss regions occur only when the magnetic field vector allows for the impingement in addition to the strength of the field.

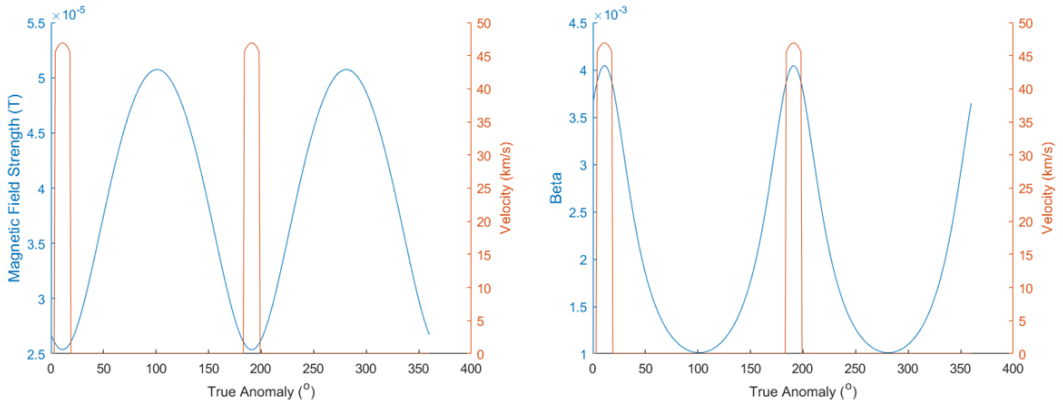

Fig. 86: LEO Magnetic Field Strength and Impact Velocity vs. Orbital Position (left); LEO Beta and Impact Velocity vs. Orbital Position (right)

10.8. Application of Erosion Results

Now that the erosion properties of the plume have been observed in many orbital scenarios, we must utilize this data to analyze how spacecraft (and their individual components) would hold up to plume impingement over extended periods of time. By establishing these performance trends, we can then apply this information to potential mission designs and assess the risk of these components during the extent of a spacecraft's primary mission. This section will look at the erosion trends over extended periods of time and how they will affect a typical five-year mission profile. For reference, a table with the appropriate material parameters is shown below.

Table 14: Formation Failure Study Material Parameters

Material	Representative Thickness (nm)
Aluminum (Al)	4500
Magnesium Fluoride (MgF_2)	100
Indium Tin Oxide (ITO)	100

10.8.1. Failure Trends

With access to the single-orbit erosion data established from the previous sections, we can now apply this data to look at the failure trends of the observed materials under constant plume impingement from the leader spacecraft. This can be performed by looking at the ratio of the material thickness to the erosion depth caused by the single orbit erosion, as shown in Equation 10-2.

$$N_{orbits} = \frac{d_{layer}}{d_{erosion}} \tag{10-2}$$

This ratio can tell us N_{orbits}, the number of orbits until the failure of one layer of the material under observation. Because of the nature of the ratio, the number of orbits tends to rise quadratically, as the erosion depth falls quadratically with distance, as shown from the data in previous sections.

10.8.1.1. LEO Failure Trends

Using the above technique, we can observe the failure trends established by the sputter in LEO from Section 10.4.2. Observing the sputter on Aluminum, it is reasonable to assume that under the constant thrust conditions of the erosion study, it will take a considerable amount of time to erode one full layer. This assumption is confirmed in Fig.

87. This graph shows, as expected, that the erosion of the material decreases quadratically as the formation distance increases. This also shows that the slight increase in exposure time based on inclination introduces a near order of magnitude change in failure limits.

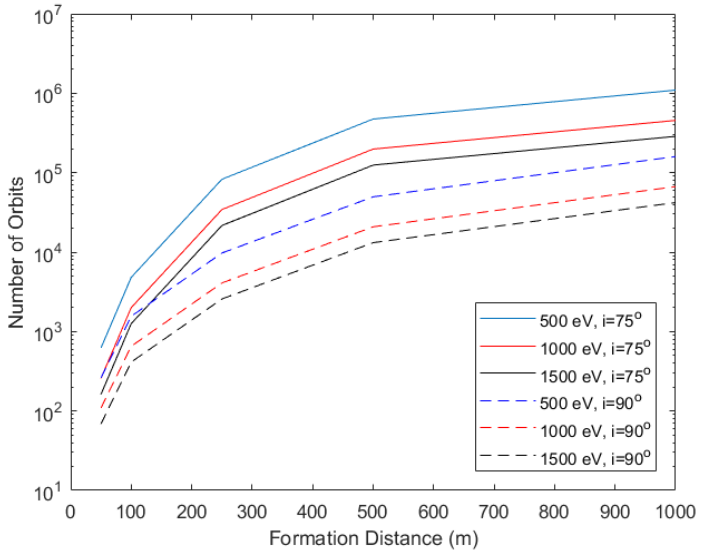

Fig. 87: LEO Orbits until Failure, Aluminum

Likewise, as with the Al erosion data, the erosion data for the AR coatings also follows these erosion trends. For both of these materials, the orbits until failure are drastically different mainly due to the significant difference in the thickness of the AR coating versus the Al mono-layer. However, when the results are observed solely amongst this class of materials, the study shows that MgF_2 lasts an order of magnitude longer than ITO solely due to the sputter yields of the material.

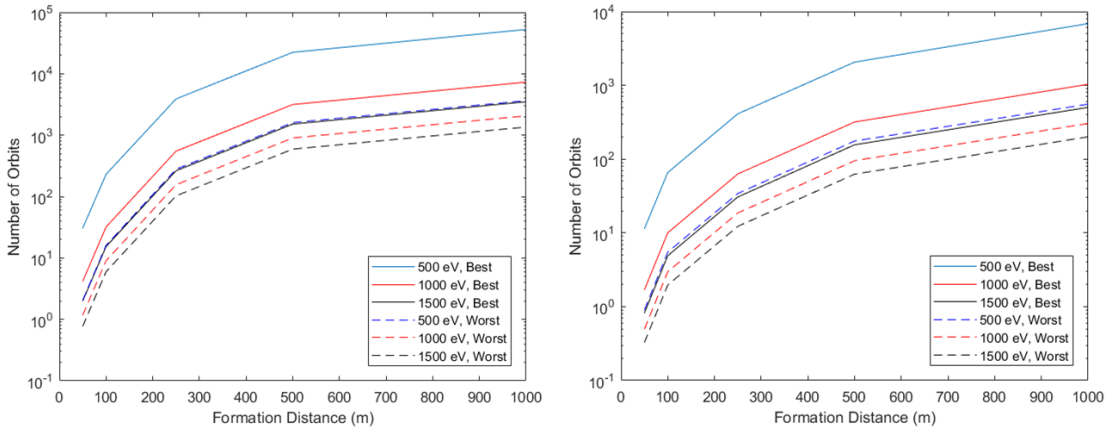

Fig. 88: LEO Orbits Until Failure, MgF_2 Best Case (left) and Worst Case (right)

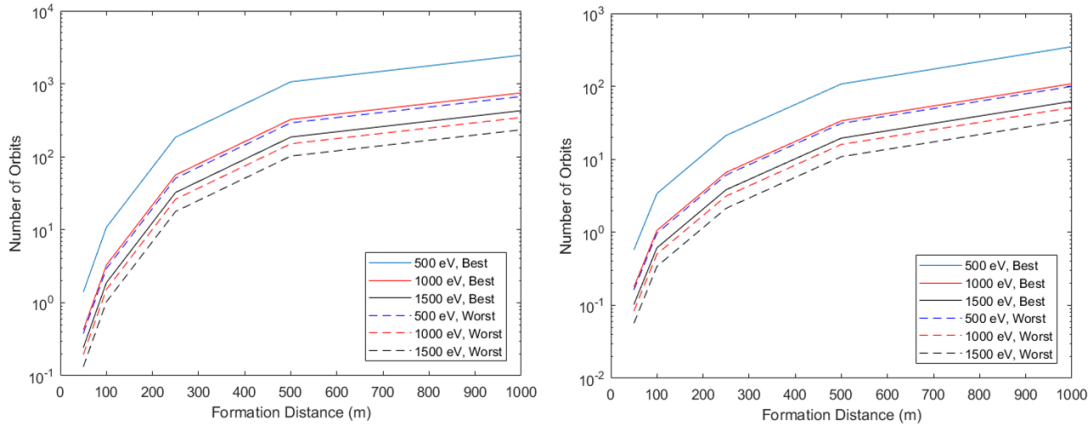

Fig. 89: LEO Orbits Until Failure, ITO Best Case (left) and Worst Case (right)

10.8.1.2. Sun-Synchronous Failure Trends

For the Sun-Sync orbital cases, similar failure trends are shown. Due to the inclination of these orbits, more geomagnetic protection is received than in LEO at 90˚ inclination. As such, the aluminum will receive higher protection at these orbits, despite the longer exposure times due to the orbital period. These results are shown in Fig. 90.

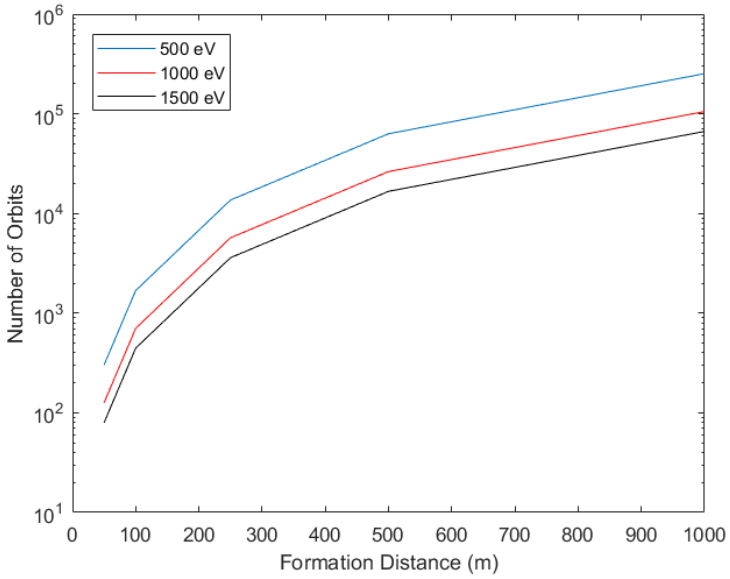

Fig. 90: Sun-Sync Orbits Until Failure, Al

10.8.1.3. GEO Failure Trends

As with the other two orbital altitudes observed, the failure trends at GEO also share similar trending. However, with the significant reduction in strength of the magnetic field versus the previous altitudes, the exposure threat is much higher, with some materials not even lasting the full orbit under constant thrust. In addition to the

weakness of the magnetic field, there is also the increased orbital period to consider, as well. The results are shown below.

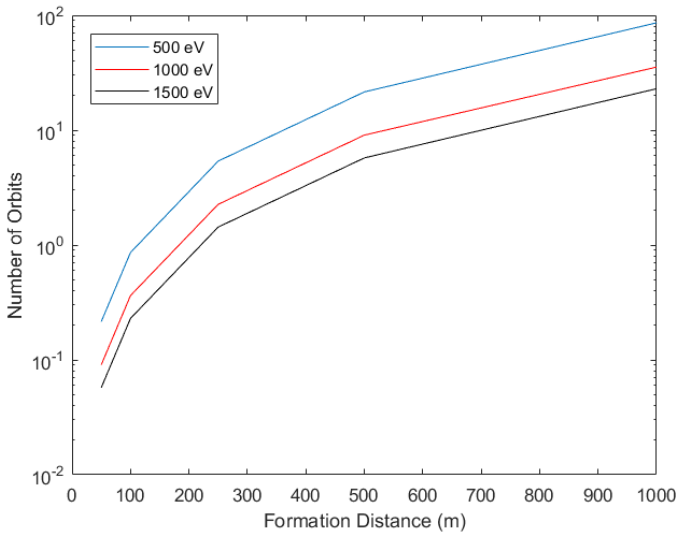

Fig. 91: GEO Orbits Until Failure, Al

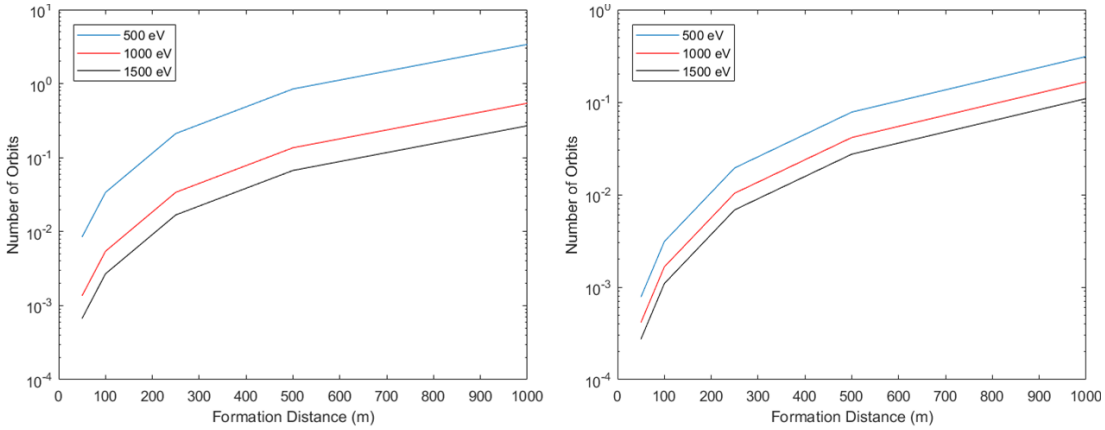

Fig. 92: GEO Orbits Until Failure, MgF_2 Best Case (left) and Worst Case (right)

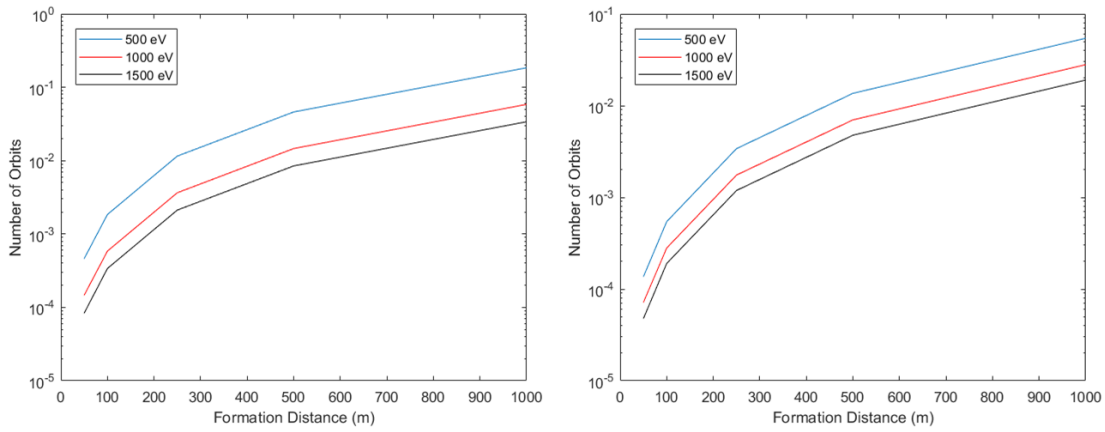

Fig. 93: GEO Orbits Until Failure, ITO Best Case (left) and Worst Case (right)

10.8.2. Five-Year Mission

One of the primary applications of this research is to inform decisions when it comes to developing a design that can last throughout a spacecraft's primary mission. With this in mind, we can design a sample mission using these failure estimates to come up with a potential design that can last throughout the mission life-cycle. For this analysis, we will assume a pair of spacecraft in a leader-follower formation with a primary mission duration of five years. During the mission timeframe, we will only assume that the spacecraft will have to make maintenance maneuvers throughout the duration that will directly impinge on the follower spacecraft. Therefore, unlike the analysis from the previous sections, we will not assume constant thrust, but instead assume the total amount of thrust time equivalent to the delta-v required for these maneuvers. We will also use the appropriate parameters from the previous formation study. Finally, the worst case scenario for the solar panel erosion will be assumed.

Each orbital altitude utilizes different orbital maneuvers for spacecraft to maintain their position. For LEO, the primary maneuvers that will be required are for drag

mitigation purposes in order to maintain the altitude required for the mission. Sun-Sync orbits usually require maneuvers for inclination maintenance to maintain their orbits. Also, one of GEO's main maneuvers is E-W stationkeeping to maintain the vehicle's position within the orbit. The annual delta-v requirements for LEO and Sun-Sync/GEO are 25 m/s and 2 m/s, respectively[69]. In order to estimate the duration of the maneuvers, we will use a spacecraft mass of 2000 kg.

Based on the annual delta-v budgets required for maintenance maneuvers, we can determine the total number of maintenance orbits required throughout the entire mission. It is important to note that "orbits" in this context may not necessarily be full orbits, but the number of orbits that represent the amount of time for thruster firings throughout the entire mission. Because of the nature of the orbit, LEO requires the highest thrust time, requiring at least 250 orbits worth of thrust time. GEO required the second-most maneuvers, followed by Sun-Sync. The table representing the maintenance orbits is shown in Table 15.

Table 15: Five-Year Sample Mission Maintenance Orbits

Beam Energy (eV)	LEO Maintenance Orbits	Sun-Sync Maintenance Orbits	GEO Maintenance Orbits
500	750	3.9	56.5
1000	375	1.93	28.05
1500	250	1.3	18.7

The results from this study show that for these missions, the limiting factor of the designs are not the Al layers within the multi-layer insulation, but the AR coatings. This is an expected result due to the thickness of the AR coating applied to the solar cells as well as the higher potential for angled incidence exposure. Another expected result is that the lower orbital altitudes provide a much longer mission life due to the geomagnetic protection from Earth. Likewise, GEO is the hardest altitude to design for, based on the lack of geomagnetic protection and amount of thrust time required. The results are shown in Table 16.

Table 16: Five-Year Sample Mission Design Results

Orbit	Materials	ISD (m)	# of orbits	Years until Failure
LEO 75˚	Al/MgF_2	500	591 (1500 eV)	11.8
LEO 90˚	Al/MgF_2	>1000*	555 (500 eV)	3.7
Sun-Sync	All	50	79 (1500 eV)	21.1
GEO	Al/MgF_2	>1000*	0.3 (500 eV)	0.4

Note: If ">1000*" is listed, then the minimum distance for this altitude is beyond 1000 m, the maximum distance tested in this study. The # of orbits presented for those orbital altitudes are those if the ISD were 1000 m.

11. Conclusions and Future Work

With the findings of this effort, we can see the effects of EP plumes on spacecraft in formation flight. If not properly designed for, plume impingement can present a very serious threat to the health and welfare of spacecraft in even simple formations. This section looks at the conclusions from this effort and some of the possible future avenues this research can be taken.

11.1. Conclusions

Due to the erosion properties of the AR coatings, even a small amount of exposure over the course of an orbit can significantly reduce the effectiveness of the solar panel due to the changes in transmission properties of the coating. We have also shown at lower orbital altitudes where the magnetic field is reasonably strong (~10^{-5} T), the magnetic field provides sufficient protection at most orbital inclinations from plume impingement. At those orbital conditions that show erosion, we have also demonstrated that significant changes in the plume density can alter its interaction properties with both the spacecraft and the local magnetic field.

However, at higher altitudes, where the magnetic field grows weaker, the threat for direct impingement increases significantly to where the protections of the geomagnetic field prove inadequate. Also, due to the study in LEO (400 km altitude), we have shown that at higher inclinations, the magnetic field oscillations can play a significant factor in allowing for plume impingement, even at larger ISD's, due to the local magnetic field vector. Because of this interaction, we can also expect to see a local weakening of the plume energy via magnetic braking based on the interactions between the geomagnetic field and plume.

This effort has also provided both experimental and theoretical data for the sputtering yields of popular AR coatings for solar cell coverglasses as well as extended the data set for a key structural component of spacecraft and the reflective surface coating of multi-layer insulation (i.e.: aluminum). Through the experiments with these materials, we have demonstrated that MgF_2 is indeed a more sputter-resistant AR coating for space operations. In practical performance situations, MgF_2 coatings last an order of magnitude longer than ITO coatings. However, depending on the mission application and formation specifics, ITO may be a viable alternative as long as the threat of direct ion plume impingement is minimal. The sputter data from this work can be used for a wide variety of purposes in the engineering community, primarily in the applications of sputter processes and mission design.

11.2. Future Work

There are a few research paths that may be viable for future directions of this work. In terms of the sputter yield data, the need to expand the current Yamamura theory for compound sputtering exists. Although using f_{sig} as a fitting parameter can generate sufficient results for compound targets, the ability to find theoretical estimates of this parameter may prove beneficial. If f_{sig} was found theoretically, one would be able to generate theoretical Yamamura curves for these types of materials. As a result, it would be possible to predict sputtering conditions for these materials and be able to apply these models to either mission design of components or sputter experiments for experimental validation.

As for the experimental data, the testing itself was limited due to the logistic difficulties of the propellant needed for the study. It is recommended to fill in the gaps of

the sputter data with the intermediate incidence angles. This study would serve to either further validate the theoretical fits established in this work or allow the fits to be refined. In particular, it would be beneficial for the purpose of refining the model fit parameters to identify the critical angle where peak erosion occurs. There is also a potential opening at looking that the specific topography effects of each material due to the impingement experienced. While some topography observations were made during the early phases of this work with the SPPL-1, no further research was established in this area [60]. Observing the changes of the surface composition, as well as observing the defects on a microscopic scale, may give an even clearer picture to the dangers of plasma erosion of spacecraft.

The simulation work provided within this effort can be extended by examining other types of formation flight, such as the bistatic formation shown in Fig. 24. This would be a logical expansion of this work since the entire formation is at an angle to the target, creating a potentially more hazardous sputter situation for the follower spacecraft. However, because of the possible maneuvers that can be performed with these spacecraft, further thought may have to be given to the types of maneuvers performed based on the erosion characteristics, especially at higher orbital altitudes and inclinations.

Finally, the erosion study should be expanded to looking beyond circular orbits. Although the study here presents the baseline of what one could expect to see, some orbits have eccentricity. As a result, the altitude changes as the spacecraft propagates throughout the orbit. Depending on the eccentricity of the orbit, these altitude changes would introduce changes in the magnetic field environment, and therefore changes in the impingement possibilities of the orbit. Orbital transfers, such as Hohmann transfers,

would also present an interesting case for this study for the altitude changes and thrust time required to generate the delta-v for the maneuver.

Appendix A: Individual Sample Sputter Yield Data

A.1. Magnesium Fluoride Samples

Table 17: Magnesium Fluoride Normal Incidence Sputter Data

Energy (eV)	Sample #	Average Ion Rate (ions/sec)	Ion Rate Std. Dev (%)	Duration (min)	Depth (μm)	Sputter Yield (atoms/ion)
500	1	7.04E12	3.93	45	5.38E-2	0.2585
500	6	7.47E12	2.56	90	1.03E-1	0.2327
500	7	1.03E13	1.85	90	1.44E-1	0.2370
750	4	1.19E13	17.68	30	1.27E-1	0.5433
750	8	7.77E12	6.28	60	1.88E-1	0.6133
750	9	8.75E12	4.26	60	1.78E-1	0.5157
750	10	1.81E13	6.85	60	4.26E-1	0.5974
1000	4	5.27E12	7.75	45	1.59E-1	1.0189
1000	5	9.97E12	4.07	45	2.73E-1	0.9264
1000	6	1.02E13	7.27	45	2.89E-1	0.9575
1250	5	2.15E13	1.70	15	3.84E-1	1.8113
1250	6	1.12E13	2.72	15	1.70E-1	1.5373
1250	8	1.21E13	5.65	20	2.57E-1	1.6151
1500	6	1.10E13	5.76	10	1.62E-1	2.2364
1500	7	1.71E13	2.84	15	2.95E-1	1.7513

Table 18: Magnesium Fluoride 30° Sputter Data

Energy (eV)	Sample #	Average Ion Rate (ions/sec)	Ion Rate Std. Dev (%)	Duration (min)	Depth (μm)	Sputter Yield (atoms/ion)
500	4	1.83E12	3.42	60	1.02E-1	1.4061
500	5	1.87E12	3.65	60	1.03E-1	1.3995
500	8	1.69E12	5.10	120	1.83E-1	1.3770
750	3	4.76E12	5.92	30	1.81E-1	1.9229
750	4	2.78E12	2.83	90	3.12E-1	1.8930
750	6	4.05E12	5.21	90	2.82E-1	1.1747
1000	1	4.73E12	6.44	60	3.33E-1	1.7888
1000	2	4.35E12	6.49	60	3.05E-1	1.9264
1000	12	7.84E12	6.31	15	1.40E-1	1.8130
1250	1	1.38E13	4.86	25	3.22E-1	1.6151
1250	2	1.19E13	4.22	25	3.33E-1	1.4205
1250	3	7.63E12	1.80	40	1.95E-1	1.7070
1250	4	4.08E12	1.62	40	3.60E-1	3.3540
1250	9	5.31E12	1.96	15	1.81E-1	3.4600
1250	10	4.36E12	1.82	40	3.04E-1	2.6568
1500	1	1.36E13	8.49	20	4.31E-1	2.4173
1500	4	7.90E12	8.07	20	2.14E-1	2.0627
1500	7	1.32E13	2.10	10	2.63E-1	3.0382

Table 19: Magnesium Fluoride 60° Sputter Data

Energy (eV)	Sample #	Average Ion Rate (ions/sec)	Ion Rate Std. Dev (%)	Duration (min)	Depth (μm)	Sputter Yield (atoms/ion)
500	1	1.06E12	2.67	75	3.91E-1	7.4961
500	3	9.87E11	3.11	120	5.08E-1	6.5253
500	4	2.39E12	3.01	61	4.46E-1	4.6580
750	1	1.63E12	1.73	30	2.31E-1	7.1993
750	2	1.54E12	1.68	30	1.71E-1	5.6558
750	4	3.52E12	5.73	15	1.97E-1	5.6887
1000	2	3.40E12	2.07	20	3.82E-1	8.5613
1000	4	2.26E12	1.38	15	2.65E-1	11.8850
1000	5	2.57E12	1.56	15	2.11E-1	8.3358
1250	4	1.07E13	9.13	4.75	3.67E-1	10.9799
1250	6	8.95E12	8.08	4.75	3.87E-1	13.8560
1250	7	6.30E12	9.69	4.75	2.47E-1	12.5822
1500	9	9.45E12	7.13	4.75	4.46E-1	15.1309
1500	10	3.33E12	13.54	4.75	1.92E-1	18.4845
1500	11	6.35E12	7.75	4.75	3.06E-1	15.4597

A.2. Indium Tin Oxide Samples

Table 20: Indium Tin Oxide Normal Incidence Sputter Data

Energy (eV)	Sample #	Average Ion Rate (ions/sec)	Ion Rate Std. Dev (%)	Duration (min)	Depth (μm)	Sputter Yield (atoms/ion)
500	1	5.66E12	3.34	10	2.54E-1	2.2457
500	2	6.26E12	7.99	10	2.09E-1	1.6733
500	3	5.70E12	8.24	10	2.06E-1	1.8125
750	1	5.37E12	97.58	10	3.57E-1	3.3239
750	2	1.02E13	3.42	10	4.45E-1	2.1825
750	3	9.89E12	2.39	10	5.41E-1	2.7369
750	4	1.44E13	8.91	10	5.06E-1	1.7579
1000	1	1.37E13	2.30	5	5.10E-1	3.7275
1000	2	1.11E13	3.36	5	4.26E-1	3.8412
1000	3	1.48E13	3.18	5	3.32E-1	2.2475
1000	4	1.73E13	5.66	5	4.12E-1	2.3865
1250	1	1.15E13	3.34	2.5	2.84E-1	4.9497
1250	2	1.25E13	3.81	2.5	2.96E-1	4.7415
1250	3	1.38E13	3.63	2.5	3.06E-1	4.4405
1250	4	2.43E13	8.25	3	4.87E-1	3.3431
1500	1	1.38E13	2.42	2.5	4.25E-1	6.1591
1500	2	1.50E13	2.85	2.5	3.49E-1	4.6562
1500	3	1.28E13	2.61	2.5	3.97E-1	6.2054
1500	4	1.54E13	5.24	3	2.82E-1	3.8240

Table 21: Indium Tin Oxide 30° Sputter Data

Energy (eV)	Sample #	Average Ion Rate (ions/sec)	Ion Rate Std. Dev (%)	Duration (min)	Depth (µm)	Sputter Yield (atoms/ion)
500	1	1.93E12	12.10	10	1.45E-1	3.7725
500	2	2.03E12	9.90	10	1.57E-1	3.8760
500	3	1.71E12	10.40	10	1.93E-1	5.6473
750	1	4.87E12	11.73	10	4.61E-1	4.7362
750	2	4.80E12	10.76	10	4.39E-1	4.5769
750	3	3.70E12	22.51	10	3.11E-1	4.2011
1000	1	5.69E12	6.85	5	2.85E-1	5.0205
1000	4	6.31E12	6.75	5	3.94E-1	6.2424
1000	5	4.77E12	5.99	5	3.11E-1	6.5103
1250	1	7.97E12	8.25	5	4.26E-1	5.3542
1250	2	9.33E12	8.48	5	4.84E-1	5.1954
1250	3	7.66E12	10.06	5	4.62E-1	6.0353
1500	2	5.82E12	8.17	5	4.44E-1	7.6372
1500	7	1.21E13	2.17	2.75	4.39E-1	6.5801
1500	8	1.00E13	8.33	2.75	3.46E-1	6.3001

Table 22: Indium Tin Oxide 60° Sputter Data

Energy (eV)	Sample #	Average Ion Rate (ions/sec)	Ion Rate Std. Dev (%)	Duration (min)	Depth (µm)	Sputter Yield (atoms/ion)
500	1	7.61E11	2.59	8	1.53E-1	12.5850
500	3	2.26E12	3.15	8	3.91E-1	10.8182
500						
750	1	1.47E12	1.08	6	2.65E-1	15.0173
750	3	1.88E12	1.95	6	3.46E-1	15.3355
750	4	4.82E12	1.72	5	4.87E-1	10.1191
1000	1	2.38E12	3.47	4	3.77E-1	19.8492
1000	2	3.20E12	2.84	4	3.81E-1	14.9133
1000	3	3.99E12	2.47	4	3.48E-1	10.9035
1250	1	2.56E12	1.26	3	2.96E-1	19.2964
1250	3	2.66E12	0.88	3	2.74E-1	17.1458
1250	4	3.42E12	2.10	3	3.23E-1	15.7556
1500	1	2.36E12	0.93	1.5	1.38E-1	19.5092
1500	2	4.79E12	0.68	1.5	2.47E-1	17.2011
1500	3	3.72E12	0.85	1.5	2.35E-1	21.0764

A.3. LEO Erosion Study Datasets

Table 23: LEO (400 km altitude) @ i=75°, Aluminum

ISD (m)	Energy (eV)	Time (min)	Flux ($^{\#}/_{m^2\text{-}s}$)	Depth (m)	Energy Loss? (Y/N)
50	500	7.179	1.18E+18	7.24E-09	Y
	1000	7.179	1.67E+18	1.75E-08	Y
	1500	7.179	2.05E+18	2.78E-08	Y
100	500	5.1278	2.12E+17	9.36E-10	Y
	1000	5.1278	3.00E+17	2.25E-09	Y
	1500	5.1278	3.68E+17	3.58E-09	Y
250	500	3.0767	2.05E+16	5.44E-11	Y
	1000	3.0767	2.89E+16	1.31E-10	Y
	1500	3.0767	3.54E+16	2.08E-10	Y
500	500	2.5639	4.26E+15	9.50E-12	Y
	1000	2.5639	6.03E+15	2.27E-11	Y
	1500	2.5639	7.38E+15	3.61E-11	Y
1000	500	2.0511	2.33E+15	4.11E-12	Y
	1000	2.0511	3.30E+15	9.89E-12	Y
	1500	2.0511	4.04E+15	1.57E-11	Y

Table 24: LEO (400 km altitude) @ i=75°, MgF2, Best Case Scenario

ISD (m)	Energy (eV)	Time (min)	Flux ($^{\#}/_{m^2\text{-}s}$)	Depth (m)	Energy Loss? (Y/N)
50	500	7.179	1.18E+18	3.28E-09	Y
	1000	7.179	1.67E+18	2.41E-08	Y
	1500	7.179	2.05E+18	5.05E-08	Y
100	500	5.1278	2.12E+17	4.35E-10	Y
	1000	5.1278	3.00E+17	3.13E-09	Y
	1500	5.1278	3.68E+17	6.53E-09	Y
250	500	3.0767	2.05E+16	2.57E-11	Y
	1000	3.0767	2.89E+16	1.82E-10	Y
	1500	3.0767	3.54E+16	3.80E-10	Y
500	500	2.5639	4.26E+15	4.48E-12	Y
	1000	2.5639	6.03E+15	3.17E-11	Y
	1500	2.5639	7.38E+15	6.60E-11	Y
1000	500	2.0511	2.33E+15	1.90E-12	Y
	1000	2.0511	3.30E+15	1.37E-11	Y
	1500	2.0511	4.04E+15	2.86E-11	Y

Table 25: LEO (400 km altitude) @ i=75°, MgF2, Worst Case Scenario

ISD (m)	Energy (eV)	Time (min)	Flux ($^{\#}/_{m^2\text{-}s}$)	Depth (m)	Energy Loss? (Y/N)
50	500	7.179	1.18E+18	4.89E-08	Y
	1000	7.179	1.67E+18	8.58E-08	Y
	1500	7.179	2.05E+18	1.30E-07	Y
100	500	5.1278	2.12E+17	6.24E-09	Y
	1000	5.1278	3.00E+17	1.11E-08	Y
	1500	5.1278	3.68E+17	1.68E-08	Y
250	500	3.0767	2.05E+16	3.59E-10	Y
	1000	3.0767	2.89E+16	6.41E-10	Y
	1500	3.0767	3.54E+16	9.73E-10	Y
500	500	2.5639	4.26E+15	6.24E-11	Y
	1000	2.5639	6.03E+15	1.11E-10	Y
	1500	2.5639	7.38E+15	1.69E-10	Y
1000	500	2.0511	2.33E+15	2.74E-11	Y
	1000	2.0511	3.30E+15	4.85E-11	Y
	1500	2.0511	4.04E+15	7.37E-11	Y

Table 26: LEO (400 km altitude) @ i=75°, ITO, Best Case Scenario

ISD (m)	Energy (eV)	Time (min)	Flux ($^{\#}/_{m^2\text{-}s}$)	Depth (m)	Energy Loss? (Y/N)
50	500	7.179	1.18E+18	7.11E-08	Y
	1000	7.179	1.67E+18	2.35E-07	Y
	1500	7.179	2.05E+18	4.11E-07	Y
100	500	5.1278	2.12E+17	9.25E-09	Y
	1000	5.1278	3.00E+17	3.04E-08	Y
	1500	5.1278	3.68E+17	5.31E-08	Y
250	500	3.0767	2.05E+16	5.39E-10	Y
	1000	3.0767	2.89E+16	1.77E-09	Y
	1500	3.0767	3.54E+16	3.08E-09	Y
500	500	2.5639	4.26E+15	9.38E-11	Y
	1000	2.5639	6.03E+15	3.07E-10	Y
	1500	2.5639	7.38E+15	5.36E-10	Y
1000	500	2.0511	2.33E+15	4.05E-11	Y
	1000	2.0511	3.30E+15	1.33E-10	Y
	1500	2.0511	4.04E+15	2.33E-10	Y

Table 27: LEO (400 km altitude) @ i=75°, ITO, Worst Case Scenario

ISD (m)	Energy (eV)	Time (min)	Flux ($^{\#}/_{m^2\text{-}s}$)	Depth (m)	Energy Loss? (Y/N)
50	500	7.179	1.18E+18	2.64E-07	Y
	1000	7.179	1.67E+18	5.11E-07	Y
	1500	7.179	2.05E+18	7.54E-07	Y
100	500	5.1278	2.12E+17	3.40E-08	Y
	1000	5.1278	3.00E+17	6.58E-08	Y
	1500	5.1278	3.68E+17	9.70E-08	Y
250	500	3.0767	2.05E+16	1.97E-09	Y
	1000	3.0767	2.89E+16	3.81E-09	Y
	1500	3.0767	3.54E+16	5.62E-09	Y
500	500	2.5639	4.26E+15	3.42E-10	Y
	1000	2.5639	6.03E+15	6.62E-10	Y
	1500	2.5639	7.38E+15	9.77E-10	Y
1000	500	2.0511	2.33E+15	1.49E-10	Y
	1000	2.0511	3.30E+15	2.89E-10	Y
	1500	2.0511	4.04E+15	4.26E-10	Y

Table 28: LEO (400 km altitude) @ i=90°, Aluminum

ISD (m)	Energy (eV)	Time (min)	Flux ($^{\#}/_{m^2\text{-}s}$)	Depth (m)	Energy Loss? (Y/N)
50	500	10.7685	1.81E+18	1.73E-08	Y
	1000	10.7685	2.57E+18	4.14E-08	Y
	1500	10.7685	3.14E+18	6.55E-08	Y
100	500	8.7173	3.70E+17	2.89E-09	Y
	1000	8.7173	5.23E+17	6.89E-09	Y
	1500	8.7173	6.41E+17	1.09E-08	Y
250	500	8.7173	5.92E+16	4.62E-10	Y
	1000	8.7173	8.37E+16	1.10E-09	Y
	1500	8.7173	1.02E+17	1.75E-09	Y
500	500	7.6918	1.31E+16	9.06E-11	Y
	1000	7.6918	1.85E+16	2.16E-10	Y
	1500	7.6918	2.27E+16	3.42E-10	Y
1000	500	7.6918	4.12E+15	2.82E-11	Y
	1000	7.6918	5.82E+15	6.74E-11	Y
	1500	7.6918	7.13E+15	1.07E-10	Y

Table 29: LEO (400 km altitude) @ i=90°, MgF2, Best Case Scenario

ISD (m)	Energy (eV)	Time (min)	Flux ($^{\#}/_{m^2\text{-}s}$)	Depth (m)	Energy Loss? (Y/N)
50	500	10.7685	1.81E+18	8.80E-09	Y
	1000	10.7685	2.57E+18	5.91E-08	Y
	1500	10.7685	3.14E+18	1.22E-07	Y
100	500	8.7173	3.70E+17	1.52E-09	Y
	1000	8.7173	5.23E+17	9.96E-09	Y
	1500	8.7173	6.41E+17	2.04E-08	Y
250	500	8.7173	5.92E+16	2.43E-10	Y
	1000	8.7173	8.37E+16	1.59E-09	Y
	1500	8.7173	1.02E+17	3.26E-09	Y
500	500	7.6918	1.31E+16	4.85E-11	Y
	1000	7.6918	1.85E+16	3.14E-10	Y
	1500	7.6918	2.27E+16	6.40E-10	Y
1000	500	7.6918	4.12E+15	1.46E-11	Y
	1000	7.6918	5.82E+15	9.69E-11	Y
	1500	7.6918	7.13E+15	1.99E-10	Y

Table 30: LEO (400 km altitude) @ i=90°, MgF2, Worst Case Scenario

ISD (m)	Energy (eV)	Time (min)	Flux ($^{\#}/_{m^2\text{-}s}$)	Depth (m)	Energy Loss? (Y/N)
50	500	10.7685	1.81E+18	1.11E-07	Y
	1000	10.7685	2.57E+18	2.02E-07	Y
	1500	10.7685	3.14E+18	3.06E-07	Y
100	500	8.7173	3.70E+17	1.82E-08	Y
	1000	8.7173	5.23E+17	3.36E-08	Y
	1500	8.7173	6.41E+17	5.09E-08	Y
250	500	8.7173	5.92E+16	2.92E-09	Y
	1000	8.7173	8.37E+16	5.37E-09	Y
	1500	8.7173	1.02E+17	8.15E-09	Y
500	500	7.6918	1.31E+16	5.69E-10	Y
	1000	7.6918	1.85E+16	1.05E-09	Y
	1500	7.6918	2.27E+16	1.60E-09	Y
1000	500	7.6918	4.12E+15	1.80E-10	Y
	1000	7.6918	5.82E+15	3.29E-10	Y
	1500	7.6918	7.13E+15	4.99E-10	Y

Table 31: LEO (400 km altitude) @ i=90°, ITO, Best Case Scenario

ISD (m)	Energy (eV)	Time (min)	Flux ($^{\#}/_{m^2\text{-}s}$)	Depth (m)	Energy Loss? (Y/N)
50	500	10.7685	1.81E+18	1.74E-07	Y
	1000	10.7685	2.57E+18	5.63E-07	Y
	1500	10.7685	3.14E+18	9.78E-07	Y
100	500	8.7173	3.70E+17	2.94E-08	Y
	1000	8.7173	5.23E+17	9.41E-08	Y
	1500	8.7173	6.41E+17	1.63E-07	Y
250	500	8.7173	5.92E+16	4.70E-09	Y
	1000	8.7173	8.37E+16	1.51E-08	Y
	1500	8.7173	1.02E+17	2.61E-08	Y
500	500	7.6918	1.31E+16	9.27E-10	Y
	1000	7.6918	1.85E+16	2.96E-09	Y
	1500	7.6918	2.27E+16	5.12E-09	Y
1000	500	7.6918	4.12E+15	2.86E-10	Y
	1000	7.6918	5.82E+15	9.19E-10	Y
	1500	7.6918	7.13E+15	1.60E-09	Y

Table 32: LEO (400 km altitude) @ i=90°, ITO, Worst Case Scenario

ISD (m)	Energy (eV)	Time (min)	Flux ($^{\#}/_{m^2\text{-}s}$)	Depth (m)	Energy Loss? (Y/N)
50	500	10.7685	1.81E+18	6.18E-07	Y
	1000	10.7685	2.57E+18	1.20E-06	Y
	1500	10.7685	3.14E+18	1.77E-06	Y
100	500	8.7173	3.70E+17	1.03E-07	Y
	1000	8.7173	5.23E+17	1.99E-07	Y
	1500	8.7173	6.41E+17	2.93E-07	Y
250	500	8.7173	5.92E+16	1.64E-08	Y
	1000	8.7173	8.37E+16	3.19E-08	Y
	1500	8.7173	1.02E+17	4.69E-08	Y
500	500	7.6918	1.31E+16	3.21E-09	Y
	1000	7.6918	1.85E+16	6.24E-09	Y
	1500	7.6918	2.27E+16	9.19E-09	Y
1000	500	7.6918	4.12E+15	1.00E-09	Y
	1000	7.6918	5.82E+15	1.95E-09	Y
	1500	7.6918	7.13E+15	2.87E-09	Y

A.4. Sun-Synchronous Erosion Study Dataset

Table 33: Sun-Sync (705 km altitude) @ i=98.14°, Aluminum

ISD (m)	Energy (eV)	Time (min)	Flux ($^{\#}/_{m^2\text{-}s}$)	Depth (m)	Energy Loss? (Y/N)
50	500	10.4079	1.63E+18	1.49E-08	Y
	1000	10.4079	2.31E+18	3.57E-08	Y
	1500	10.4079	2.83E+18	5.66E-08	Y
100	500	8.7645	3.45E+17	2.67E-09	Y
	1000	8.7645	4.88E+17	6.40E-09	Y
	1500	8.7645	5.98E+17	1.01E-08	Y
250	500	7.669	4.85E+16	3.30E-10	Y
	1000	7.669	6.86E+16	7.89E-10	Y
	1500	7.669	8.40E+16	1.25E-09	Y
500	500	7.1212	1.13E+16	7.14E-11	Y
	1000	7.1212	1.59E+16	1.71E-10	Y
	1500	7.1212	1.95E+16	2.70E-10	Y
1000	500	7.1212	2.82E+15	1.78E-11	Y
	1000	7.1212	3.98E+15	4.27E-11	Y
	1500	7.1212	4.88E+15	6.76E-11	Y

A.5. GEO Erosion Study Datasets

Table 34: GEO (35786 km altitude) @ i=0°, Aluminum

ISD (m)	Energy (eV)	Time (min)	Flux ($^{\#}/_{m^2\text{-}s}$)	Depth (m)	Energy Loss? (Y/N)
50	500	1.44E+03	1.59E+19	2.09E-05	N
	1000	1.44E+03	2.25E+19	4.97E-05	N
	1500	1.44E+03	2.76E+19	7.85E-05	N
100	500	1.44E+03	3.98E+18	5.23E-06	N
	1000	1.44E+03	5.63E+18	1.24E-05	N
	1500	1.44E+03	6.90E+18	1.96E-05	N
250	500	1.44E+03	6.37E+17	8.37E-07	N
	1000	1.44E+03	9.01E+17	1.99E-06	N
	1500	1.44E+03	1.10E+18	3.14E-06	N
500	500	1.44E+03	1.59E+17	2.09E-07	N
	1000	1.44E+03	2.25E+17	4.97E-07	N
	1500	1.44E+03	2.76E+17	7.85E-07	N
1000	500	1.44E+03	3.98E+16	5.23E-08	N
	1000	1.44E+03	5.63E+16	1.24E-07	N
	1500	1.44E+03	6.90E+16	1.96E-07	N

Table 35: GEO (35786 km altitude) @ i=0°, MgF2, Best Case Scenario

ISD (m)	Energy (eV)	Time (min)	Flux ($^{\#}/_{m^2\text{-}s}$)	Depth (m)	Energy Loss? (Y/N)
50	500	1.44E+03	1.59E+19	1.18E-05	N
	1000	1.44E+03	2.25E+19	7.35E-05	N
	1500	1.44E+03	2.76E+19	1.49E-04	N
100	500	1.44E+03	3.98E+18	2.95E-06	N
	1000	1.44E+03	5.63E+18	1.84E-05	N
	1500	1.44E+03	6.90E+18	3.71E-05	N
250	500	1.44E+03	6.37E+17	4.72E-07	N
	1000	1.44E+03	9.01E+17	2.94E-06	N
	1500	1.44E+03	1.10E+18	5.94E-06	N
500	500	1.44E+03	1.59E+17	1.18E-07	N
	1000	1.44E+03	2.25E+17	7.35E-07	N
	1500	1.44E+03	2.76E+17	1.49E-06	N
1000	500	1.44E+03	3.98E+16	2.95E-08	N
	1000	1.44E+03	5.63E+16	1.84E-07	N
	1500	1.44E+03	6.90E+16	3.71E-07	N

Table 36: GEO (35786 km altitude) @ i=0°, MgF2, Worst Case Scenario

ISD (m)	Energy (eV)	Time (min)	Flux ($^{\#}/_{m^2\text{-}s}$)	Depth (m)	Energy Loss? (Y/N)
50	500	1.44E+03	1.59E+19	1.28E-04	N
	1000	1.44E+03	2.25E+19	2.41E-04	N
	1500	1.44E+03	2.76E+19	3.65E-04	N
100	500	1.44E+03	3.98E+18	3.21E-05	N
	1000	1.44E+03	5.63E+18	6.03E-05	N
	1500	1.44E+03	6.90E+18	9.14E-05	N
250	500	1.44E+03	6.37E+17	5.14E-06	N
	1000	1.44E+03	9.01E+17	9.65E-06	N
	1500	1.44E+03	1.10E+18	1.46E-05	N
500	500	1.44E+03	1.59E+17	1.28E-06	N
	1000	1.44E+03	2.25E+17	2.41E-06	N
	1500	1.44E+03	2.76E+17	3.65E-06	N
1000	500	1.44E+03	3.98E+16	3.21E-07	N
	1000	1.44E+03	5.63E+16	6.03E-07	N
	1500	1.44E+03	6.90E+16	9.14E-07	N

Table 37: GEO (35786 km altitude) @ i=0°, ITO, Best Case Scenario

ISD (m)	Energy (eV)	Time (min)	Flux ($^{\#}/_{m^2\text{-}s}$)	Depth (m)	Energy Loss? (Y/N)
50	500	1.44E+03	1.59E+19	2.17E-04	N
	1000	1.44E+03	2.25E+19	6.84E-04	N
	1500	1.44E+03	2.76E+19	1.20E-03	N
100	500	1.44E+03	3.98E+18	5.42E-05	N
	1000	1.44E+03	5.63E+18	1.71E-04	N
	1500	1.44E+03	6.90E+18	2.95E-04	N
250	500	1.44E+03	6.37E+17	8.67E-06	N
	1000	1.44E+03	9.01E+17	2.74E-05	N
	1500	1.44E+03	1.10E+18	4.72E-05	N
500	500	1.44E+03	1.59E+17	2.17E-06	N
	1000	1.44E+03	2.25E+17	6.84E-06	N
	1500	1.44E+03	2.76E+17	1.18E-05	N
1000	500	1.44E+03	3.98E+16	5.42E-07	N
	1000	1.44E+03	5.63E+16	1.71E-06	N
	1500	1.44E+03	6.90E+16	2.95E-06	N

Table 38: GEO (35786 km altitude) @ i=0°, ITO, Worst Case Scenario

ISD (m)	Energy (eV)	Time (min)	Flux ($^{\#}/_{m^2\text{-}s}$)	Depth (m)	Energy Loss? (Y/N)
50	500	1.44E+03	1.59E+19	7.34E-04	N
	1000	1.44E+03	2.25E+19	1.40E-03	N
	1500	1.44E+03	2.76E+19	2.10E-03	N
100	500	1.44E+03	3.98E+18	1.84E-04	N
	1000	1.44E+03	5.63E+18	3.57E-04	N
	1500	1.44E+03	6.90E+18	5.26E-04	N
250	500	1.44E+03	6.37E+17	2.94E-05	N
	1000	1.44E+03	9.01E+17	5.71E-05	N
	1500	1.44E+03	1.10E+18	8.41E-05	N
500	500	1.44E+03	1.59E+17	7.34E-06	N
	1000	1.44E+03	2.25E+17	1.43E-05	N
	1500	1.44E+03	2.76E+17	2.10E-05	N
1000	500	1.44E+03	3.98E+16	1.84E-06	N
	1000	1.44E+03	5.63E+16	3.57E-06	N
	1500	1.44E+03	6.90E+16	5.26E-06	N

Appendix B: Data Observations

B.1. f_{sig} Fitting

During Chapters 8 and 9, the parameter of f_{sig} had to be turned into a fitting parameter in order to establish the Yamamura curve fit that is seen in those chapters. Because the fitting of compound materials to a Yamamura curve has so little prior work, it was necessary to find a solution in order to provide the theoretical fit within this effort.

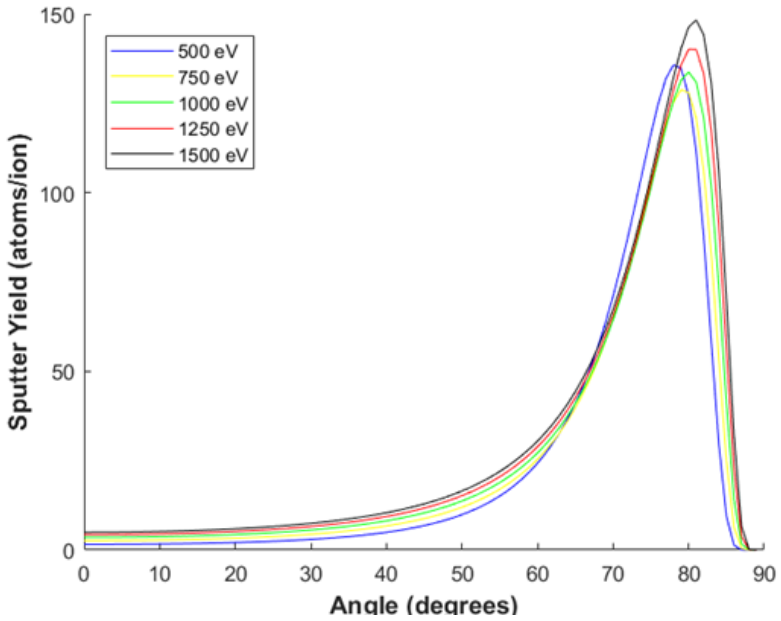

Fig. 94: Original ITO Angular Model, *f*=1.7850

Initially, the f_{sig} value used was an amalgamation of the corresponding values of the elemental composition of the compounds. However, although this seemed a reasonable plan, this also led to the curves yielding unreasonably high sputter yields for the majority of incidence angles, as shown above in Fig. 94. The reason for this is unconfirmed, as of this writing, but it may have to do with the interaction of the lattice geometry and the sputter interaction.

Through multiple fitting sessions, we determined the f_{sig} parameters that are shown in the above chapters. However, the question arose of potentially finding an f_{sig} that could fit the 30˚ and 60˚ incidences well individually. This would seem to be straightforward, however, as would be evident, this is no small task. On the contrary, it may be infeasible to do this purely because of the structure of the curve fit.

The structure of the curve fit, based on the Yamamura equation itself (Equation 3-11), makes it easier to manipulate the fit at higher incidence angles closer to the peak of the curve than at the lower angles in the quasi-linear section of the curve. The figures below show the adjustment from the f_{sig} used within the effort to the potential fitting of the 30˚ incidence.

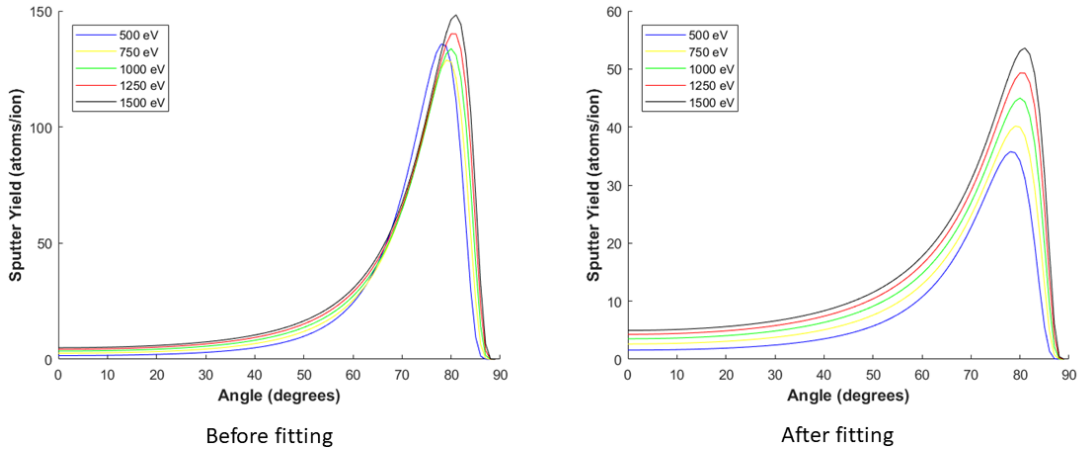

Fig. 95: Comparison of original f_{sig} to accepted f_{sig}

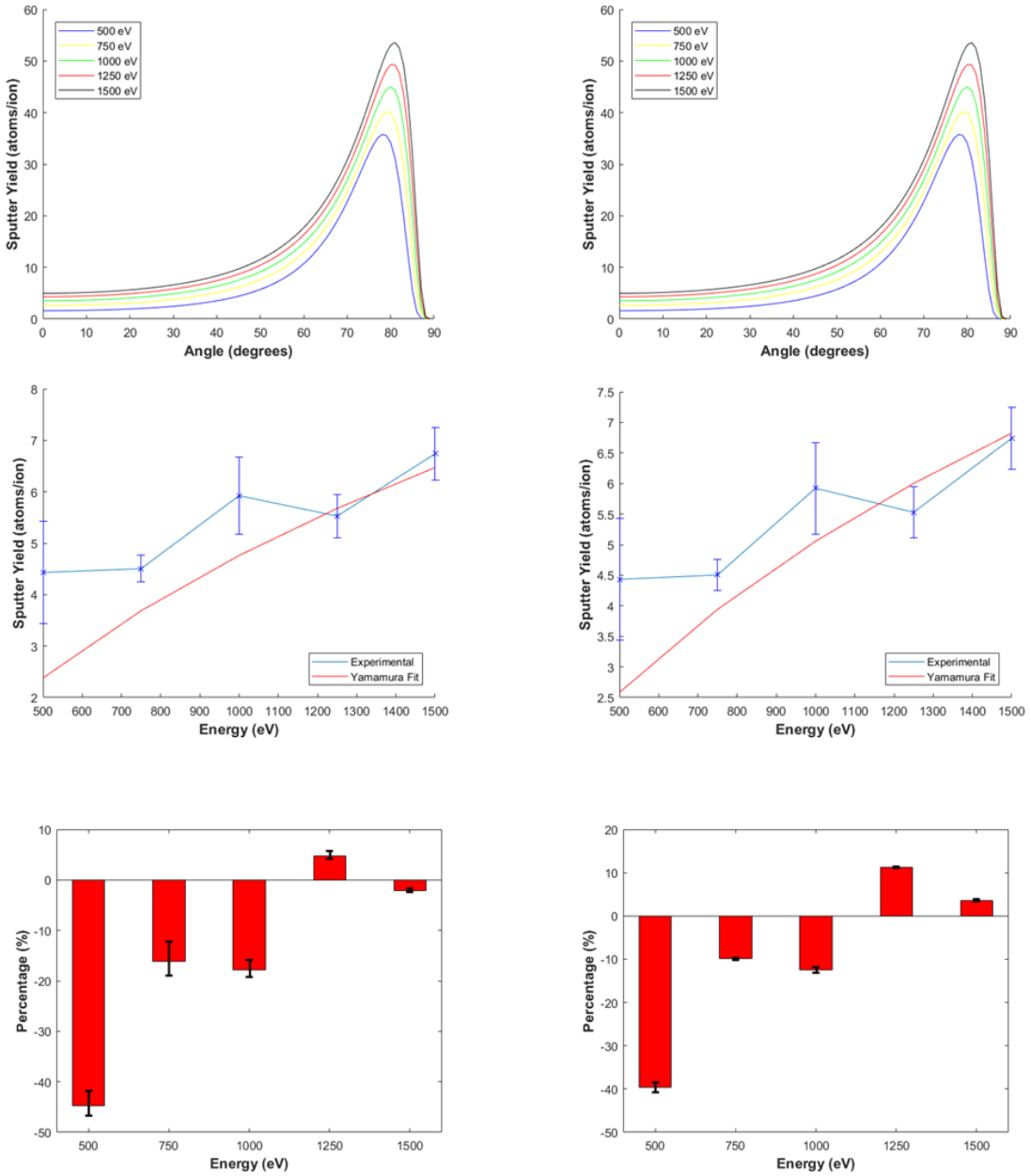

Fig. 96: Comparisons between f_{sig}=1.25 (left) and f_{sig}=1.5 (right), 30°

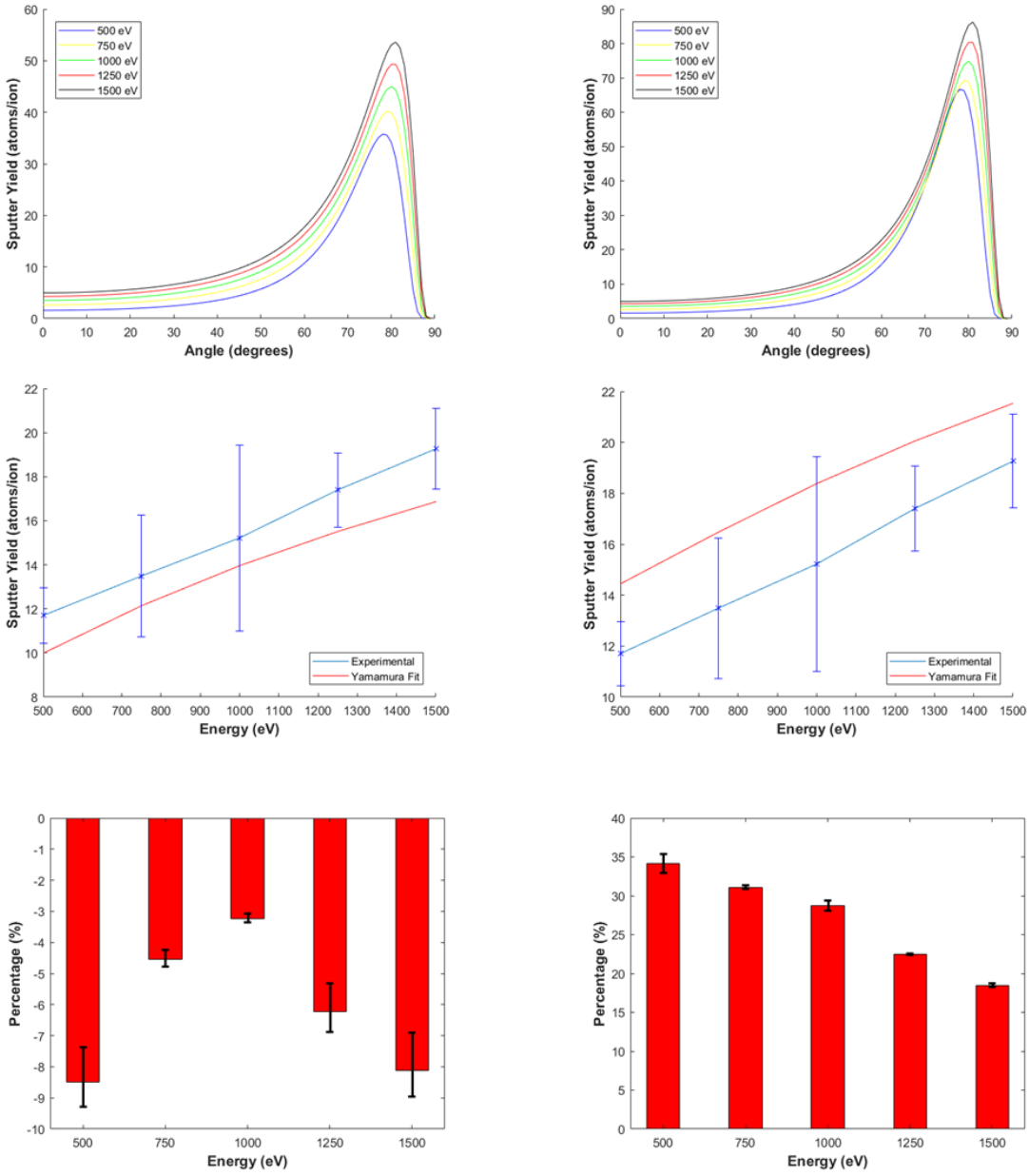

Fig. 97: Comparisons between f_{sig}=1.25 (left) and f_{sig}=1.5 (right), 60°

As shown in the preceding figures, the changing of f_{sig} has a more dramatic effect on the higher incidence angles, as it translates the curve fit (within an incidence angle) vertically along the sputter yield axis. However, the effect on the 30° incidence is very minimal. The changing of f_{sig} is also insufficient to change the slope of the fit in this location, as well.

Appendix C: Previous Test Results

This section contains the previous analysis that was seen in Chapters 10.3 through 10.5. There was a previous issue with the set of magnetic field equations (Equation 4-12) in which they were divided by 4π and resulted in a reduced strength magnetic field. Therefore, the magnetic braking effect that we see after the β transition point is much less pronounced, resulting in a higher potential for erosion. The appropriate figures below are similar to the official figures from the aforementioned sections of this work, but with the magnetic field reductions in place. It is noteworthy to mention that, despite the error with the magnetic field values, the results in GEO did not change at all, due to the relatively weak magnetic field strength in that region.

C.1. Test Case Results

As mentioned in Chapter 10.2, the leader-follower formation from the effort by Roberts[2] was utilized to test the accuracy of the simulation efforts for this work. According to Roberts, the C-TOS leader-follower formation experienced particle impacts to the spacecraft for approximately 16-18 minutes during its one orbital maneuver within one portion of the orbit according to Fig. 98. It is also noteworthy to indicate that they expect the CEX impingement to have a higher flux of particles to the follower than from direct impingement itself, yet will contribute very little to erosion.

Table 39: C-TOS Leader-Follower Parameters [2]

Altitude	1100 km
Inclination	63.4°
ISD	500 m

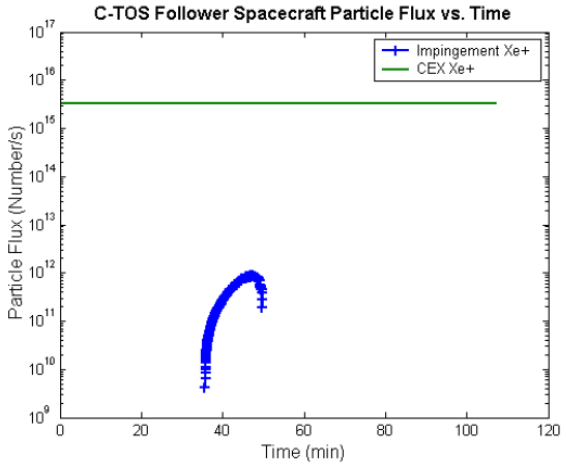

Fig. 98: C-TOS Impingement Flux [2]

The simulation from this effort indicates that the exposure time seen by the follower is 17.53 minutes, which is within the expected tolerance of the erosion time. Yet, while the simulation agrees with the timetable set by previous work on this formation, the simulation indicates that the exposure takes place throughout multiple sections of the orbit, as shown in Fig. 99. The simulation shows that although the erosion times are split into three different events throughout the orbit, this is also due to the regions in which there are sufficient β values that allow for direct plume exposure. All other sections of the orbit show no direct exposure at 500 m.

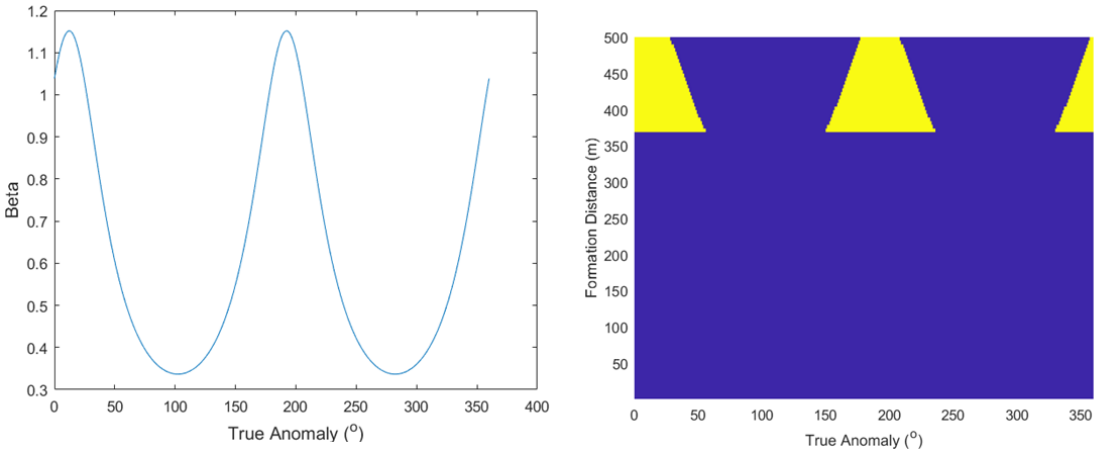

Fig. 99: C-TOS Test Case: Beta at 500 m (left), Hit Graph (right)

From here, the results from our simulation show a linear erosion trend, as demonstrated in Section 3.2.5. The data shows minor erosion of both the aluminum

structure as well as the AR coatings on the panels in the best case scenarios. For the worst case scenarios for MgF_2, the AR coating has the potential to lose ~16-45% of its thickness when exposed to the plume at a 60˚ incidence, with respect to the 500-1500 eV energy range. According to Yalin[52], even a 15% dosage will affect the transmission properties significantly, which will translate to a significant loss of power. A similar effect should be expected for the ITO coatings, as well, which bear even higher sputter yields than the MgF_2. Even with normal incidence exposure, the ITO still completely erodes away after one orbit with a 1500 eV beam; the other cases will expect to see significant power drops, as well. The worst-case exposures also show total failure above 500 eV for one orbit.

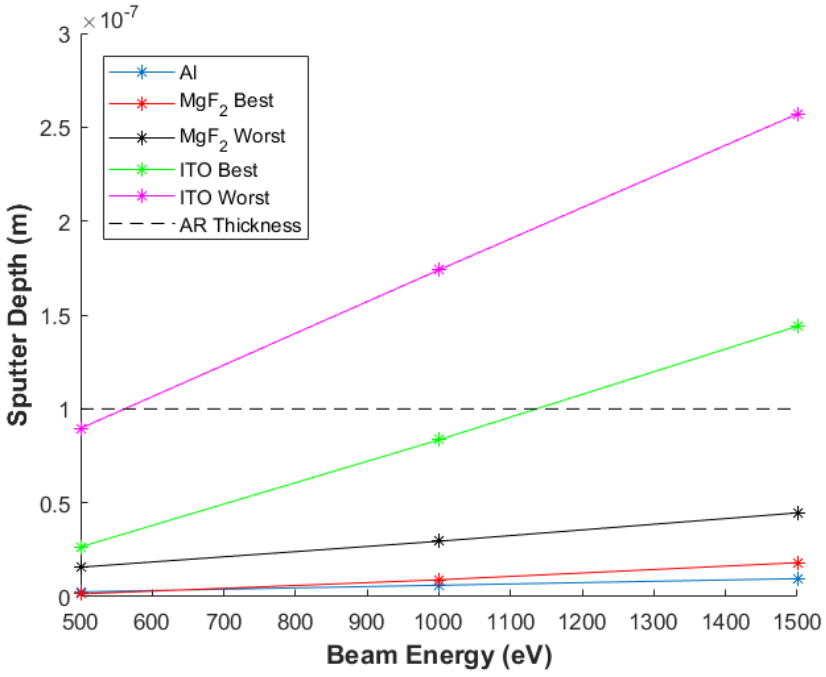

Fig. 100: C-TOS Test Case Sputter Depths

C.2. LEO Case Study

Low Earth Orbit (LEO) is home to many Earth observation missions, and as such, could become a focal point for formation flight missions of all types in the near future. To this end, a comprehensive study was performed for a range of orbital inclinations as well as ISD's, as shown in Table 12. The orbital altitude chosen (400 km) coincides with the International Space Station (ISS). This section will work to summarize the results of the case study, with the majority of the data available in Appendix A.3. LEO Erosion Study Datasets. For reference, unless otherwise noted, the plume density used for these observations is $1.47 \text{x} 10^{18}$ #/m^3.

C.2.1. Plume Exposure Observations

Because of the unique geomagnetic field environment, we are able to examine multiple trends within LEO: the changes in exposure due to the change in ISD and the changes in the exposure due to the change in orbital inclination. At first, the changes in exposure because of inclination change would be non-obvious; however, as mentioned above, the geomagnetic field environment in LEO is stronger than the other test altitudes. As the geomagnetic field model indicates, the field will increase significantly with respect to the orbital inclination, as shown in Fig. 89. As the orbital inclination increases, the gradient of the field strength increases as the peaks of the field increase significantly and the valleys of the field reduce in strength, as well.

For the most part, the exposure properties of the plume tend to remain the same until 45° inclination. The close-range ISD's show total exposure until a transition occurs between 250 and 500 m. After this, the exposure time drops off sharply in this transition

regime until 500 m, where there is no observed interaction from the ion plume for the remaining ISD's.

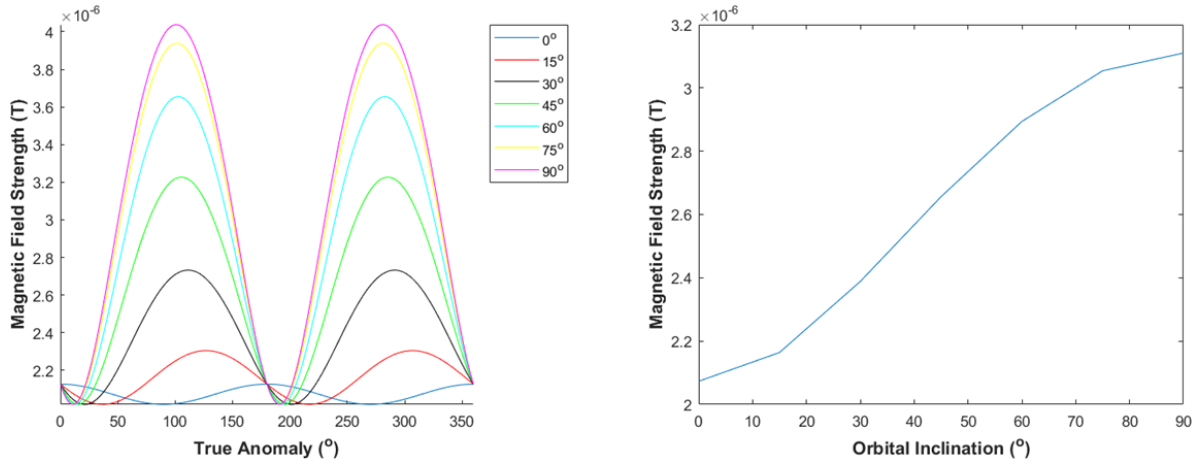

Fig. 89: LEO Geomagnetic Field Environment

As the orbital inclination increases, the transition point from full exposure to reduced exposure on orbit begins to shift closer to the spacecraft. This trend is expected due to the increasing magnetic field strength, as shown in Fig. 90. These changes in the magnetic field start to affect the plume interaction significantly by decreasing the exposure time at the intermediate ISD's, as well. However, at the higher inclinations, the ISD's which formerly showed no interaction

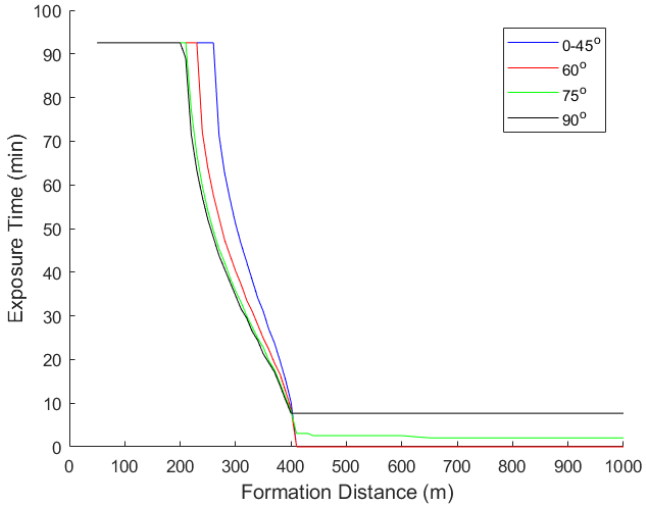

Fig. 90: Exposure Time Trends with respect to Orbital Inclination

with the spacecraft show very small, but quantifiable exposure times with the spacecraft. These occur in very small regions of the orbit where the magnetic field is weakest. This indicates that at higher orbital inclinations, the follower spacecraft is still vulnerable to plume impingement. These effects can be observed in Fig. 90. These regions, according to the simulation, also indicate varying degrees of energy loss of the plume, which will be discussed in a later section.

Another observation is the variance in density with respect to the exposure properties of the plume. As Equation 2-5 would suggest, the plasma density is directly proportional to β and, as such, plays an important role in determining the interaction properties of the plume to the follower spacecraft. This is verified by looking at the impact of plume density on the exposure times at a single orbital inclination, as shown in Fig. 103. As expected, the transition point from complete exposure to partial exposure begins to shift farther away from the leader spacecraft at higher plume densities.

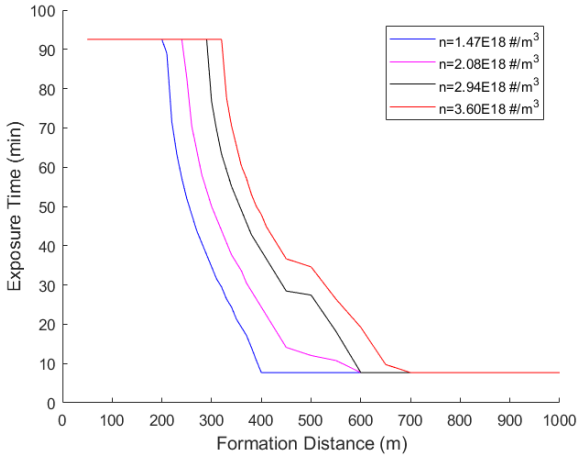

Fig. 103: Exposure Trends with respect to Plume Density, i=90°

It is worth noting that the BHT-HD-600, which served as the basis for the assumed plume density, is a 600 W Hall thruster designed for only 36 mN of thrust[65].

As shown, just increasing the density by a factor of 2.5 extended the full exposure transition point by 120 m (60%). Therefore, it would stand to reason that high thrust EP systems would pose a much higher risk for close formation spaceflight missions, which is a reasonable expectation due to higher plume densities. This trend is also in agreement with the β modelling trends, as shown in Section 4.2.1.

C.2.2. LEO Erosion Results

With the plume interaction properties of LEO determined, we must look at the actual erosion characteristics from these orbital conditions. As expected, the trend of the erosion depths coincide with the trends described above, showing an increasing linear trend with respect to both energy and time exposed; likewise, at higher ISD's, the follower spacecraft experiences less erosion due to the quadratic drop in plume density. For a majority of the observed orbital conditions, this general trending holds up fairly well. However, as mentioned above, at the higher orbital inclinations, specifically 75˚ and 90˚, the orbital conditions allow for small windows of plume interaction that result in surface erosion on the follower spacecraft.

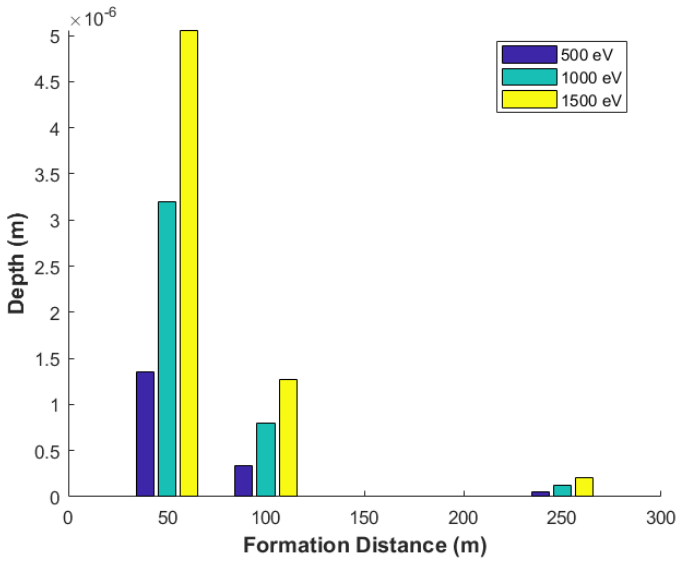

Fig. 104: LEO Sputter Data, i=0˚-45˚

As for the levels of erosion themselves, most cases show generally light erosion of aluminum, with the maximum erosion occurring at a beam energy of 1500 eV and ISD

of 50 m for all LEO orbital conditions, with a depth of approximately 5 µm based on the structural cross-section mentioned in Section 10.2.1. It is important to note that a layer of BoPET is 4.5 µm thick, so erosion of this level would compromise one layer of the BoPET sheath of a spacecraft. This erosion depth is also representative of one complete orbit with constant thrust.

Likewise, the AR coatings of the solar cells, in most of both the best and worst-cast scenarios, show significant amounts of erosion ranging from 102 to 104 nm. This, according to Yalin[52], would significantly affect the transmission properties of the coating, thereby experiencing a significant drop in power to the solar cells. And, as expected from earlier chapters, MgF_2 is significantly more resistant to plasma erosion than ITO in all cases, as the erosion is practically an order of magnitude higher in all cases when exposed to the same flux levels. Represented in Fig. 80 below shows the representative trends of the AR sputtering.

The remainder of the sputter data covering all scenarios can be located in Appendix A.3. LEO Erosion Study Datasets.

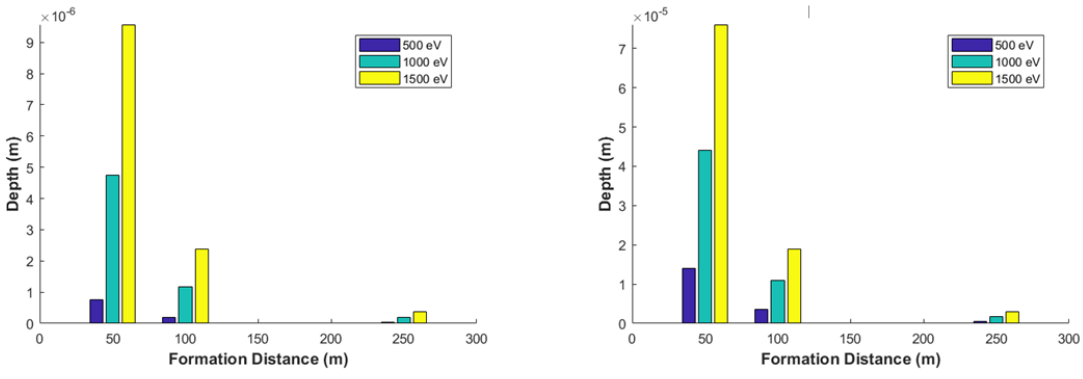

Fig. 105: LEO AR Sputter Data, Best Case i=0°-45°

C.3. Sun-Synchronous Erosion Results

Sun-Synchronous orbits are a unique case within this study due to the fact that, unlike the other two orbital conditions, this type of orbit always has the solar panels locked in a 90˚ incidence, where sputter of the AR coating is not possible. It is also unique due to the significant variation of the magnetic field for this set of orbital conditions. While there are many Sun-Sync orbits that can be observed, this particular orbit observed belongs to the A-Train[68] constellation, which has many satellites in leader-follower formations, but at distances much larger than those observed in this study.

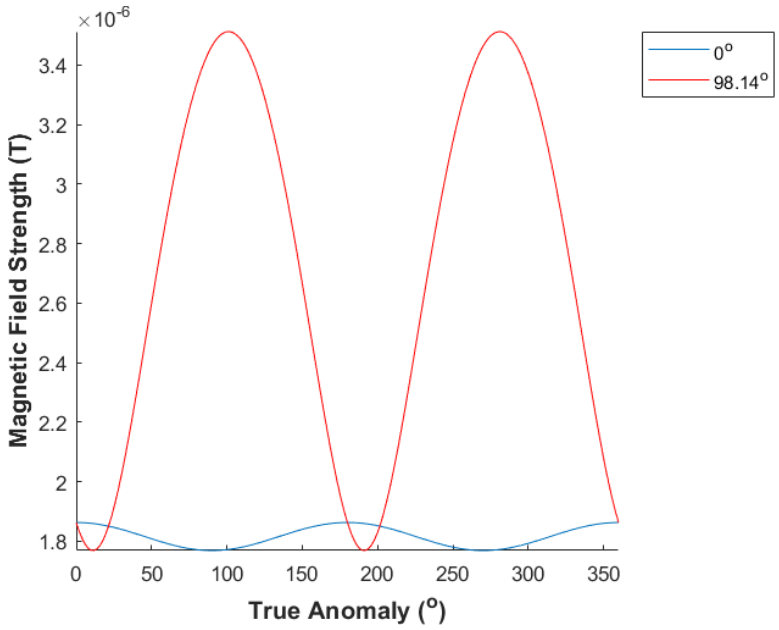

Fig. 106: Sun-Sync Geomagnetic Environment

As shown with the LEO study, the magnetic field oscillation does increase proportionally to the orbital inclination. As such, due to these high oscillations, there are small pockets of exposure at higher ISD's that also show energy loss at these locations. Overall, the erosion environment is similar to the environment found in LEO at 90˚

inclination. The sputter depth levels are also very similar, but due to being in a higher orbit than from the LEO study, the orbital period is slightly longer, resulting in slightly higher levels of erosion. The sputter depths displayed show the expected quadratic fall in sputter depth as the flux falls due to the distance from the beam exit, as shown in Fig. 82.

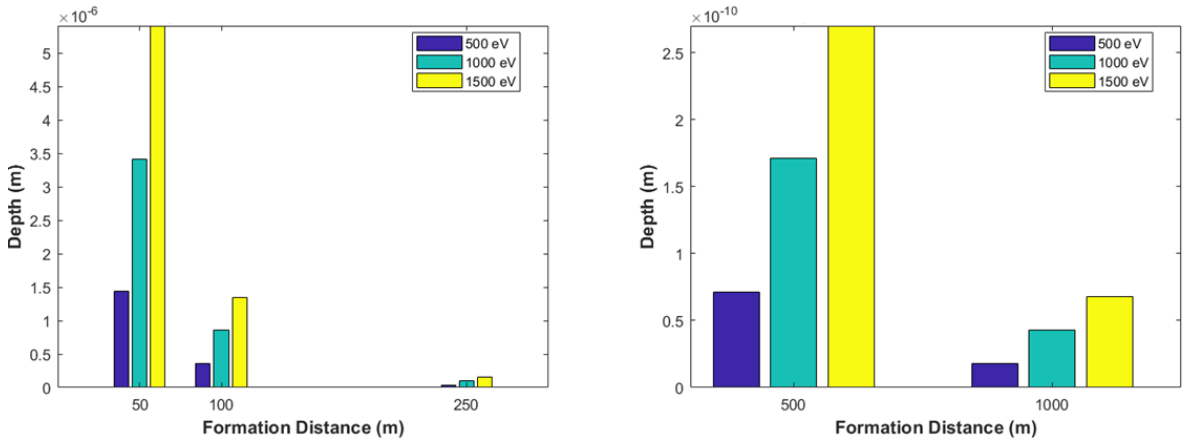

Fig. 107: Sun-Sync Sputter Depth Data

C.4. Previous LEO Erosion Study Datasets

Table 40: LEO (400 km altitude) @ i=0°-45°, Aluminum

ISD (m)	Energy (eV)	Time (min)	Flux ($^{\#}/_{m^2\text{-}s}$)	Depth (m)	Energy Loss? (Y/N)
50	500	92.5576	1.59E+19	1.35E-06	N
	1000	92.5576	2.25E+19	3.20E-06	N
	1500	92.5576	2.76E+19	5.06E-06	N
100	500	92.5576	3.98E+18	3.37E-07	N
	1000	92.5576	5.63E+18	8.01E-07	N
	1500	92.5576	6.90E+18	1.27E-06	N
250	500	92.5576	6.37E+17	5.39E-08	N
	1000	92.5576	9.01E+17	1.28E-07	N
	1500	92.5576	1.10E+18	2.02E-07	N
500	500	0	0	0	N
	1000	0	0	0	N
	1500	0	0	0	N
1000	500	0	0	0	N
	1000	0	0	0	N
	1500	0	0	0	N

Table 41: LEO (400 km altitude) @ i=0°-45°, MgF2, Best Case Scenario

ISD (m)	Energy (eV)	Time (min)	Flux ($^{\#}/_{m^2\text{-}s}$)	Depth (m)	Energy Loss? (Y/N)
50	500	92.5576	1.59E+19	7.60E-07	N
	1000	92.5576	2.25E+19	4.74E-06	N
	1500	92.5576	2.76E+19	9.57E-06	N
100	500	92.5576	3.98E+18	1.90E-07	N
	1000	92.5576	5.63E+18	1.18E-06	N
	1500	92.5576	6.90E+18	2.39E-06	N
250	500	92.5576	6.37E+17	3.04E-08	N
	1000	92.5576	9.01E+17	1.90E-07	N
	1500	92.5576	1.10E+18	3.83E-07	N
500	500	0	0	0	N
	1000	0	0	0	N
	1500	0	0	0	N
1000	500	0	0	0	N
	1000	0	0	0	N
	1500	0	0	0	N

Table 42: LEO (400 km altitude) @ i=0°-45°, MgF2, Worst Case Scenario

ISD (m)	Energy (eV)	Time (min)	Flux ($^{\#}/_{m^2\text{-}s}$)	Depth (m)	Energy Loss? (Y/N)
50	500	92.5576	1.59E+19	8.28E-06	N
	1000	92.5576	2.25E+19	1.56E-05	N
	1500	92.5576	2.76E+19	2.36E-05	N
100	500	92.5576	3.98E+18	2.07E-06	N
	1000	92.5576	5.63E+18	3.89E-06	N
	1500	92.5576	6.90E+18	5.89E-06	N
250	500	92.5576	6.37E+17	3.31E-07	N
	1000	92.5576	9.01E+17	6.22E-07	N
	1500	92.5576	1.10E+18	9.42E-07	N
500	500	0	0	0	N
	1000	0	0	0	N
	1500	0	0	0	N
1000	500	0	0	0	N
	1000	0	0	0	N
	1500	0	0	0	N

Table 43: LEO (400 km altitude) @ i=0°-45°, ITO, Best Case Scenario

ISD (m)	Energy (eV)	Time (min)	Flux ($^{\#}/_{m^2\text{-}s}$)	Depth (m)	Energy Loss? (Y/N)
50	500	92.5576	1.59E+19	1.40E-05	N
	1000	92.5576	2.25E+19	4.41E-05	N
	1500	92.5576	2.76E+19	7.61E-05	N
100	500	92.5576	3.98E+18	3.49E-06	N
	1000	92.5576	5.63E+18	1.10E-05	N
	1500	92.5576	6.90E+18	1.90E-05	N
250	500	92.5576	6.37E+17	5.59E-07	N
	1000	92.5576	9.01E+17	1.76E-06	N
	1500	92.5576	1.10E+18	3.04E-06	N
500	500	0	0	0	N
	1000	0	0	0	N
	1500	0	0	0	N
1000	500	0	0	0	N
	1000	0	0	0	N
	1500	0	0	0	N

Table 44: LEO (400 km altitude) @ i=0°-45°, ITO, Worst Case Scenario

ISD (m)	Energy (eV)	Time (min)	Flux ($^{\#}/_{m^2\text{-}s}$)	Depth (m)	Energy Loss? (Y/N)
50	500	92.5576	1.59E+19	4.73E-05	N
	1000	92.5576	2.25E+19	9.21E-05	N
	1500	92.5576	2.76E+19	1.35E-04	N
100	500	92.5576	3.98E+18	1.18E-05	N
	1000	92.5576	5.63E+18	2.30E-05	N
	1500	92.5576	6.90E+18	3.39E-05	N
250	500	92.5576	6.37E+17	1.89E-06	N
	1000	92.5576	9.01E+17	3.68E-06	N
	1500	92.5576	1.10E+18	5.42E-06	N
500	500	0	0	0	N
	1000	0	0	0	N
	1500	0	0	0	N
1000	500	0	0	0	N
	1000	0	0	0	N
	1500	0	0	0	N

Table 45: LEO (400 km altitude) @ i=60°, Aluminum

ISD (m)	Energy (eV)	Time (min)	Flux ($^{\#}/_{m^2\text{-}s}$)	Depth (m)	Energy Loss? (Y/N)
50	500	92.5576	1.59E+19	1.35E-06	N
	1000	92.5576	2.25E+19	3.20E-06	N
	1500	92.5576	2.76E+19	5.06E-06	N
100	500	92.5576	3.98E+18	3.37E-07	N
	1000	92.5576	5.63E+18	8.01E-07	N
	1500	92.5576	6.90E+18	1.27E-06	N
250	500	57.6883	6.37E+17	3.36E-08	N
	1000	57.6883	9.01E+17	7.99E-08	N
	1500	57.6883	1.10E+18	1.26E-07	N
500	500	0	0	0	N
	1000	0	0	0	N
	1500	0	0	0	N
1000	500	0	0	0	N
	1000	0	0	0	N
	1500	0	0	0	N

Table 46: LEO (400 km altitude) @ i=60°, MgF2, Best Case Scenario

ISD (m)	Energy (eV)	Time (min)	Flux ($^{\#}/_{m^2\text{-}s}$)	Depth (m)	Energy Loss? (Y/N)
50	500	92.5576	1.59E+19	7.60E-07	N
	1000	92.5576	2.25E+19	4.74E-06	N
	1500	92.5576	2.76E+19	9.57E-06	N
100	500	92.5576	3.98E+18	1.90E-07	N
	1000	92.5576	5.63E+18	1.18E-06	N
	1500	92.5576	6.90E+18	2.39E-06	N
250	500	57.6883	6.37E+17	1.89E-08	N
	1000	57.6883	9.01E+17	1.18E-07	N
	1500	57.6883	1.10E+18	2.39E-07	N
500	500	0	0	0	N
	1000	0	0	0	N
	1500	0	0	0	N
1000	500	0	0	0	N
	1000	0	0	0	N
	1500	0	0	0	N

Table 47: LEO (400 km altitude) @ i=60°, MgF2, Worst Case Scenario

ISD (m)	Energy (eV)	Time (min)	Flux ($^{\#}/_{m^2\text{-}s}$)	Depth (m)	Energy Loss? (Y/N)
50	500	92.5576	1.59E+19	8.28E-06	N
	1000	92.5576	2.25E+19	1.56E-05	N
	1500	92.5576	2.76E+19	2.36E-05	N
100	500	92.5576	3.98E+18	2.07E-06	N
	1000	92.5576	5.63E+18	3.89E-06	N
	1500	92.5576	6.90E+18	5.89E-06	N
250	500	57.6883	6.37E+17	2.06E-07	N
	1000	57.6883	9.01E+17	3.88E-07	N
	1500	57.6883	1.10E+18	5.87E-07	N
500	500	0	0	0	N
	1000	0	0	0	N
	1500	0	0	0	N
1000	500	0	0	0	N
	1000	0	0	0	N
	1500	0	0	0	N

Table 48: LEO (400 km altitude) @ i=60°, ITO, Best Case Scenario

ISD (m)	Energy (eV)	Time (min)	Flux ($^{\#}/_{m^2\text{-}s}$)	Depth (m)	Energy Loss? (Y/N)
50	500	92.5576	1.59E+19	1.40E-05	N
	1000	92.5576	2.25E+19	4.41E-05	N
	1500	92.5576	2.76E+19	7.61E-05	N
100	500	92.5576	3.98E+18	3.49E-06	N
	1000	92.5576	5.63E+18	1.10E-05	N
	1500	92.5576	6.90E+18	1.90E-05	N
250	500	57.6883	6.37E+17	3.48E-07	N
	1000	57.6883	9.01E+17	1.10E-06	N
	1500	57.6883	1.10E+18	1.90E-06	N
500	500	0	0	0	N
	1000	0	0	0	N
	1500	0	0	0	N
1000	500	0	0	0	N
	1000	0	0	0	N
	1500	0	0	0	N

Table 49: LEO (400 km altitude) @ i=60°, ITO, Worst Case Scenario

ISD (m)	Energy (eV)	Time (min)	Flux ($^{\#}/_{m^2\text{-}s}$)	Depth (m)	Energy Loss? (Y/N)
50	500	92.5576	1.59E+19	4.73E-05	N
	1000	92.5576	2.25E+19	9.21E-05	N
	1500	92.5576	2.76E+19	1.35E-04	N
100	500	92.5576	3.98E+18	1.18E-05	N
	1000	92.5576	5.63E+18	2.30E-05	N
	1500	92.5576	6.90E+18	3.39E-05	N
250	500	57.6883	6.37E+17	1.18E-06	N
	1000	57.6883	9.01E+17	2.30E-06	N
	1500	57.6883	1.10E+18	3.38E-06	N
500	500	0	0	0	N
	1000	0	0	0	N
	1500	0	0	0	N
1000	500	0	0	0	N
	1000	0	0	0	N
	1500	0	0	0	N

Table 50: LEO (400 km altitude) @ i=75°, Aluminum

ISD (m)	Energy (eV)	Time (min)	Flux ($^{\#}/_{m^2\text{-}s}$)	Depth (m)	Energy Loss? (Y/N)
50	500	92.5576	1.59E+19	1.35E-06	N
	1000	92.5576	2.25E+19	3.20E-06	N
	1500	92.5576	2.76E+19	5.06E-06	N
100	500	92.5576	3.98E+18	3.37E-07	N
	1000	92.5576	5.63E+18	8.01E-07	N
	1500	92.5576	6.90E+18	1.27E-06	N
250	500	49.4837	6.37E+17	2.88E-08	N
	1000	49.4837	9.01E+17	6.85E-08	N
	1500	49.4837	1.10E+18	1.08E-07	N
500	500	2.5639	4.26E+15	9.50E-12	Y
	1000	2.5639	6.03E+15	2.27E-11	Y
	1500	2.5639	7.38E+15	3.61E-11	Y
1000	500	2.0511	2.33E+15	4.11E-12	Y
	1000	2.0511	3.30E+15	9.89E-12	Y
	1500	2.0511	4.04E+15	1.57E-11	Y

Table 51: LEO (400 km altitude) @ i=75°, MgF2, Best Case Scenario

ISD (m)	Energy (eV)	Time (min)	Flux ($^{\#}/_{m^2\text{-}s}$)	Depth (m)	Energy Loss? (Y/N)
50	500	92.5576	1.59E+19	7.60E-07	N
	1000	92.5576	2.25E+19	4.74E-06	N
	1500	92.5576	2.76E+19	9.57E-06	N
100	500	92.5576	3.98E+18	1.90E-07	N
	1000	92.5576	5.63E+18	1.18E-06	N
	1500	92.5576	6.90E+18	2.39E-06	N
250	500	49.4837	6.37E+17	1.63E-08	N
	1000	49.4837	9.01E+17	1.01E-07	N
	1500	49.4837	1.10E+18	2.05E-07	N
500	500	2.5639	4.26E+15	4.48E-12	Y
	1000	2.5639	6.03E+15	3.17E-11	Y
	1500	2.5639	7.38E+15	6.60E-11	Y
1000	500	2.0511	2.33E+15	1.90E-12	Y
	1000	2.0511	3.30E+15	1.37E-11	Y
	1500	2.0511	4.04E+15	2.86E-11	Y

Table 52: LEO (400 km altitude) @ i=75°, MgF2, Worst Case Scenario

ISD (m)	Energy (eV)	Time (min)	Flux ($^{\#}/_{m^2\text{-}s}$)	Depth (m)	Energy Loss? (Y/N)
50	500	92.5576	1.59E+19	8.28E-06	N
	1000	92.5576	2.25E+19	1.56E-05	N
	1500	92.5576	2.76E+19	2.36E-05	N
100	500	92.5576	3.98E+18	2.07E-06	N
	1000	92.5576	5.63E+18	3.89E-06	N
	1500	92.5576	6.90E+18	5.89E-06	N
250	500	49.4837	6.37E+17	1.77E-07	N
	1000	49.4837	9.01E+17	3.33E-07	N
	1500	49.4837	1.10E+18	5.04E-07	N
500	500	2.5639	4.26E+15	6.24E-11	Y
	1000	2.5639	6.03E+15	1.11E-10	Y
	1500	2.5639	7.38E+15	1.69E-10	Y
1000	500	2.0511	2.33E+15	2.74E-11	Y
	1000	2.0511	3.30E+15	4.85E-11	Y
	1500	2.0511	4.04E+15	7.37E-11	Y

Table 53: LEO (400 km altitude) @ i=75°, ITO, Best Case Scenario

ISD (m)	Energy (eV)	Time (min)	Flux ($^{\#}/_{m^2\text{-}s}$)	Depth (m)	Energy Loss? (Y/N)
50	500	92.5576	1.59E+19	1.40E-05	N
	1000	92.5576	2.25E+19	4.41E-05	N
	1500	92.5576	2.76E+19	7.61E-05	N
100	500	92.5576	3.98E+18	3.49E-06	N
	1000	92.5576	5.63E+18	1.10E-05	N
	1500	92.5576	6.90E+18	1.90E-05	N
250	500	49.4837	6.37E+17	2.99E-07	N
	1000	49.4837	9.01E+17	9.43E-07	N
	1500	49.4837	1.10E+18	1.63E-06	N
500	500	2.5639	4.26E+15	9.38E-11	Y
	1000	2.5639	6.03E+15	3.07E-10	Y
	1500	2.5639	7.38E+15	5.36E-10	Y
1000	500	2.0511	2.33E+15	4.05E-11	Y
	1000	2.0511	3.30E+15	1.33E-10	Y
	1500	2.0511	4.04E+15	2.33E-10	Y

Table 54: LEO (400 km altitude) @ i=75°, ITO, Worst Case Scenario

ISD (m)	Energy (eV)	Time (min)	Flux ($^{\#}/_{m^2\text{-}s}$)	Depth (m)	Energy Loss? (Y/N)
50	500	92.5576	1.59E+19	4.73E-05	N
	1000	92.5576	2.25E+19	9.21E-05	N
	1500	92.5576	2.76E+19	1.35E-04	N
100	500	92.5576	3.98E+18	1.18E-05	N
	1000	92.5576	5.63E+18	2.30E-05	N
	1500	92.5576	6.90E+18	3.39E-05	N
250	500	49.4837	6.37E+17	1.01E-06	N
	1000	49.4837	9.01E+17	1.97E-06	N
	1500	49.4837	1.10E+18	2.90E-06	N
500	500	2.5639	4.26E+15	3.42E-10	Y
	1000	2.5639	6.03E+15	6.62E-10	Y
	1500	2.5639	7.38E+15	9.77E-10	Y
1000	500	2.0511	2.33E+15	1.49E-10	Y
	1000	2.0511	3.30E+15	2.89E-10	Y
	1500	2.0511	4.04E+15	4.26E-10	Y

Table 55: LEO (400 km altitude) @ i=90°, Aluminum

ISD (m)	Energy (eV)	Time (min)	Flux ($^{\#}/_{m^2\text{-}s}$)	Depth (m)	Energy Loss? (Y/N)
50	500	92.5576	1.59E+19	1.35E-06	N
	1000	92.5576	2.25E+19	3.20E-06	N
	1500	92.5576	2.76E+19	5.06E-06	N
100	500	92.5576	3.98E+18	3.37E-07	N
	1000	92.5576	5.63E+18	8.01E-07	N
	1500	92.5576	6.90E+18	1.27E-06	N
250	500	47.9453	6.37E+17	2.79E-08	N
	1000	47.9453	9.01E+17	6.64E-08	N
	1500	47.9453	1.10E+18	1.05E-07	N
500	500	7.6918	4.26E+15	9.06E-11	Y
	1000	7.6918	6.03E+15	2.16E-10	Y
	1500	7.6918	7.38E+15	3.42E-10	Y
1000	500	7.6918	2.33E+15	2.82E-11	Y
	1000	7.6918	3.30E+15	6.74E-11	Y
	1500	7.6918	4.04E+15	1.07E-10	Y

Table 56: LEO (400 km altitude) @ i=90°, MgF2, Best Case Scenario

ISD (m)	Energy (eV)	Time (min)	Flux ($^{\#}/_{m^2\text{-}s}$)	Depth (m)	Energy Loss? (Y/N)
50	500	92.5576	1.59E+19	7.60E-07	N
	1000	92.5576	2.25E+19	4.74E-06	N
	1500	92.5576	2.76E+19	9.57E-06	N
100	500	92.5576	3.98E+18	1.90E-07	N
	1000	92.5576	5.63E+18	1.18E-06	N
	1500	92.5576	6.90E+18	2.39E-06	N
250	500	47.9453	6.37E+17	1.57E-08	N
	1000	47.9453	9.01E+17	9.82E-08	N
	1500	47.9453	1.10E+18	1.98E-07	N
500	500	7.6918	4.26E+15	4.85E-11	Y
	1000	7.6918	6.03E+15	3.14E-10	Y
	1500	7.6918	7.38E+15	6.40E-10	Y
1000	500	7.6918	2.33E+15	1.46E-11	Y
	1000	7.6918	3.30E+15	9.69E-11	Y
	1500	7.6918	4.04E+15	1.99E-10	Y

Table 57: LEO (400 km altitude) @ i=90°, MgF2, Worst Case Scenario

ISD (m)	Energy (eV)	Time (min)	Flux ($^{\#}/_{m^2\text{-}s}$)	Depth (m)	Energy Loss? (Y/N)
50	500	92.5576	1.59E+19	8.28E-06	N
	1000	92.5576	2.25E+19	1.56E-05	N
	1500	92.5576	2.76E+19	2.36E-05	N
100	500	92.5576	3.98E+18	2.07E-06	N
	1000	92.5576	5.63E+18	3.89E-06	N
	1500	92.5576	6.90E+18	5.89E-06	N
250	500	47.9453	6.37E+17	1.71E-07	N
	1000	47.9453	9.01E+17	3.22E-07	N
	1500	47.9453	1.10E+18	4.88E-07	N
500	500	7.6918	4.26E+15	5.69E-10	Y
	1000	7.6918	6.03E+15	1.05E-09	Y
	1500	7.6918	7.38E+15	1.60E-09	Y
1000	500	7.6918	2.33E+15	1.80E-10	Y
	1000	7.6918	3.30E+15	3.29E-10	Y
	1500	7.6918	4.04E+15	4.99E-10	Y

Table 58: LEO (400 km altitude) @ i=90°, ITO, Best Case Scenario

ISD (m)	Energy (eV)	Time (min)	Flux ($^{\#}/_{m^2\text{-}s}$)	Depth (m)	Energy Loss? (Y/N)
50	500	92.5576	1.59E+19	1.40E-05	N
	1000	92.5576	2.25E+19	4.41E-05	N
	1500	92.5576	2.76E+19	7.61E-05	N
100	500	92.5576	3.98E+18	3.49E-06	N
	1000	92.5576	5.63E+18	1.10E-05	N
	1500	92.5576	6.90E+18	1.90E-05	N
250	500	47.9453	6.37E+17	2.90E-07	N
	1000	47.9453	9.01E+17	9.14E-07	N
	1500	47.9453	1.10E+18	1.58E-06	N
500	500	7.6918	4.26E+15	9.27E-10	Y
	1000	7.6918	6.03E+15	2.96E-09	Y
	1500	7.6918	7.38E+15	5.12E-09	Y
1000	500	7.6918	2.33E+15	2.86E-10	Y
	1000	7.6918	3.30E+15	9.19E-10	Y
	1500	7.6918	4.04E+15	1.60E-09	Y

Table 59: LEO (400 km altitude) @ i=90°, ITO, Worst Case Scenario

ISD (m)	Energy (eV)	Time (min)	Flux ($^{\#}/_{m^2\text{-}s}$)	Depth (m)	Energy Loss? (Y/N)
50	500	92.5576	1.59E+19	4.73E-05	N
	1000	92.5576	2.25E+19	9.21E-05	N
	1500	92.5576	2.76E+19	1.35E-04	N
100	500	92.5576	3.98E+18	1.18E-05	N
	1000	92.5576	5.63E+18	2.30E-05	N
	1500	92.5576	6.90E+18	3.39E-05	N
250	500	47.9453	6.37E+17	9.81E-07	N
	1000	47.9453	9.01E+17	1.91E-06	N
	1500	47.9453	1.10E+18	2.81E-06	N
500	500	7.6918	4.26E+15	3.21E-09	Y
	1000	7.6918	6.03E+15	6.24E-09	Y
	1500	7.6918	7.38E+15	9.19E-09	Y
1000	500	7.6918	2.33E+15	1.00E-09	Y
	1000	7.6918	3.30E+15	1.95E-09	Y
	1500	7.6918	4.04E+15	2.87E-09	Y

C.5. Previous Sun-Synchronous Erosion Study Dataset

Table 60: Sun-Sync (705 km altitude) @ i=98.14°, Aluminum

ISD (m)	Energy (eV)	Time (min)	Flux ($^{\#}/_{m^2\text{-}s}$)	Depth (m)	Energy Loss? (Y/N)
50	500	98.8748	1.59E+19	1.44E-06	N
	1000	98.8748	2.25E+19	3.42E-06	N
	1500	98.8748	2.76E+19	5.41E-06	N
100	500	98.8748	3.98E+18	3.60E-07	N
	1000	98.8748	5.63E+18	8.55E-07	N
	1500	98.8748	6.90E+18	1.35E-06	N
250	500	68.7467	6.37E+17	4.01E-08	N
	1000	68.7467	9.01E+17	9.52E-08	N
	1500	68.7467	1.10E+18	1.50E-07	N
500	500	7.1212	1.13E+16	7.14E-11	Y
	1000	7.1212	1.59E+16	1.71E-10	Y
	1500	7.1212	1.95E+16	2.70E-10	Y
1000	500	7.1212	2.82E+15	1.78E-11	Y
	1000	7.1212	3.98E+15	4.27E-11	Y
	1500	7.1212	4.88E+15	6.76E-11	Y

Appendix D: Impurity Flux Assessment

As mentioned in Section 6.2, the vacuum environment for the sputter experiments carries a high chance for a phenomenon called *target poisoning*, a type of material interference from impurity flux to the samples within high vacuum environments. As described by Güttler, the concept of impurity flux comes directly from neutral bombardment to the sample[70]. This bombardment would take place at the thermal velocity of the gas, as shown in Equation D-1. This thermal velocity can then be used to calculate the impurity flux based on the density of particles, as demonstrated in Equation D-2.

$$v_{th,n} = \sqrt{\frac{8k_B T}{\pi m_n}} \tag{D-1}$$

$$\Gamma_n = \frac{1}{4} n_n v_{th,n} \tag{D-2}$$

Impurity flux can also be calculated using the partial pressure of the neutral gas, as shown in Equation D-3 and Equation D-4.

$$P_n = n_n k_B T \tag{D-3}$$

$$\Gamma_n = \frac{P_n}{\sqrt{2\pi k_B T m_n}} \tag{D-4}$$

Once the impurity flux is known, we can then calculate the probability that the target will be poisoned. This is conducted through use of the sticking coefficient, *S*. As described by Güttler, this sticking coefficient is a function of temperature, surface roughness and θ, the surface compound fraction, and is bound between 0 and 1. Once *S* is known, we can then proceed to find the amount of particles that adhere, or *adsorb*, to the surface. These parameters are represented by Equation D-5 and Equation D-6, respectively. It is important to note that this process usually only builds one monolayer of material on the surface if it completely adsorbs.

$$N_{adsorb} = \Gamma_n S \tag{D-5}$$

$$S = S_0 \left(1 + k\frac{\theta}{1-\theta}\right)^{-1} \tag{D-6}$$

However, it is important to note that an analysis by Wanlass notes that *S* is inversely proportional to the temperature of the local environment[71]. This work shows two separate experiments analyzing the sticking coefficients of nitrogen on tungsten from Ehrlich (A) and Kisliuk (B). Both researchers noted the temperature dependence of the coefficients. This data is shown in Fig. 108. Wanlass also noted that the data from Kisliuk could be fit onto the Ehrlich data with the

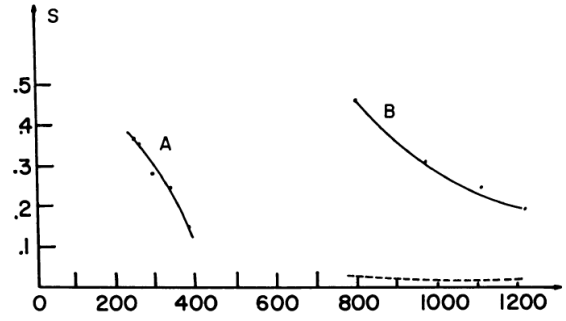

Fig. 108: Sticking Coefficient Data for Nitrogen Adsorption on Tungsten [71]

use of a scale factor, shown in Fig. 108 as the dashed line.

For the experiments performed within this work, the standard operating pressure was 0.2-0.4 mTorr, or 2.7-5.3x10^{-2} Pa, respectively. This is also taking into account the flow of xenon gas through the chamber. Without the xenon flow to consider, the background pressure of the vacuum chamber alone is 0.18 mTorr. This represents a possible impurity flux of ~10^{20} #/m^2-s from neutrals such as nitrogen (N_2) and oxygen (O_2). A representative ion flux to the sample at 500 eV would be ~10^{19} #/m^2-s, which would state that the impurity flux is an order of magnitude higher than the ion flux.

However, it is important to recall the discussion from above with regards to sticking coefficient and temperature effects on the sample. As noted in Section 7.4, the surface temperature for the majority of the samples was sufficiently increased due to the power input to the sample from the beam and the lack of active cooling to the sample throughout the experiment. Because of the direct impingement of the beam, the power input to the sample is represented by the product of the current to the exposed area and the kinetic energy of the beam, as represented in Equation D-7. This, in turn, can be equated to blackbody radiation expression for power, shown in Equation D-8, in order to find the temperature of the surface.

$$P = I\varphi \tag{D-7}$$

$$P = \varepsilon\sigma A T^4 \tag{D-8}$$

From these equations, we can determine that even at the lowest energies for this effort, the temperature on the sample would at least be 400 K, a region where the sticking

coefficient would be assumed to be low, depending on the reaction. Also, due to the Al calibration experiments at 1200 eV, the difference between the data point from this work and the Tartz data is relatively low, considering the Tartz experiment was performed in a vacuum chamber with ~10^{-8} mbar pressure before Xe flow; with Xe flow, this would become a $3.75x10^{-5}$ Torr ($5x10^{-5}$ mbar) vacuum environment[37].

Another factor to note is that, because of the temperature of the sample and its surroundings, if any particles did adsorb and combine with any of the surface atoms, most of the byproducts would melt immediately due to their reduced melting temperatures as laid out by the Clausius-Clapeyron relation (Equation 7-1), such as Indium Oxide.

Lastly, experiments performed using the SPPL-1 also showed very little in the form of target poisoning due to EDS scans taken from the exposed areas of the Al 6061-T4 samples[60]. These EDS scans indicated that, although there was oxygen presented inside the scanned areas, these particles were present in the alloyed sample and actually decreased in concentration in the exposed areas versus the unexposed areas of the surface. Therefore, it is reasonable to assume that, despite the impurity flux to the sample, due to a low sticking coefficient, the flux has a minimal effect on the sputter results presented in this work.

Appendix E: SPPL-1 Ion Source

E.1. Introduction

At the early phase of this experimental effort, it was decided to create an ion source that could perform the early erosion experiments to gather preliminary data for this work. To this end, it was decided to create a lab-model ion engine in order to sputter Al 6061-T4 samples with an Argon ion beam. This ion engine would be a representative case of the beam plumes that could be seen in orbit. It would also serve as a teaching tool for several undergraduate lab courses that were just being introduced to plasma thrusters. As a result, this would become, to the author's knowledge, the first ion engine with a transparent discharge chamber in order to visually observe the plasma that is formed within.

E.2. Structural Components

In order to visually inspect the plasma, the frame had to allow for visualization of the discharge chamber. The discharge chamber itself, was made out of a custom-cut quartz tube by Scientific Glass International with a 9 cm inner diameter. The anode, which would also have to be as transparent as possible, was made out of standard metallic mesh that could withstand the temperatures expected from the plasma and the emitter cathode. The frame surrounding the discharge chamber includes the retainer ring and the cathode cap flanking both sides of the tube, the

Fig. 109: SPPL-1 Frame

magnet frame, and the neutralizer pod (which attaches at the top of the magnet frame). The cathode cap contained multiple orifices for the emission cathode (to be supported by tungsten rods to conduct power and allow for cooling of the cathode), the propellant gas feed (a pressure orifice with a 10.5 μm hole for choked flow control) created by Lenox Laser, Inc., and for a Langmuir probe to conduct plasma diagnostics of the discharge chamber. The entirety of the frame, which includes supports for the SPPL-1 to directly connect to the vacuum chamber, is made of stainless steel. The magnet frame would become home to three R1410 ring magnets with an inner diameter of 10 cm, each with a maximum magnetic strength of 0.49 T at the edges of the magnet. The frame was designed by the author and constructed by Ed Cole of the Institute for Physical Sciences and Technology.

E.3. Internal Components

In order to create the ion beam required for the experiments, the following components would be required: 1) ion optics, 2) electron sources, and 3) appropriate power sources. This section will give a brief overview of these components.

E.3.1. Ion Optics

As mentioned in Section 1.1.2, the ion optics allow for the focusing of the ions from the discharge chamber into beamlets that then accelerate the ions to create thrust. Normally, these are grids with thousands of holes to create these

Fig. 110: SPPL-1 Optics Grids w/Alumina spacers

beamlets to maximize ion transparency, but minimize neutral transparency to increase efficiency. However, due to the current levels that were required for the experiment, each grid only required ~280 holes per grid, each appropriately sized to maximize beamlet efficiency. These grids were also made of stainless steel and created by Lenox Laser, Inc. In order to separate the grids from each other, alumina spacers were custom-made by Kadco Ceramics to insulate each of the grids from each other as well as the anode inside the discharge chamber. The spacing between each of the grids is 2 mm.

E.3.2. Electron Sources

In order to provide the primary electrons for ionization, an emission cathode would be required. To this end, a thermionic filament was to be utilized. Although hollow cathodes are vastly more efficient, a thermionic filament was used due to ease of maintenance and cost. At first, tantalum filaments were used for electron sources. This was due to the increased potential for electron emission based on the material's work function φ, or the minimum energy required to liberate free electrons from a transition metal. This effect is mapped by the Richardson equation for current density (shown in Equation E-1), a basemark equation for thermionic emission. However, while these were successful, they were less robust than the standard tungsten filaments. The tradeoff for the reduced electron emission from the higher work function of tungsten metal is the increased melting temperature of the material, which allows for longer durations of use.

$$J = AT^2 e^{-kT/e\varphi} \tag{E-1}$$

E.3.3. Power System Description

To generate the ion beam from this type of electrostatic thruster, multiple power sources are required in order to generate the beam. Power sources for the following components are needed: the anode, emission cathode, the neutralizer cathode, the screen grid, the accelerator grid, and a discharge power supply to handle the electron pumping for the ionization process. These power supplies would also have to be held relative to the

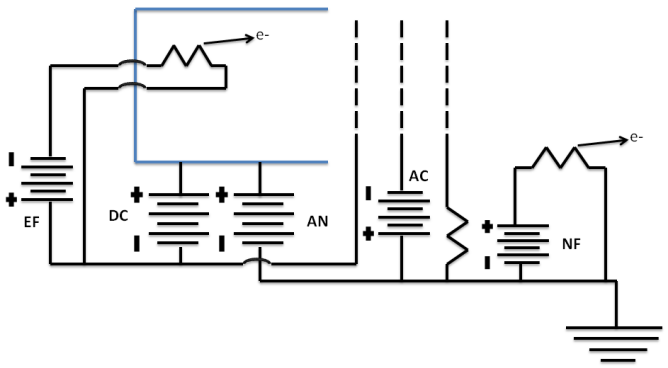

Fig. 111: Electrical Diagram for SPPL-1 [60]

Table 61: Electrical Components for SPPL-1 [60]

Component	Power Supply
Emitter Filament (EF)	Acopian A015HX1000M
Discharge Supply (DC)	Acopian A0100MX25
Anode (AN)	Acopian A0150NX05
Accelerator Grid (AC)	Acopian N01HA30
Neutralizer Filament (NF)	Mastech TP3020-D

anode potential, as well. A schematic of the power system as well as a listing of all appropriate power supplies are listed below.

E.4. Conclusion

Although the SPPL-1 ion source was not utilized for the experiments presented in this work, the ion source was used to carry out material experiments which are outlined in

the author's previous work[60]. The ion source also contributed to an ion beam modelling effort as a part of the AFOSR research grant for this project, as well[72]. The ion source successfully created ion beams up to 350 eV with Ar propellant. The source was to be retrofitted to perform at higher energies, but the Tectra ion source became available and the refit of the source was halted.

Fig. 112: SPPL-1 First Plasma Ignition

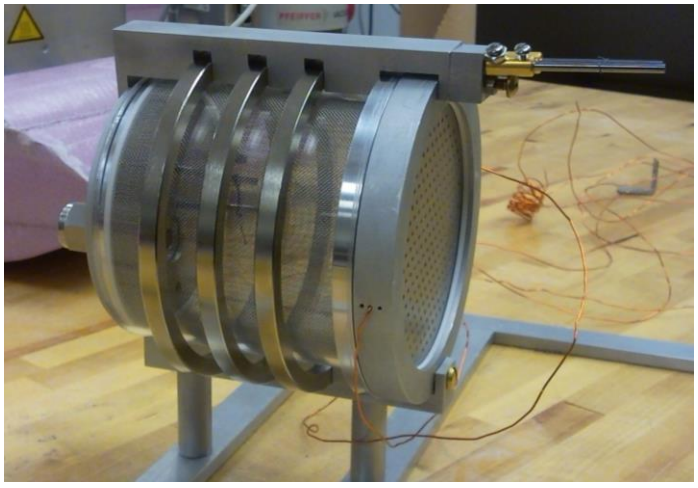

Fig. 113: SPPL-1

Bibliography (Covers Sources used from Chapters 1 and 2)

[1] Sutton, G. and Biblarz, O., *Rocket Propulsion Elements, 7th Edition*, John Wiley & Sons, 2001

[2] Roberts, C. and Hastings, D., "Electric Thruster Impingement Effects on Multiple Spacecraft System Environments," *38th AIAA/ASME/SAE/ASEE Joint Propulsion Conference & Exhibit*, AIAA 2002-3670, Indianapolis, IN, 7-10 July 2002

[3] Goebel, D.M. and I. Katz, *Fundamentals of Electric Propulsion: Ion and Hall Thusters*, John Wiley & Sons, 2008

[4] Jahn, R., *Physics of Electric Propulsion*, McGraw-Hill, Inc., 1968

[5] Wang, J., et al., "Deep Space One Investigations of Ion Propulsion Plasma Environment," *Journal of Spacecraft and Rockets*, Vol. 37, No. 5, Sep-Oct 2000, pp. 545-555

[6] Brophy, J., et al., "The Ion Propulsion System For Dawn," AIAA-2003-4542

[7] Kaufmann, H., "Electrostatic Thrustors," NASA N65-21470

[8] Detleff, G., "Plume Flow and Plume Impingement in Space Technology," *Prog. Aerospace Science*, Vol. 28, pp. 1-71, 1991

[9] Jianhua, Z., et al., "Numerical and Experimental Study of Plume Impingement Effects," *57th International Astronautical Congress 2006*, IAC-06-C4.P.1.8

[10] Pfaff, R., "The Near-Earth Plasma Environment," *Space Science Review*, Number 168, 2012, pp. 23-112

[11] Levin, D., et al., "Tightly Coupled Mechanistic Study of Materials in the Extreme Space Environment," *AFOSR Program Review on Materials and Processes Far from Equilibrium*, Cleveland, OH, Nov. 29-30, 2011

[12] Behrish, R. and Eckstein, W., *Sputtering by Particle Bombardment*, Springer, 2007

[13] Tartz, M., Hartmann, E., Deltschew, R., and Neumann, H., "Grid Erosion Study of a Three-Grid Ion Thruster," *34th AIAA/ASME/SAE/ASEE Joint Propulsion Conference & Exhibit*, AIAA 1998-3646, Cleveland, OH, 13-15 July 1998

[14] Brophy, J., Katz, I., Polk, J., and Anderson, J., "Numerical Simulations of Ion Thruster Grid Erosion," AIAA-2002-4261

[15] Wirz, R., Anderson, J., Katz, I., and Goebel, D., "Time-Dependent Erosion of Ion Optics," *44th AIAA/ASME/SAE/ASEE Joint Propulsion Conference and Exhibit*, AIAA 2008-4529, Hartford, CT, 21-23 July 2008

[16] Tartz, M. and Neumann, H., "Validated Ion Thruster Grid Lifetime Simulation," *42nd AIAA/ASME/SAE/ASEE Joint Propulsion Conference & Exhibit*, AIAA 2006-5022, Sacramento, CA, 9-12 July 2006

[17] Polk, J.E., et al., "An Overview of the Results from an 8200 Hour Wear Test of the NSTAR Ion Thruster," AIAA 99-2446

[18] Hickman, T., Arrington, L., Frandina, M., and Soulas, G., "Overview of Diagnostics for the NEXT Long Duration Test," 41st *AIAA/ASME/SAE/ASEE Joint Propulsion Conference & Exhibit,* AIAA 2005-4064, Tucson, AZ, 10-13 July 2005

[19] Kamhawi, H., Soulas, G., Patterson, M., and Frandina, M., "NEXT Ion Engine 2000 hour Wear Test Plume and Erosion Results," *40th AIAA/ASME/SAE/ASEE Joint Propulsion Conference and Exhibit*, AIAA 2004-3792, Ft. Lauderdale, FL, 11-14 July 2004

[20] Herman, D., Soulas, G., Patterson., M. "Status of the NEXT Ion Thruster Long-Duration Test after 10,100 h and 207 kg Demonstrated." 43rd AIAA/ASME/SAE/ASEE Joint Propulsion Conference & Exhibit, July 8-11, 2002 Cincinnati, OH, AIAA-2007-5272

[21] Soulas, G., "The Impact of Back-Sputtered Carbon on the Accelerator Grid Wear Rates of the NEXT and NSTAR Ion Thrusters," *33rd International Electric Propulsion Conference*, IEPC-2013-157, Oct. 6-10, 2013, IEPC, Washington, D.C.

[22] Pencil, E., et al., "Ion Beam Characterization of a NEXT Multi-Thruster Array Plume," *42th AIAA/ASME/SAE/ASEE Joint Propulsion Conference & Exhibit,* AIAA 2006-5182, Sacramento, CA, 9-12 July 2006

[23] King, L. and Gallimore, A., "Ion Energy Diagnostics in the Plume of an SPT-100 from Thrust Axis to Backflow Region," *34th AIAA/ASME/SAE/ASEE Joint Propulsion Conference & Exhibit*, AIAA 1998-3641, Cleveland, OH, 13-15 July 1998

[24] Mikellides, I., Jongeward, G., Katz, I., and Manzella, D., "Plume Modeling of Stationary Plasma Thrusters and Interactions with the Express-A Spacecraft," *Journal of Spacecraft and Rockets*, Vol. 39, No. 6, Nov-Dec. 2002, pp.894-903

[25] Wartelski, M., Theroude, C., Ardura., C.,and Gengembre., E., "Self-consistent Simulations of Interactions between Spacecraft and Plumes of Electric Thrusters," *33rd International Electric Propulsion Conference*, IEPC-2013-73, Oct. 6-10, 2013, IEPC, Washington, D.C.

[26] Darnon, F., "The SPT-100 Plasma Plume and its Interaction with a Spacecraft, from Modeling to Ground and Flight Characterization," *36th AIAA/ASME/SAE/ASEE Joint Propulsion Conference & Exhibit*, AIAA-2000-3525, Huntsville, AL, 17-19 July 2000

[27] Mikellides, I., et al., "A Hall-Effect Thruster Plume and Spacecraft Interactions Modeling Package," *27th International Electric Propulsion Conference*, IEPC-01-251, Oct. 15-19, 2001, IEPC, Pasadena, CA

[28] Oh, D., et al., "Modeling of Stationary Plasma Thruster-100 Thruster Plumes and Implications for Satellite Design," *Journal of Propulsion and Power*, Vol. 15, No. 2, Mar-Apr 1999, pp. 345-357

[29] Kannenberg, K. and Khayms, V., "Validation of Hall Thruster Plume Sputter Model," 37th *AIAA/ASME/SAE/ASEE Joint Propulsion Conference*, AIAA 2001-3986, Salt Lake City, UT, 9-11 July 2001

[30] Chesta, E., et al., "CNES Electric Propulsion activities overview: flight programs, R&T actions, novel mission designs," *30th International Electric Propulsion Conference*, IEPC-2007-206, Sep. 17-20, 2007, IEPC, Florence, Italy

[31] Darnon, F., Arrat, D., d'Escrivan, S., Chesta, E., and Pillet, N., "An overview of Electric Propulsion activities in France," *43rd AIAA/ASME/SAE/ASEE Joint Propulsion Conference & Exhibit*, AIAA 2007-5165, Cincinnati, OH, 8-11 July 2007

[32] Gonzalez del Amo, J., et al., "Spacecraft/thrusters interaction analysis for SMART-1," *29th International Electric Propulsion Conference*, IEPC-2005-003, Oct. 31-Nov. 4, 2005, IEPC, Princeton University

[33] Manzella, D., et al., "Hall Thruster Plume Measurements On-Board the Russian Express Satellites," NASA/TM-2001-211217, 2001

[34] Samanta Roy, R., Hastings, D., and Gatsonis, N., "Ion Thruster Plume Modeling for Backflow Contamination," *Journal of Spacecraft and Rockets*, Vol. 33, No. 4, July-Aug 1996, pp. 525-534

[35] Khayms, V. and Kannenberg, K., "Long Term Exposure of a Biased Solar Array to a Hall Thruster Plume," *41st AIAA/ASME/SAE/ASEE Joint Propulsion Conference & Exhibit*, AIAA 2005-3670, Tuscon, AZ, 10-13 July 2005

[36] Pencil, E., Randolph, T., and Manzella, D., "End-of-life Stationary Plasma Thruster far-field plume characterization," *32nd AIAA/ASME/SAE/ASEE Joint Propulsion Conference & Exhibit*, AIAA 1996-2709, Lake Buena Vista, FL, 1-3 July 1996

[37] Tartz, M., et al., "Sputter Yields of Mo, Ti, W, Al, Ag Under Xenon Ion Incidence," *European Physical Journal D*, Vol. 61, 2011, pp.587-592

[38] Rosenberg, D. and Weiner, K., "Sputtering Yields for Low Energy He^+, Kr^+, and Xe^+ Ion Bombardment," *Journal of Applied Physics*, Vol. 33, No. 5, May 1962, pp. 1842-1845

[39] Borde, J., Teston, F., Santandrea, S., and Boulade, S., "Feasibility of the Proba-3 Formation Flying Demonstration Mission as a Pair of Microsats in GTO," *The 4S Symposium: Small Satellites, Systems, and Services 2004*, ESA-SP-571, La Rochelle, France

[40] Landgraf, M. and Mestreau-Garreau, A., "Formation Flying and Mission Design for Proba-3," *Acta Astronautica*, Vol. 82, pp. 137-145

[41] Llorente, J., et al. “PROBA-3: Precise Formation Flying Demonstration Mission,” *Acta Astronautica*, Vol. 82, pp. 38-46

[42] Gill, E., D’Amico, S., and Montenbruck, O., “Autonomous Formation Flying for the PRISMA Mission,” pp. 671-681, *Journal of Spacecraft and Rockets*, Vol. 44, No. 3, May-June 2007

[43] Anflo, K. and Mollerberg, R., “Flight Demonstration of New Thruster and Green Propellant Technology on the PRISMA satellite,” *Acta Astronautica*¸Vol. 65, 2009, pp. 1238-1249

[44] Ardaens, J-S., D’Amico, S., and Montenbruck, O., “Flight Results from the PRISMA GPS-Based Navigation,” *5th ESA Workshop on Satellite Navigation Technologies, NAVITEC’2010*, 8-10 Dec. 2010, Noordwijk, Netherlands

[45] D’Amico, S., Ardaens, J-S, and Montenbruck, O., “Navigation of Formation Flying Spacecraft using GPS: the PRISMA Technology Demonstration,” ION-GNSS-2009

[46] Bodin, P., et al., “PRISMA: An In-Orbit Test Bed for Guidance, Navigation, and Control Experiments,” pp. 615-623, *Journal of Spacecraft and Rockets*, Vol. 46, No. 3, May-June 2009

[47] Persson, S., Veldman, S., and Bodin, P., “PRISMA-A formation flying project implementation phase,” *Acta Astronautica*, Vol. 65, 2009, pp. 1360-1374

[48] Kreiger, G., et al., “TanDEM-X: A Satellite Formation for High-Resolution SAR Interferometry,” pp. 3317-3341, *IEEE Transactions on Geoscience and Remote Sensing*, Vol. 45, No. 11, November 2007

[49] Moreira, A., et al., “TanDEM-X: A TerraSAR-X Add-On Satellite for Single-Pass SAR Interferometry,” pp. 1000-1003, IEEE 0-7803-8742-2/04

[50] Zink, Manfred, et al. "The TanDEM-X mission concept," *Synthetic Aperture Radar (EUSAR), 2008 7th European Conference on*. VDE, 2008

[51] Hoang, B., et al., “Test Program of Multi-Junction GaAs/Ge Solar Array Coupons with Combined Space Environmental Exposures,” pp. 003263-003268, *Photovoltaic Specialists Conference, 2012 38th IEEE*, Austin, TX, 3-8 June 2012

[52] Yalin, A., et al., “Effect of Ion Sputtering on Transmission of Coverglass with Magnesium Fluoride Coating,” *32nd International Electric Propulsion Conference*, IEPC-2011-066, Sep. 11-13, 2011, IEPC, Wiesbaden, Germany

[53] Hu, S., et al., “Hall Thruster Plume Effects and Sputtering of Spacecraft Surfaces,” *37th Joint Propulsion Conference*, AIAA 2001-3356, Salt Lake City, UT, July 9-11, 2001

[54] Vayner, B. and Galofaro, J., “Solar Array in Dense Plasma,” *52nd Aerospace Sciences Meeting, AIAA SciTech 2014*, AIAA 2014-1421, National Harbor, MD, 13-17 January 2014

[55] Eckstein, W., Preuss, R., “New Fit Formulae for the Sputtering Yield”, *Journal of Nuclear Materials*, Vol. 320, pp. 209-213

[56] Bohdansky, J., "A Universal Relation for the Sputtering Yield of Monatomic Solids at Normal Ion Incidence," *Nuclear Instruments and Methods in Physics Research*, Vol. B, No. 2, pp. 587-591

[57] Eckstein, W., García-Rosales, C., Roth, J., and László, J., "Threshold Energy for Sputtering and its Dependence on Angle of Incidence," *Nuclear Instruments and Methods in Physics Research*, Vol. B, No. 83, pp. 95-109

[58] Yamamura, Y., Itikawa, Y., and Itoh, N., "Angular Dependence of Sputtering Yields of Monatomic Solids," *Institute of Plasma Physics, Japan*, IPPJ-AM, No. 26, 1983

[59] Murty, R.C., "Effective Atomic Numbers of Heterogeneous Materials," pp. 398-399, *Nature*, Vol. 207, July 24, 1965

[60] Young, J., Sedwick, R., Dumpala, S., and Rajan, K., "High Energy Plume Impingement on Spacecraft Systems," *52nd Aerospace Sciences Meeting, AIAA SciTech 2014*, AIAA-2014-1032, National Harbor, MD, 13-17 January 2014

[61] Kimball Physics FC-71A Datasheet

[62] Veeco Instruction Manual, FabLab

[63] Veeco NT1100 Setup Guide

[64] Staugaitis, C. and Kobren, L., "Mechanical and Physical Properties of the Echo II Metal-Polymer Laminate," NASA TN-D-3409, 1966

[65] https://en.wikipedia.org/wiki/Clausius%E2%80%93Clapeyron_relation from 9/3/2017 @ 6:02 PM

[66] Ekholm, J., et al., "Plume Characteristics of the Busek 600 W Hall Thruster," *42nd AIAA/ASME/SAE/ASEE Joint Propulsion Conference & Exhibit*, AIAA-2006-4659, Sacramento, CA, 9-12 July 2006

[67] McVey, J. et al., "Characteristics of the T-220HT Hall-Effect Thruster," *39th AIAA/ASME/SAE/ASEE Joint Propulsion Conference & Exhibit*, AIAA-2003-5158, Huntsville, AL, 20-23 July 2003

[68] https://en.wikipedia.org/wiki/A-train_(satellite_constellation)

[69] https://en.m.wikipedia.org/wiki/Orbital_station-keeping

[70] Güttler, D., *An Investigation of Target Poisoning during Reactive Magnetron Sputtering* (Doctoral Dissertation), Retrieved from Qucosa, www.qucosa.de/fileadmin/data/qucosa/documents/137/1240493527858-2666.pdf

[71] Wanlass, F. and Eyring, H., "Sticking Coefficients," *Solid Surfaces*, Ch. 16, pp. 140-145, June 1961

[72] Korkut, B., Levin, D., Young, J., and Sedwick, R., "Comparison of Ion Thruster Plumes Generated in the SPPL-1 Facility with DSMC Simulations using AMR," *52nd Aerospace Sciences Meeting, AIAA SciTech 2014*, AIAA-2014-0139, National Harbor, MD, 13-17 January 2014